INFORMATION TO USERS

This manuscript has been reproduced from the microfilm master. UMI films the text directly from the original or copy submitted. Thus, some thesis and dissertation copies are in typewriter face, while others may be from any type of computer printer.

The quality of this reproduction is dependent upon the quality of the copy submitted. Broken or indistinct print, colored or poor quality illustrations and photographs, print bleedthrough, substandard margins, and improper alignment can adversely affect reproduction.

In the unlikely event that the author did not send UMI a complete manuscript and there are missing pages, these will be noted. Also, if unauthorized copyright material had to be removed, a note will indicate the deletion.

Oversize materials (e.g., maps, drawings, charts) are reproduced by sectioning the original, beginning at the upper left-hand corner and continuing from left to right in equal sections with small overlaps.

Photographs included in the original manuscript have been reproduced xerographically in this copy. Higher quality 6" x 9" black and white photographic prints are available for any photographs or illustrations appearing in this copy for an additional charge. Contact UMI directly to order.

UMI®

ATOMISTIC SIMULATION STUDIES OF DEFECT FORMATION, MIGRATION
AND STABILITY IN ION-IMPLANTED SILICON

By

GOPALAKRISHNAN SUBRAMANIAN

A DISSERTATION PRESENTED TO THE GRADUATE SCHOOL
OF THE UNIVERSITY OF FLORIDA IN PARTIAL FULFILLMENT
OF THE REQUIREMENTS FOR THE DEGREE OF
DOCTOR OF PHILOSOPHY

UNIVERSITY OF FLORIDA

2000

UMI Number: 9997873

UMI®

To my parents

ACKNOWLEDGMENTS

The author would like to thank his advisor Prof. Kevin Jones for his guidance, support and encouragement. The author would like to thank Prof. Mark Law for helpful discussions and the other members of the author's supervisory committee, Profs. R. T. Dehoff, S. J. Pearton and R. K. Singh, for their advice.

The author would like to express his deep sense of gratitude to Dr. Maria Caturla and Dr. T. Diaz de la Rubia, both belonging to Lawrence Livermore National Laboratory, for helping the author get started with his simulations. They provided the code for the simulations and Dr. Caturla was very helpful by continuously giving useful suggestions. The author is particularly grateful to Dr. Caturla for coming to Gainesville and collaborating with him in running the molecular dynamics code for diffusivity calculations.

Special thanks go to Mr. James Albury for his assistance in preparing this thesis. Finally, the author would like to thank his parents for their support.

iii

TABLE OF CONTENTS

LIST OF TABLES

LIST OF FIGURES

vii

viii

Abstract of Dissertation Presented to the Graduate School
of the University of Florida in Partial Fulfillment of the
Requirements for the Degree of Doctor of Philosophy

ATOMISTIC SIMULATION STUDIES OF DEFECT FORMATION, MIGRATION
AND STABILITY IN ION-IMPLANTED SILICON
By

Gopalakrishnan Subramanian

December 2000

Chairman: Prof. Kevin Jones
Major Department: Materials Science and Engineering

Point defects, submicroscopic clusters and extended defects play an important

role in dopant diffusion in ion-implanted silicon. Point defects aggregate during the

annealing process to form small clusters, {311} defects and dislocation loops. {311}

defects, in turn, have been observed to release interstitials upon annealing the silicon.

These interstitials interact with dopant atoms such as boron leading to transient enhanced

diffusion.

In this work, molecular dynamics simulations are used to study the motion of

interstitial, vacancy and di-interstitial species in silicon. From these calculations the

validity of the new environment dependent interatomic potential is determined by

comparing the interstitial migration energy barrier obtained from different interatomic

potentials.

Molecular dynamics simulations are also used to determine the formation energies

of self-interstitial clusters with less than 10 interstitials. By comparing these formation

x

energies with those of {311} defects of the same size inferences are drawn about the transition from these sub-microscopic clusters to {311} defects. Further, in this work, the formation energies of {311} defects and perfect dislocation loops are computed using the conjugate gradient technique. From the formation energy values of {311} defects with varying widths, the possibility of a length to width correlation of these defects is studied which has a bearing on the traditional view of the growth of these defects.

Finally, the relative stability of {311} defects and perfect dislocation loops is determined from the nucleation free energies of these defects. From this study a better understanding of the unfaulting behavior of {311} defects to form dislocation loops is gained.

CHAPTER 1
INTRODUCTION

1.1 Motivation

In the semiconductor industry, ion implantation is used most commonly for producing reproducible, precisely controlled doping in the fabrication of integrated circuits. Ion implantation is also used to modify the properties of solids. This work will deal with the application of ion implantation in semiconductors, primarily, for doping of silicon. The major disadvantage of ion implantation is that the implant produces damage in silicon. This necessitates a post-implant annealing step to activate the dopants. As a result of this anneal, silicon self-interstitials formed by the implant attain sufficient energy to aggregate into extended defects. These defects, by acting as a source of interstitials, lead to anomalous diffusion of dopants due to the interaction between self-interstitials and dopants upon elevated temperature annealing. This phenomenon, known as transient- enhanced diffusion (TED), results in changes in the junction depth leading to degradation in the performance of future generation semiconductor devices.

TED also is found to occur under conditions where there is a suppression of the formation of extended defects suggesting that submicroscopic interstitial defects exist [Zhang 95]. While structural characterization of {311} defects is possible using Transmission electron microscopy (TEM), the characteristics of small clusters are not well understood. It was only recently that evidence of the presence of small clusters was found for self-implants using deep level transition spectroscopy [Benton 97]. Moreover,

1

for many years now, considerable experimental and theoretical investigations have been carried out to study the structure, energetics and migration of point defects in silicon in addition to their role in TED. Experimental work in silicon has produced conflicting evidence resulting in debates, particularly, on the relative contribution of vacancies and interstitials on silicon self-diffusion.

In contrast to this, theoretical work has made significant progress in this area using both first principle calculations and atomistic simulations based on empirical interatomic potentials. However, controversy remains regarding some of the most fundamental properties of point defects. A number of crucial parameters such as the diffusivities and formation energies of point defects have not been well established.

Moreover, small interstitial clusters have not been sufficiently characterized and the transition from small clusters to extended defects needs further investigation. On the issue of extended defects such as {311} defects and dislocation loops, parameters such as formation energies and relative stability of these extended defects have not been conclusively obtained. Some work has been done related to Si self-diffusion [Gilmer 95] using the Stillinger-Weber interatomic potential. As far as small silicon self-interstitial clusters are concerned, tight binding molecular dynamics calculations have been done to obtain information about mainly the structure of clusters with a maximum of nine interstitials [Colombo 99]. More recently, the transition from small interstitial clusters to extended {311} defects has been investigated experimentally using photoluminescence and TEM studies [Coffa 2000]. The conclusion of this study was that small interstitial clusters are not direct precursors of the {311} defects and that a structural transformation must occur at some stage of the growth process.

Nucleation of vacancy type dislocation loops and voids has been studied [Tan 97]. However there is no known work in the literature regarding the interstitial-type dislocation loops. Moreover, the relative stability of loops versus {311}s has not been studied. The unfaulting of {311} defects has been found to be the source of dislocation loops by TEM studies [Li 98]. Understanding why {311}s form rods is essential to developing accurate {311} nucleation, growth, dissolution models and loop nucleation models.

1.2 Point Defect Diffusion in Silicon

With shrinking device dimensions, it becomes important to understand the tendency of dopants to exhibit enhanced diffusion. Vacancies and interstitials produced due to implant damage have a deleterious effect on the junction depth produced during post-implant annealing. As an example, release of the interstitials by {311} defects tends to produce anomalous enhanced diffusion by the interaction of these interstitials and dopant atoms such as boron or phosphorus. Excess interstitials are generated by a "knock on" effect. Implanted ions displace atoms from their lattice sites close to the surface and create a shallow vacancy-rich region. The displaced atoms and the implanted ions come to rest deeper inside the silicon creating an interstitial-rich region there.

At present, it is believed that most of the Frenkel pairs recombine and leave an interstitial concentration approximately equal to the dose. The aggregation of these excess interstitials leads to the formation of {311} defects and loops which in turn act as a source of interstitial emission and thereby, enhanced diffusion.

Large leakage currents are seen near p-n junction depletion regions due to the presence of defects in that area. Moreover, there is a competition between self-interstitials

and inactive dopants for substitutional lattice sites. This affects the electrical activation of implanted dopants.

It has been observed that there are many mechanisms for the diffusion of point defects through a crystal lattice. The most common mechanisms are described below.

- Vacancy mechanism: This occurs when a dopant atom moves to occupy a lattice site and thus becomes a substitutional atom. In order to achieve long-range movement, the vacancy, which was originally in the dopant site must diffuse to a location some distance away from the original lattice site. A vacancy must diffuse at least three lattice sites away in order to complete the diffusion step. This happens to be the minimum distance that allows the vacancy to come back to a site adjacent to the dopant atom through another path [Fahey 89].

- Interstitialcy diffusion: This occurs when a silicon interstitialcy pair approaches a substitutional dopant atom's lattice site. Diffusion occurs when one of the interstitialcy –silicon atom forms a bond with a third silicon atom to produce a new interstitialcy pair. A similar mechanism occurs with a silicon-dopant interstitialcy defect. It should be noted that, unlike the vacancy mechanism here the diffusing defect remains intact [Fahey 89].

- Interstitial mechanism: This mechanism is operative when an interstitial silicon atom goes near a substitutional dopant atom, dislodges it from its site and occupies the lattice site. Therefore this mechanism is called a "kickout mechanism". The impurity atom is now liberated and can freely migrate in the lattice interstices, until it takes part in another interstitial exchange [Fair 81, Fahey 85,Tan 85]. Fig. 1.1 illustrates these three types of dopant diffusion mechanisms.

1.3 Transient Enhanced Diffusion

For many years to come, ion implantation will continue to be the mainstay of introducing dopants into silicon during the fabrication of devices. During implantation, damage is produced in the form of vacancies and interstitials. In order to remove the damage the implanted silicon wafer is subjected to a high temperature anneal. However, during this annealing phase, many types of extended defects are formed. During this anneal anomalous diffusion of dopants is found to occur which is different from equilibrium diffusion as postulated by Fick's law.

Specifically, the diffusion of boron is enhanced several orders of magnitude greater than the diffusion of boron in thermal equilibrium [Michel 87]. The TED of boron takes place primarily because of silicon excess self-interstitials which are created during boron implantation. From theoretical calculations, such as first principle calculations, the activation energy of boron diffusion associated with Si interstitials is the lowest among possible diffusion mechanisms [Car 84, Nichols 89]. This enhanced diffusion is transient in that it occurs for a certain limited time period, which depends on the annealing temperature. Hence, this anomalous diffusion, which is many orders of magnitude larger than equilibrium diffusion, is called transient enhanced diffusion (TED).

TED is found to be the result of a complicated interaction between dopant atoms, point defects and extended defects. Investigations [Eaglesham 94] have shown that extended defects such as the {311} defects can act as sources of interstitials for driving TED. It has been suggested that Si interstitials, which are released from extended defects, aid dopant impurity movement via the "kickout mechanism" discussed earlier. Other investigations [Zhang 95] have suggested that TED can occur even in the absence of {311} formation due to Boron interstitial clusters, which act as a source of interstitials.

1.4 Classification of Extended Defects in Silicon

During the post-implant annealing of the silicon different types of extended

defects form. The type of extended defect formed depends on the implant and anneal

conditions. A systematic analysis of these defects has been done leading to a

classification scheme [Jones 87]. A schematic of the connection between the damage

density distribution and the effective threshold damage density is illustrated in fig.1.2.

1.4.1 Type I: Sub-Amorphization Defects

This damage is observed when the dose exceeds a critical value and there is no

concomitant amorphization. These defects form around the projected range of the

implanted ions. These defects have two types of morphology: rod-like $\{311\}$ defects and

dislocation loops. $\{311\}$s form at lower doses than dislocation loops. The threshold dose

has been shown to be as low as $7x10^{12}/cm^2$ whereas the threshold for dislocation

formation is around $2x10^{14}/cm^2$. These subamorphization defects form due to the fact

that the concentration of ions implanted exceeds the equilibrium vacancy concentration.

Upon Frenkel pair recombination the implantation process results in a supersaturation of

interstitials. When the implant dose exceeds $2x10^{14}/cm^2$ but below the amorphization

threshold then both $\{311\}$ defects and dislocation loops form. If the anneal is above 800

^0C after implanting with a dose below $2x10^{14}/cm^2$ then no extended defects are seen after

annealing. For higher doses without amorphization then subthreshold dislocation loops

are observed which can be stable to temperatures above 1000 ^0C.

1.4.2 Type II: End-of-Range Defects

These defects arise when an amorphous layer is produced. The location of these

defects is below the amorphous-crystalline interface in heavily damaged but crystalline

material. These defects consist of both dislocation loops and $\{311\}$ defects at low

annealing temperature. However, unlike the subthreshold defects, where there is a possibility of formation of {311} defects without loops, the concentration of interstitials beyond the amorphous/crystalline interface is such that both defects are observed together. There are two major sources of the interstitials for these defects.

The first source consists of transmitted ions which rest below the amorphous/crystalline interface. The second source is the recoiling of the excess interstitials deeper into the material because of the forward momentum of the ion beam. The shallower region where many of the excess vacancies reside in non-amorphizing implants is now amorphized. Therefore, after solid phase regrowth there are excess interstitials from the separated Frenkel pairs which could not recombine because of vacancy incorporation during regrowth. These excess interstitials can now constitute the end of the end-of range loop density as well as providing the general interstitial supersaturation in the end-of range region. The concentration of type II defects is not as strongly dependent on the dose as in the case of type I defects. This is because an amorphous layer exists which increases in thickness as dose increases.

High annealing temperatures are necessary to dissolve end-of range defects, particularly, the loops completely. These temperatures are not attained in the thermal budgets of current processing techniques. If these loops exist in the space charge regions of junctions they can cause high leakage currents. Therefore, the junction should be located deep enough such that the end-of range defects are not in the space charge region of the device.

1.4.3 Type III Defects

Formation of this category of defects can occur due to regrowth of the amorphous layer. These defects are found to exist in the region previously occupied by the

amorphous layer. There are many forms of this defect type. Hairpin dislocations form when the regrowing amorphous/crystalline interface encounters pockets of misoriented crystalline material. The other form of type III defects are microtwins. Defect formation also occurs just beneath the surface. This is due to the rejection of some species, such as flourine, by the progressing amorphous/crystalline interface for sufficient dose.

1.4.4 Type IV Defects

These defects form due to the fact that regrowth of a buried amorphous layer occurs by the movement of both amorphous/crystalline interfaces. At the depth where these two interfaces meet type IV defects originate. These defects are also called "zipper" or "clamshell" defects.

1.4.5 Type V Defects

In ion implantation, which is a non-equilibrium process, the solid solubility of a species can be exceeded in a target material. During solid phase epitaxy, dopant concentrations in excess of the solid solubility can be incorporated in the lattice sites as substitutional species. Upon further annealing, precipitation occurs. The defects thus formed at a dopant projected range depth consist of both dislocation loops and precipitates.

1.5 Extended {311} Defects

The {311} extended defect is peculiar to silicon and germanium. Mathews and Ashby [Mathews 73] observed these defects in irradiated n-type and p-type silicon at temperatures above 400 ^{0}C. They found these defects to be similar in electron-irradiated and proton-irradiated silicon. {311} defects were for the first time found in electron-irradiated germanium by Ferreira et al. [Ferreira 76] , and in annealed, ion-implanted

silicon by Davidson et al. and Chadderton et al. [Davidson 70, Chadderton 71]. It is a {311} stacking fault since fringe contrast is similar to that observed in the common {111} stacking fault. However, the defect has {311} habit planes. Initially, the only structural model proposed was that there is a layer of interstitial atoms in these defects each with three dangling bonds with bonds of the matrix crystal atoms on either side of the interstitial atom layer stretched by 35-48% [Salisbury 79]. This structure is not favorable energetically.

Tan [Tan 81] proposed a low-energy model for {311} defects which consists of a layer of interstitial atoms with no dangling bonds and with insignificant bond length changes. This model is shown in fig. 1.3 (a) and fig. 1.3 (b). In fig. 1.3 (a) the interstitial atoms are on the $(1\bar{1}0)$ plane layers of the matrix crystal. The bond length changes are within 5% for all atoms. Figure 1.3 (b) shows that excepting for the single bond which is shared by two neighboring seven-membered rings and is stretched by 15%, all the remaining bonds are more or less unchanged in their lengths. In both these depictions the defect habit plane is $(\bar{1}\bar{1}3)$.

{311} defects are a part of subthreshold or type I defects. As mentioned in a previous section, the dissolution of these {311} defects is one of the principal sources of interstitials causing TED. Below the loop formation threshold the interstitials generated due to the implantation are in a supersaturated state upon Frenkel pair recombination and these interstitials agglomerate to form the {311} defects. The {311} defects are unstable compared to the loops and they dissolve upon annealing the silicon between 700 and 800^0 C. Figure 1.4 shows the loss of interstitials from {311} defects as a function of annealing time at 750^0 C [Jones 96].

As mentioned in the previous section, type II defects or end of range defects form when the silicon has been amorphized during implantation. Both {311} defects and dislocation loops are seen to form just below the amorphous/crystalline interface at low annealing temperatures. Unlike in subthreshold defects, where {311} defects can form without loops, in the end of range defects both loops and {311}s are seen to form. The {311} defects which are present in the end of range regime coarsen and dissolve upon annealing the sample between 700 and 800^0 C. During the dissolution of the {311}s TED is seen to occur for dopants located both below the amorphous crystalline interface and in the regrown region.

The atomic structure and energy of {311} defects have been studied by energy minimization calculations [Kohyama 92] although the effect of the width of the defect on the energetics of the defect has not been completely investigated. Using the Tersoff interatomic potential the energetics of {311} defects has been investigated, for infinitely long chains, as a function of defect size and width [Cuendet 96]. Continuum calculations have been performed in the modeling of {311} defects [Hobler 99]. Also, total energy calculations using the tight-binding scheme have been carried out to study the structural properties and energetics of {311} defects [Kim 97].

1.6 Scope of This Study

The scope of this work is as follows:

- To carry out a comparative study of diffusivities of point defects using Molecular Dynamics simulations with three different interatomic potentials, namely, the Stillinger Weber (SW) potential, the Tersoff potential and the recently developed

Environment Dependent Interatomic potential (EDIP). From this study the validity of the EDIP potential is determined.

- To calculate formation energies of small interstitial clusters, using Molecular Dynamics simulations with the SW potential, and to analyze the transformation of these clusters into {311} defects.

- To calculate the formation energies of {311} defects, using the conjugate gradient technique, as a function of size and width and to calculate the formation energy of perfect dislocation loops, also using the conjugate gradient method. Thereby, inferences are drawn about the relative stability of these two types of extended defects.
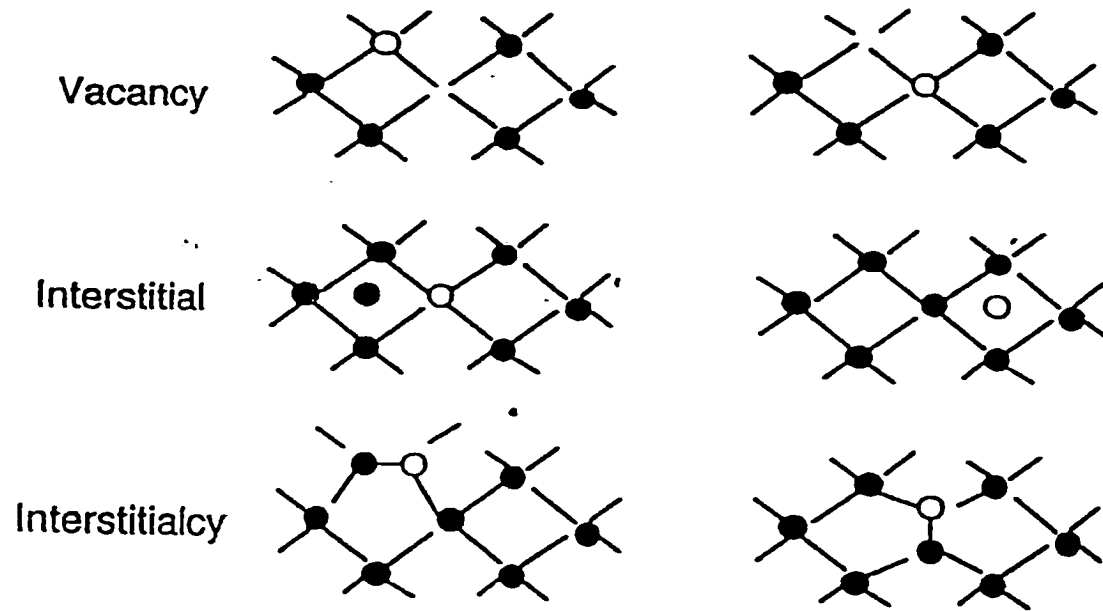
Fig 1.1 Dopant diffusion mechanisms
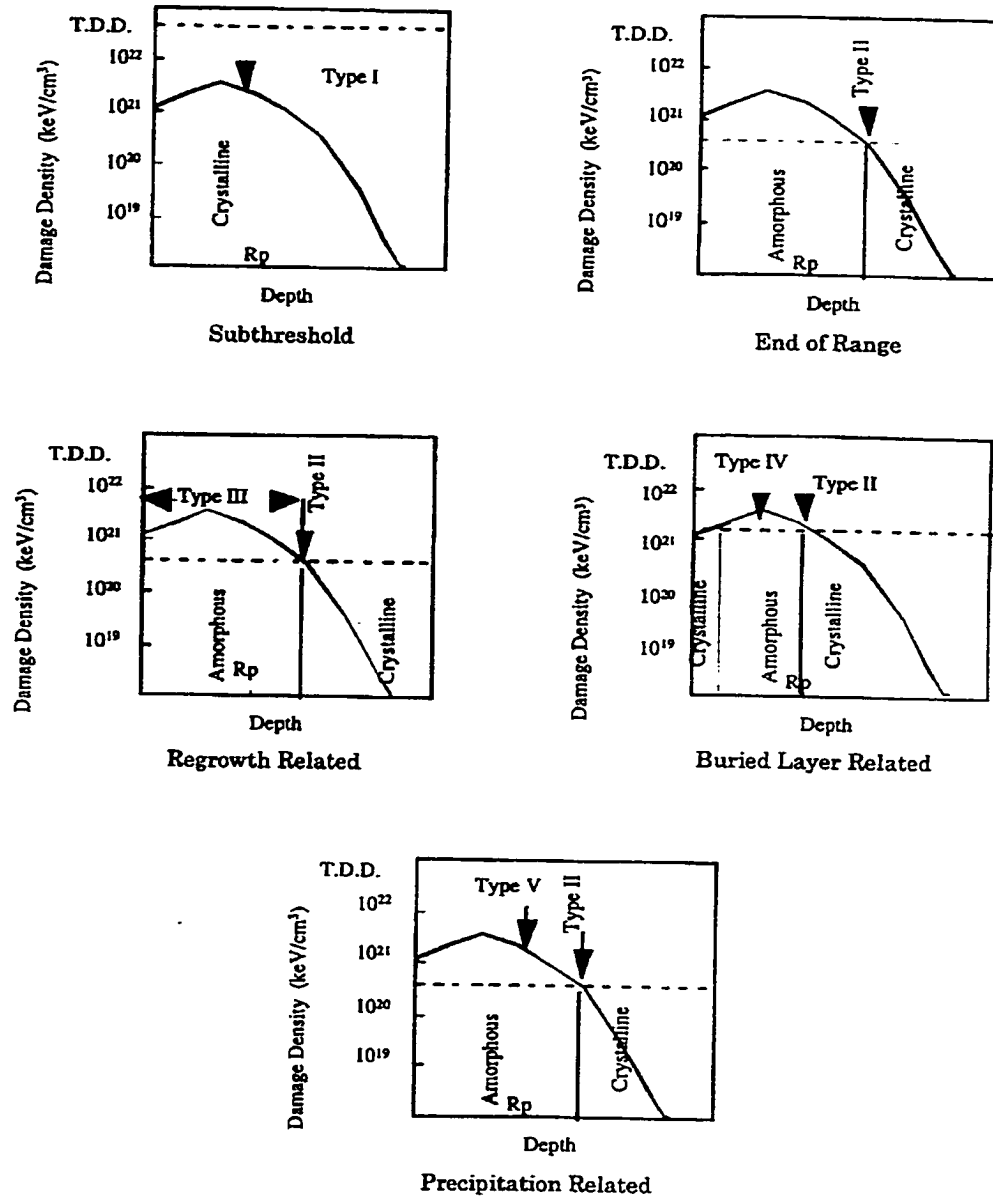
Fig. 1.2 Schematic of damage classification after ion implantation and subsequent annealing
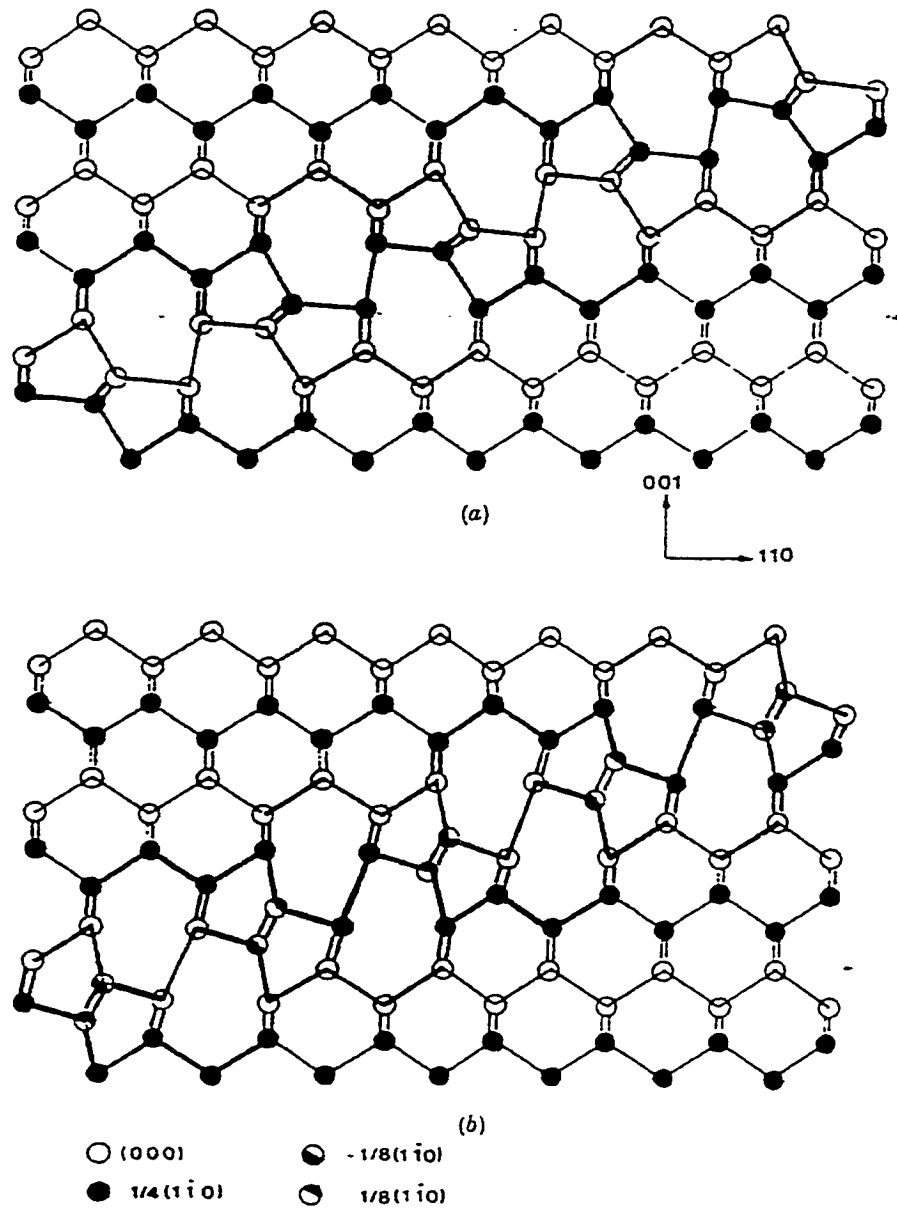
Fig. 1.3 (a) Atomic model of a {311} defect with a matrix crystal displacement of 1/5 [$\bar{1}\,\bar{1}\,1$] (b) Atomic model of a {311} defect with a matrix crystal displacement of 1/25 [$\bar{1}\,\bar{1}\,6$]
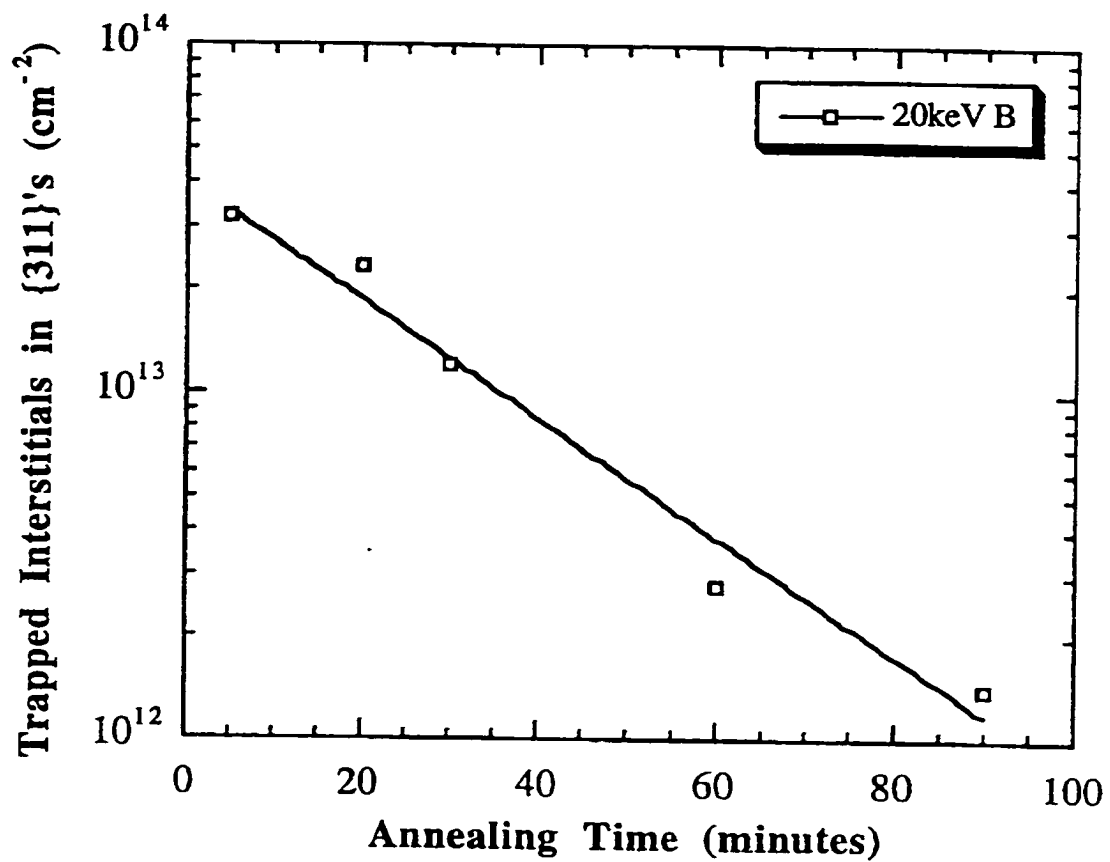
Fig. 1.4 Interstitial loss from {311} defects as a function of annealing time at 750^0 C obtained using quantitative PTEM. Implant conditions are 20 KeV B^+, 2×10^{14} /cm^2

CHAPTER 2
THEORY OF COLLISIONS

2.1 Ion Implantation Models

Ion implantation models can be either analytical theories (AT) or computer

simulations (CS). According to both the models the implanted ion loses energy by elastic

and inelastic collisions [Townsend 76]. When ions collide with the atomic nuclei the

collision is elastic and collisions between ions and electrons are inelastic [Bohr 48]. The

losses due to inelastic collisions are simple energy losses [Lindhard 61]. The collision

will not, in this case, lead to a deviation of the trajectory. On the other hand, elastic

collisions modify the ion's trajectory and the scattering angle in the collision is

determined by an interatomic potential. The binary collision approximation, which is the

simplest model of collisions, assumes that the collision takes place only between two

atoms in the solid. The distance between colliding atoms alone is used in implementing

the interatomic potential. Both analytical theories and computer simulations employ such

interatomic potentials. As a result, these models describe the damage profiles and range

of implanted ions in solids as well as the sputtering of atoms from the surface of the solid.

Since these potentials do not account for the way atoms are bound in the solid,

more advanced potentials are used to determine the interatomic interactions in a solid.

Common examples of these potentials are the EAM [Daw 84] potential for metals and the

Tersoff [Tersoff 89] and Stillinger and Weber (SW) [Stillinger 85] potentials for covalent

materials like silicon. The SW potential consists of two and three body terms and was

16

fitted to experimental properties of the diamond cubic and molten phases of silicon. Among its uses are the study of lattice dynamics [Li 88], point defects [Batra 87], surfaces [Poon 90], and the liquid and amorphous phases [Stillinger 85, Broughton 87], [Luedtke 88, Kluge 87, Ishimaru 96]. The Tersoff potential contains many-body interactions included in a bond order term fitted to various silicon polytypes. Its uses include the study of lattice dynamics [Li 88], point defects [Tersoff 88], thermomechanical properties [Porter 97] and the liquid and amorphous phases [Tersoff 88, Ishimaru 96, Kelires 88].

Recently, more than 30 empirical interatomic potentials have been developed for silicon. These potentials differ in the degree of sophistication, functional form , and range of interaction. No single potential can accurately model various special atomic configurations. It has been claimed that the transferability of the SW and Tersoff potentials to a wide class of structures remains in doubt [Justo 98]. It has also been claimed that, the most recent interatomic potential called the environment-dependent interatomic potential, provides a better description of local structures and is, at the same time, computationally efficient.

These interatomic potentials can be used in molecular dynamics to determine the evolution of a group of atoms as a function of time. This is done by solving Newton's equations of motion involving the potentials to calculate energies and forces of each atom in the computational cell. Although multiple collisions between target atoms are included in the calculations, electronic effects are not included. Certain models like tight binding combine the advantages of classical molecular dynamics (using interatomic potentials) and *ab initio* calculations. Classical molecular dynamics is, by far, the best technique for

studying ion implantation in an energy range between eV and several keV. By employing a sound interatomic potential in classical molecular dynamics calculations it would be possible to gain insight into trends and processes involved in ion implantation collisions, something which is impossible using analytical models and binary collision simulations.

2.2 Ion Range and Stopping in Solid Materials

The observation of emission of energetic particles from radioactive materials created interest in how these particles were slowed down in matter. In the early days, since there was no accurate model for the atom, attempts to create a particle energy loss theory were futile. J.J.Thomson was the first to address the issue of scattering of two point charges in his classic book on electricity [Thomson 03]. Although this book contains an excellent description of classical Coulombic scattering between energetic charged particles, it does not calculate actual stopping powers.

In the decade following the discovery of radioactivity, sufficient experimental evidence was collected to make stopping power theory one of the dominant issues for those trying to develop a model for the atom. Both J.J.Thomson and Niels Bohr were actively involved in the analysis of the stopping of charged particles by matter. However, the model of the atom as an entity with a heavy positively-charged core is attributed to Bohr's work [Bohr 13, Bohr 15]. Bohr's initial work is informative because, for the first time, a unified theory of stopping was proposed. One of Bohr's original postulates was that the energy loss of ions passing through matter has two contributors namely, nuclear stopping (energy loss to the material's positive atomic cores) and electronic stopping (energy loss to the material's light electrons).

The Lindhard, Sharff and Schiott theory (LSS) developed in 1963 was the first analytical approximation to the range and stopping of ions [Lindhard 63]. According to the terminology introduced by these authors, a reduced energy ε and a reduced length ρ as follows:

$$\varepsilon = E \frac{aM_2}{Z_1 Z_2 e^2 (M_1 + M_2)} \qquad (2.1)$$

$$\rho = R\Omega M_2 \frac{4\pi a^2 M_1}{(M_1 + M_2)^2} \qquad (2.2)$$

Subscript 1 denotes the projectile and subscript 2 refers to the target atom, M refers to the mass and Z the atomic number. The existence of electrons in an atom is accounted for in the screening distance a. Ω is the target density. The energy loss of an ion, which is interacting with the target, can be equated to the sum of elastic or nuclear collisions and the inelastic or electronic collision. This equation can be represented as

$$\frac{d\varepsilon}{d\rho} = (\frac{d\varepsilon}{d\rho})_n + (\frac{d\varepsilon}{d\rho})_e = [\, s_n(\varepsilon) + s_e(\varepsilon)\,] \qquad (2.3)$$

where the subscript n refers to nuclear and subscript e refers to electronic. s_n and s_e are called elastic and inelastic stopping powers and these can be obtained analytically assuming very simple interatomic potentials and random collisions. Figure 2.1 shows the nuclear and electronic stopping powers as a function of reduced energy obtained using the assumptions of the LSS theory [Robinson 94].

Whereas the elastic energy loss is independent of the mass ratios, the inelastic energy loss is more important for high mass ratios. Upon comparing the contribution of the two types of collisions, it is seen that for low values of ε the elastic collisions

dominate and for ε>1 the inelastic collisions become significant. It should also be noted that even at low energies, for light projectiles inelastic energy losses must be considered. The stopping powers can be used to obtain the range of the ions as follows:

$$\rho(\varepsilon) = \int_{\varepsilon}^{0} \frac{d\varepsilon}{d\varepsilon \, / \, d\rho} = \int_{0}^{\varepsilon} \frac{d\varepsilon}{s_n(\varepsilon) + s_e(\varepsilon)} \qquad (2.4)$$

It must be noted that this equation is valid only when the initial energy of the ion is much greater than the energy transmitted in the collision.

2.2.1 Elastic Collisions

In the LSS model we assume a particular interatomic potential between the ions and atoms in the solid. Only two atoms are involved in a collision according to the stopping theory and this is called the Binary Collision Approximation (BCA). The BCA is justified for high energies when the two colliding electrons are at a separation much smaller than the interatomic distance in the solid and the probability of three or more particles colliding is very small. Moreover, the collision time is much smaller than the vibrational period of the atoms. The interatomic potential will depend only on the distance between the colliding atoms. With reference to figure 2.2, the relationship between the transmitted energy, T and the scattering angle Φ_c

$$T = \frac{4 M_1 M_2 E}{(M_1 + M_2)^2} \sin^2 \frac{\phi_c}{2} \qquad (2.5)$$

where E is the initial energy of the projectile.

2.2.2 Inelastic Collisions

For the case of low velocities and amorphous materials it can be assumed that the inelastic energy loss is proportional to the ion velocity. From the work of Lindhard and Scharff [Lindhard 61], the electronic energy loss can be approximated as

$$\left(\frac{d\varepsilon}{d\rho}\right)_e = k\varepsilon^{1/2} \tag{2.6}$$

$$k \approx \frac{0.0793 Z_1^{1/6} Z_1^{1/2} Z_2^{1/2} (M_1 + M_2)^{3/2}}{(Z_1^{2/3} + Z_2^{2/3})^{3/4} M_1^{3/2} M_2^{1/2}} \tag{2.7}$$

The value of k decreases with ion mass, which means that the inelastic energy losses are more important for lighter ions.

For low velocities, the scattering resulting from a collision is between the ion and the electron gas. At higher ion velocity, the ion has a probability to lose all its electrons and the Lindhard approximation is not valid. In such a case the stopping power will be proportional to v^{-2} in accordance with the Bohr model [Bohr 48]. For the case of even higher velocities, inelastic stopping power calculations are best done using the Bethe and Bloch [Townsend 76] approximation.

2.3 Computer Simulations and Theory

Since the time of Newton, scientific theories have been developed in a reductionistic mode, i.e. a complex system is reduced to one or more simple subsystems which are, in turn, analyzed. At a higher level, simulations serve as an alternative to reductionism since simulations allow us to study the behavior of classes of systems or subsystems. Therefore, while in reductionism the emphasis is on structural analysis, simulations stress on behavioral classification. In fig.2.3, it is shown that simulation has two distinct roles to play in scientific research. At a higher level, simulation can be an alternative to reductionism whereas at a lower level simulation becomes a tool in reductionism.

Analytical theories treat the issue of ion bombardment by using statistical quantities such as cross sections. In these theories, details of individual ion bombardment

are not clear. On the other hand, in computer simulations, single ions are dealt with and their interaction with the target solid is examined. Experimental tools such as scanning tunneling microscopy and atomic force microscopy corroborate some results of simulations such as molecular dynamics simulations. Moreover, computer simulations provide a means of measuring quantities not accessible to experiments.

However, the limitation of computer simulation and theory starts when data is needed for a wide range of ion-target combinations. In this respect range theory provides qualitative values for all ion-target combinations. Computer simulations can be either binary collision approximation (BCA) techniques or classical molecular dynamics. BCA methods are computationally very efficient and can be employed to measure quantities such as sputter yields, ranges or damage profiles. However, the BCA models make use of simple potentials unlike classical molecular dynamics, which employs more accurate potentials fitted to specific properties of the material being studied. This enables one to understand, at a microscopic level, the processes involved in the bombardment of an ion on a particular target. The trade off is that the molecular dynamics simulations are computationally expensive. It follows that sputtering yields and ranges are not easily computed with this technique.

2.3.1 Binary Collision Approximation

The first binary collision approximation (BCA) simulation was reported by Yoshida in 1961 [Yoshida 61]. The BCA models can be classified into the binary crystal (BC) models and the Monte Carlo (MC) models. The BC model employs a crystalline target with all the atoms having well-defined initial positions. MARLOWE, developed by Robinson and Torrens [Robinson 74], is a popular BC model. Modifications and improvements to this model such as UT-MARLOWE have been done more recently.

Damage and dopant profiles, sputtering yields and a wide range of target-projectile combinations have been simulated using UT-MARLOWE [Tasch 95]. Monte Carlo models use random methods to locate target atoms as well as random values to obtain collision parameters. In this category, TRIM, a program developed by Biersack and Haggmark [Biersack 80] and updated yearly by Ziegler is very popular among experimentalists and in the modeling world.

In order to use time scales and temperatures typically used in semiconductor manufacturing, programs for calculating damage production are coupled with a Monte Carlo simulation of defect diffusion. This simulation is carried out by first generating a cascade by MARLOWE. The locations of vacancies and interstitials, obtained from the set of sites where a displaced atom was in its final and initial positions respectively, are passed on to the Monte Carlo diffusion simulator. Vacancy –interstitial recombination, annihilation at the surface, clustering of like defects, re-emission from the clusters and interstitial trapping at native carbon traps are achieved by giving the vacancies and interstitial random jumps. The accuracy of the MC diffusion simulations depends on the accuracy of the parameters used. It should be noted that Binary collision models have succeeded in generating subcascades for high incident particle energies [Beeler 76].

2.3.2 Molecular Dynamics Simulations

Molecular Dynamics (MD) simulations integrate the equations of motion for all the atoms in a computational cell. In classical MD simulations interaction between the particles is determined by empirical interatomic potentials. Particle trajectories are calculated by integrating the Newton's equations of motion. The gradient of a conservative potential yields the force as a function of the particle coordinates. The relevant equations are listed below:

$$\vec{F}_i = -\nabla V(\vec{r}) \tag{2.8}$$

$$\frac{d^2\vec{r}}{dt^2} = \frac{\vec{F}_i}{m_i} \tag{2.9}$$

These equations can be numerically integrated to give the particle trajectories using time as the integration step. There is a trade-off between computation efficiency and errors in choosing the time step. Usually, the time step is of the order of 0.5-1.0 femtoseconds (fs).

2.3.2.1 Newtonian Dynamics

For N spherical molecules, Newton's second law represents 3N second order ordinary differential equations of motion. MD simulations require a numerical method for solving the differential equations of motion. The classical tools for solving initial value problems are finite difference methods. These methods replace differentials such as dx and dt with finite differences Δx and Δt. Therefore they replace differential equations with finite difference equations. Also, over a small but finite time interval Δt, these methods assume that the rate or some known function of the rate is constant

2.3.2.2 Periodic Boundary Conditions

Typically MD simulations are done on systems containing several hundred or a few thousand atoms. In simulations where surface effects are not of interest, they are removed using periodic conditions. Periodic boundary conditions are implemented in a simulation of N atoms confined to a volume V, by assuming that volume V is only a small fraction of the bulk material. This volume V, called the primary cell, is representative of the bulk material with the assumption that the bulk is composed of the primary cell surrounded by exact replicas of itself called image cells. Therefore the primary cell is imagined to be periodically replicated in all directions to constitute a

macroscopic sample of the substance of interest. This periodicity extends to the positions and momenta of the images in image cells.

2.3.2.3 Predictor-Corrector Algorithms

Predictor-Corrector algorithms consist of three steps: prediction, evaluation and correction. Specifically, from the current position x(t) and velocity v(t) the steps are as follows:

1. Predict the position $x(t+\Delta t)$ and velocity $v(t+\Delta t)$ at the end of the next step.

2. Evaluate the forces at $t+\Delta t$ using the predicted position.

3. Correct the predicted positions and their derivatives using the discrepancy between the predicted acceleration and that given by the evaluated force (using the potential energy function).

In this work, the MD simulation code used is called MDCASK. This code is adaptable to work stations. The classical equations of motion are integrated numerically using a fourth order predictor-corrector scheme. The Langevin equation of motion is applied to the atoms in the link cells adjacent to the cell boundaries in order to control crystal temperature.

2.3.2.4 Interatomic Potential

The interatomic potential contains the information about the interaction between the particles. The first potentials to be used were the Born-Mayer potential [Gibson 60] and the Lennard-Jones potential. More sophisticated potentials have since been used. Examples are the embedded atom poential (EAM) by Daw and Baskes [Daw 84] which has proven to be very successful in cascade simulation in metals and alloys [Diaz de la Rubia 92]. Some of the most important potentials for covalent materials are the Stillinger-Weber potential [Stillinger 85], the Tersoff potential [Tersoff 89] and more recently, the

environment-dependent interatomic potential (EDIP) [Bazant 97]. A discussion of these potentials for silicon can be found in later chapters.

Prior to studies of ion-implantation in semiconductors, radiation damage studies in metals were carried out beginning with Vineyard and co-workers at Brookhaven [Vineyard 72]. Related studies in collision cascade phenomena as a result of radiation damage have been done since with the advent of powerful computers.

To summarize, MD appears to be the most powerful tool in the study of ion-implantation of ions with energies between eV and a few keV for the following reasons: MD avoids the approximations which are found in analytical theories. MD simulations incorporate the target structure. MD can be used to study the defect distribution in the cascade. Using empirical potentials, only reasonable computing times are required for simulations with millions of atoms

In this work only classical MD has been used and the code, MDCASK, which is used to carry out the simulations will be discussed in the next chapter.
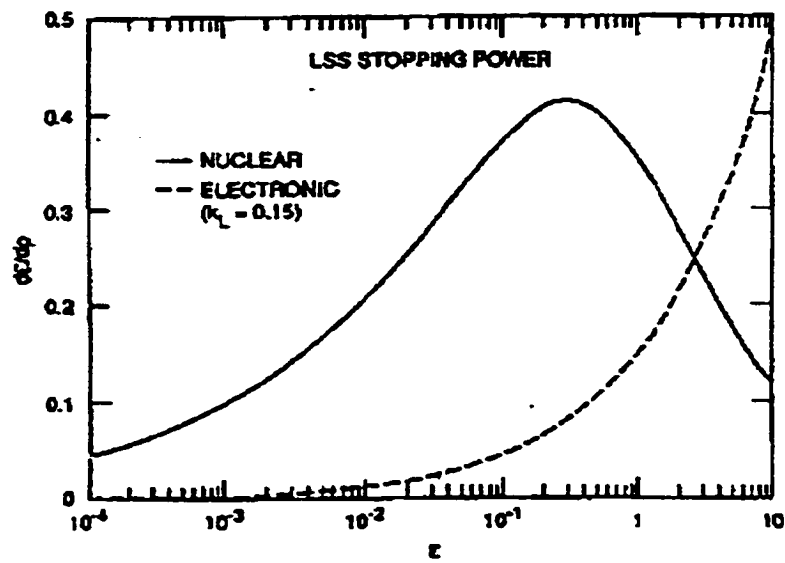
Fig. 2.1 Nuclear and Electronic stopping powers as a function of reduced energy ε
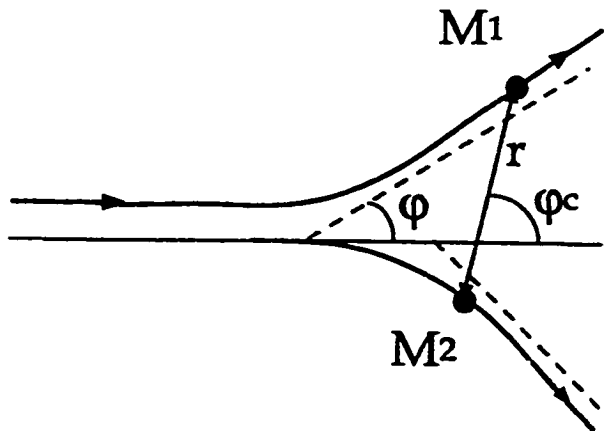
Fig. 2.2 Two atom scattering
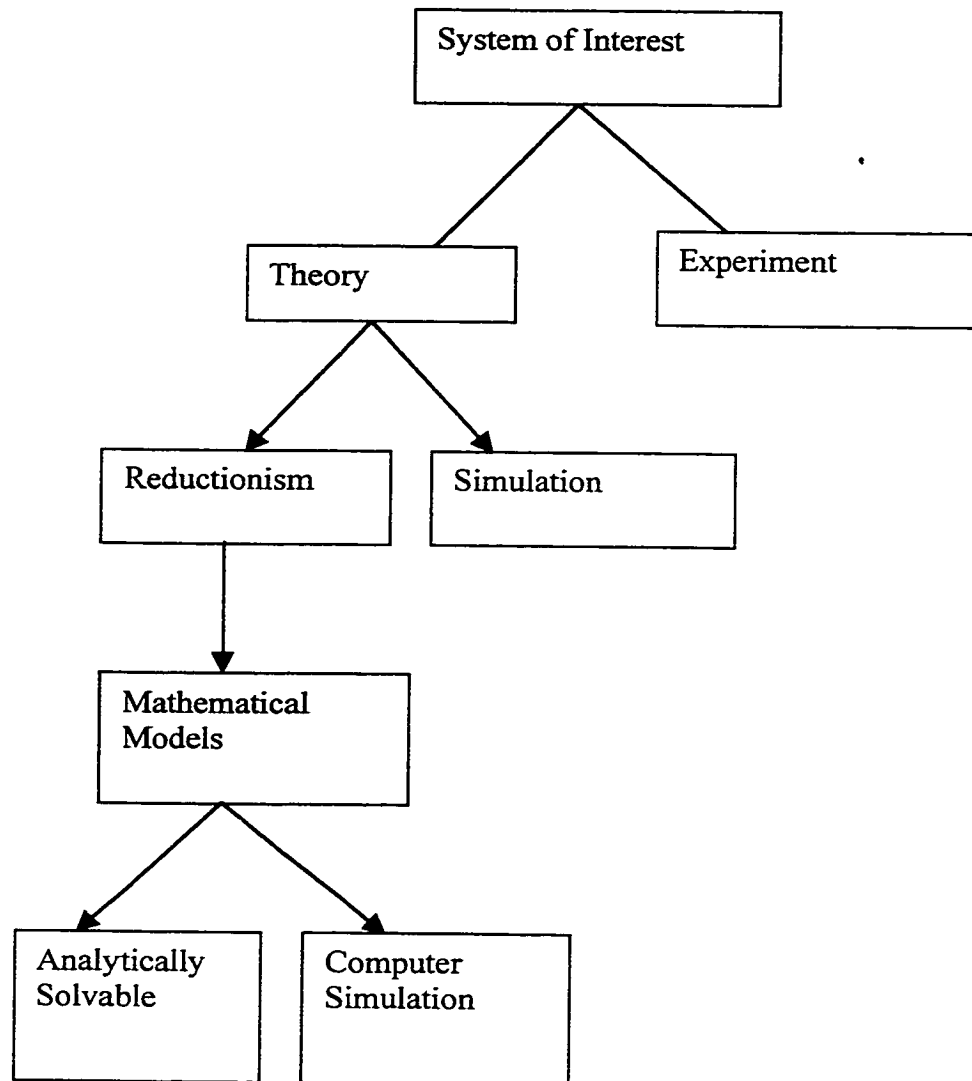
Fig. 2.3 Hierarchy of scientific methods of investigation

CHAPTER 3
COMPUTER CODE FOR MD SIMULATIONS: MDCASK

MDCASK is a code originally based on the MOLDY code developed at Harwell laboratory in the United Kingdom by Finnis and co-workers [Finnis 89]. MDCASK can be used to study ion implantation in the energy range between eV and a few keV in silicon, silicon carbide and metals targets.

MD simulations generally require an algorithm for integrating the equations of motion, specific boundary conditions and an interatomic potential. Integration of equations of motion is carried out in MDCASK using a fourth-order predictor corrector algorithm [Berendsen 85] which is explained in detail in the next section.

There are as many as 30 interatomic potentials today for silicon. In this work the Stillinger Weber potential is primarily used although some work has been done with the Tersoff and the Environment Dependent Interatomic Potential (EDIP) which will be presented in subsequent chapters. MDCASK uses periodic boundary conditions whereby the MD computational cell is repeated to simulate an infinite solid [Born 12]. This is accomplished through the minimum image conversion method [Allen 86]. In a real solid, if implantation is carried out, the initial ion energy will spread out in the solid by conduction resulting in thermal equilibrium with the same initial temperature. On the other hand, in simulations, upon the application of boundary conditions the energy remains inside the solid increasing its temperature. The MDCASK code has features to achieve constant temperature as in a real solid which will be explained in this chapter.

29

3.1 The Predictor Corrector Algorithm

The technique to integrate the equations of motion used in MDCASK is called the fourth-order predictor corrector scheme. Assuming that the classical trajectory of the atoms in the system is continuous, a Taylor expansion can be used to calculate the positions (r), velocity (v), acceleration (a), etc. at a time $t+\delta t$, given the value of these quantities at time t. The expressions for the dynamic variables would be predicted as follows, if the Taylor's series is truncated in the third derivative:

$$r^p(t + \delta t) = r(t) + \delta t v(t) + \frac{1}{2} \delta t^2 a(t) + \frac{1}{6} \delta t^3 b(t) \qquad (3.1)$$

$$v^p(t + \delta t) = v(t) + \delta t a(t) + \frac{1}{2} \delta t^2 b(t) \qquad (3.2)$$

$$a^p(t + \delta t) = a(t) + \delta t b(t) \qquad (3.3)$$

$$b^p(t + \delta t) = b(t) \qquad (3.4)$$

The predicted values for the positions lead to the forces at time $t+\delta t$ using the inter-atomic potential. The correct accelerations, $a^c(t+\delta t)$, give us the error in the prediction step as:

$$\Delta a(t + \delta t) = a^c(t + \delta t) - a^p(t + \delta t) \qquad (3.5)$$

This error is incorporated in the predicted values, thus yielding the corrected new positions and velocities as

$$r^c(t + \delta t) = r^p(t + \delta t) + c_0 \Delta a(t + \delta t) \qquad (3.6)$$

$$v^c(t + \delta t) = v^p(t + \delta t) + c_1 \Delta a(t + \delta t) \qquad (3.7)$$

$$a^c(t + \delta t) = a^p(t + \delta t) + c_2 \Delta a(t + \delta t) \qquad (3.8)$$

$$b^c(t + \delta t) = b^p(t + \delta t) + c_3 \Delta a(t + \delta t) \qquad (3.9)$$

The values of the coefficients c_0, c_1, c_2 and c_3 have been optimized by Gear and are the following for a fourth order predictor corrector algorithm:

$c_0 = 1/6$, $c_1 = 5/6$, $c_2 = 1$ and $c_3 = 1/3$

The finite time-step of the simulation introduces errors in the solutions of the classical equations of motion. Therefore, the optimum time step is chosen such that $\Delta t \ll 1/\upsilon$ where υ is the vibrational frequency of the atoms in the solid. In MD this time step is a femtosecond.

3.2 Cell Structures and Linked Lists

In the beginning of the simulation, a list is constructed of all the neighbors of each molecule. In order to facilitate this, the cubic simulation box is divided into smaller cells, the dimensions of each being slightly larger than the cut off distance of the interatomic potential. For example, as shown in fig. 3.1, the neighbors of the molecules in the two dimensional cell 13 are found in cells 7, 8, 9, 12, 13, 14, 17, 18, 19. The linked lists method can be adopted while using the cell structure described above. The first step involves sorting all the molecules into their appropriate cells. The identification of one of the molecules in each of the cells is stored in an array while executing the program. This head-of-chain molecule number is used to identify the element of a linked list array which contains the number of the next molecule in that cell. This linked list array element for this molecule, in turn, indicates the next molecule in the cell and this process is continued until an element of the linked list array becomes zero. At this juncture, it becomes clear that there are no more molecules in that cell and the code moves on to the

head-of-chain molecule of the next cell. The MD program calculates the forces by looping over all cells.

3.3 The Stillinger-Weber Interatomic Potential

Here, the Stillinger-Weber interatomic potential is discussed. The two other interatomic potentials used in this work namely, the Tersoff potential and the environment-dependent interatomic potential (EDIP) will be described in another section. Any interatomic potential must have terms denoting interactions between one body, two body and three body terms such as

$$\Phi = \sum_i \upsilon_1(i) + \sum_{i,j(i<j)} \upsilon_2(i,j) + \sum_{i,j,k(i<j<k)} \upsilon_3(i,j,k) \tag{3.10}$$

Ever since the Stillinger-Weber (SW) potential was developed by Stillinger and Weber in 1985 [Stillinger 85], it has been used extensively in numerous computer simulations. This potential describes very well the solid and liquid states in silicon. Since the Si crystal consists of strong and directional bonds, it would be appropriate to develop a potential energy function comprising pair (υ_2)and triplet (υ_3) terms and this is precisely the form adopted by Stillinger and Weber. Upon introducing an energy unit $\varepsilon$and a length unit σ, the pair and triplet terms can be written as

$$\upsilon_2(r_{ij}) = \varepsilon f_2(r_{ij} / \sigma) \tag{3.11}$$

$$\upsilon_3(r_i, r_j, r_k) = \varepsilon f_3(r_i / \sigma, r_j / \sigma, r_k / \sigma) \tag{3.12}$$

Here ε is chosen to give f_2 depth -1, and σ is chosen to make $f_2(2^{1/6})$ vanish. The reduced

pair potential used by the authors of the SW potential was selected from the following

five-parameter family:

$$f_2(\rho) = \begin{cases} A(B\rho^{-p}-\rho^{-q})\exp[(\rho-a)^{-1}] & r < a \\ 0 & r \geq a \end{cases}$$

(3.13)

where $\rho = r/\sigma$. This form enables us to cut off the function at $\rho = a$, with the derivative

being continuous. The three body term selected by the authors with the same cutoff

advantage is as folows:

$$f_3(\rho_i,\rho_j,\rho_k) = h(\rho_{ij},\rho_{ik},\Theta_{jik}) + h(\rho_{ji}, \rho_{jk}, \Theta_{ijk}) + h(\rho_{ki}, \rho_{kj}, \Theta_{ikj})$$

(3.14)

In this equation, Θ_{jik} is the angle between ρ_j and ρ_k subtended at vertex i. The h functions

take the form

$$h(\rho_{ij},\rho_{ik},\Theta_{jik}) = \lambda\exp[\gamma(\rho_{ij}-a)^{-1} + [\gamma(\rho_{ik}-a)^{-1}]\,(\cos\Theta_{jik}+1/3)^2$$

(3.15)

The most satisfactory parameter set to be fitted to this potential is as follows:

A = 7.049556277, B = 0.602245584,

P=4, q = 0, a = 1.8,

λ = 21.0, γ = 1.2

The parameters listed above were obtained such that the melting point and the

liquid structure computed by MD simulations for silicon conform to experimental values.

This potential gives the melting point of silicon as 1691K within an error of 20K. which

is very close to the experimental value of 1683K. In addition to this, the diamond

structure is proposed to be the most stable at low pressure. The cut off for this potential is

found to be at a distance 3.77 Å which is between the first and second nearest neighbor distance in diamond silicon.

Compared to experimental values, SW yields a value for the bulk modulus very close to the experimental results. As will be evident in subsequent chapters, SW yields good structure and energetics information of point defects. Also, SW matches the first principles calculations in producing the (100) Si surface,but, fails to model of the the several reconstructions of the (111) surface. Since the SW potential consists of only first and second nearest neighbor terms, it cannot distinguish between the diamond phase and the hexagonal diamond phase. By far, the SW potential is the most widely used potential in simulations of silicon.

3.3 The Universal Potential

To give a better treatment of interactions between atoms at short distances or having higher energies the repulsive part of the two-body term of the SW potential has been modified to link it to the Universal potential. Although there is no sharp demarcation for the validity of the two potentials, this range is chosen to be between a few eV for the potential. In the MDCASK code, the universal potential and the SW potential are connected between the r values in the range $r_1 = 1.2107$ Å and $r_2 = 1.8456$ Å. These r values correspond to a potential energy ≈ 24 eV and the pair part for the SW equal to 0 eV for r_1 and r_2 respectively. A spline is used to connect the two potentials between these two points.

For the total distance range the value of the pair potentials is given by

$$V(r) = \begin{cases} V_{ZBL} & r < r_1 \\ \alpha_0 + \alpha_1 r + \alpha_2 r^2 + \alpha_3 r^3 & r_1 \leq r < r_2 \\ \varepsilon\, f_2(r/\sigma) & r \geq r_2 \end{cases} \qquad (3.16)$$

where $\alpha_0 = 335.0594$ eV, $\alpha_1 = -492.3905$ eV $\overset{\circ}{A}^{-1}$, $\alpha_2 = 244.5280$ eV $\overset{\circ}{A}^{-2}$, and $\alpha_3 = -41.2347$ eV $\overset{\circ}{A}^{-3}$.

3.4 Constant-Temperature MD and the Canonical Ensemble

In a MD simulation, the positions and momenta of all the particles form the phase space. The phase space points constitiute the MD ensemble. An average over phase space gives any desired property of the system. The efficacy of the MD simulations in producing valid results depends on the assumption, from a statistical mechanics perspective that properties or observables are averages over some region of sample space. The transition from a single MD system to an ensemble is based on the quasiergodic hypothesis which states: ensemble averages are equal to time averages, if the average is done for a period of time sufficient to make the average independent of the averaging time [Beeler 76, Heermann 86]. It follows that in order to build statistical ensembles in MD the system must reach an equilibrium. When the mean and variance of a dynamical variable become independent of time equilibrium is attained.

The thermodynamic state of a system is determined from three parameters such as the number of particles, N, the temperature T and pressure, P. The microcanonical ensemble is the regular ensemble in an MD simulation. In this ensemble, the number of particles, N, the volume, V and the total energy E are constant. In this ensemble, the

problem is totally deterministic since no stochastic elements are included excepting for the elements related to the machine round-off errors. This is an isolated system.

In many cases, however, it is interesting to study an ensemble with N, V and T constant or N,P and H constant. Constant temperature calculations are possible in the MDCASK code and two methods of achieving this are highlighted here.

The NVT ensemble is known as the canonical ensemble. In this ensemble, the equations of motion are altered to couple the system to a thermal bath. In this case only the kinetic energy is conserved. The equations of motion are constrained by a stochastic force which simulates collisions with virtual particles. The other means of maintaining the temperature constant is by fixing the kinetic energy of the system. This can be achieved by rescaling the velocities at each time step by a factor $(T/\tau)^{1/2}$ where τ is the current kinetic temperature and T is the desired temperature [Allen 87].

Another means of achieving the canonical ensemble is by using Brownian dynamics. In this technique, the system particles are interacting with a viscous medium. A stochastic force acting on every particle in the computational cell represents the thermal bath. The particles, in this case, are said to obey a Langevin equation of motion in a field force such as

$$m \frac{dv_i}{dt} = F_i + R_i(t) - \beta v_i \qquad (3.17)$$

where βv_i is the friction force acting on the particle, with β being the viscous constant and $R_i(t)$ is a random force that simulates the heat of the particle at the necessary bath temperature. The friction force removes the excess of energy and the random force

maintains the system at the required temperature. The random force must conform to certain rules such as the following:

It has to be zero on the average over long times, i.e.

$$< R(t) > = 0$$

The random force must be uncorrelated at two different times and taking into account the equipartition theorem must obey

$$< R(t) R(0) > = 2\beta kT\delta(t) \tag{3.18}$$

Moreover, in order to get a Maxwellian velocity distribution the random force must be Gaussian distributed as follows:

$$P(R) = \frac{1}{\sqrt{2\pi < R^2 >}} \exp(-R^2 / 2 < R^2 >) \tag{3.19}$$

The variance $<R^2>$ is obtained given the fact that the correlation time for the force is $\delta(t)$ as follows:

$$<R^2> = \beta k_B T/\delta t \tag{3.20}$$

In order to satisfy these conditions, a random number must be generated with mean value zero and variance $<R^2>$.
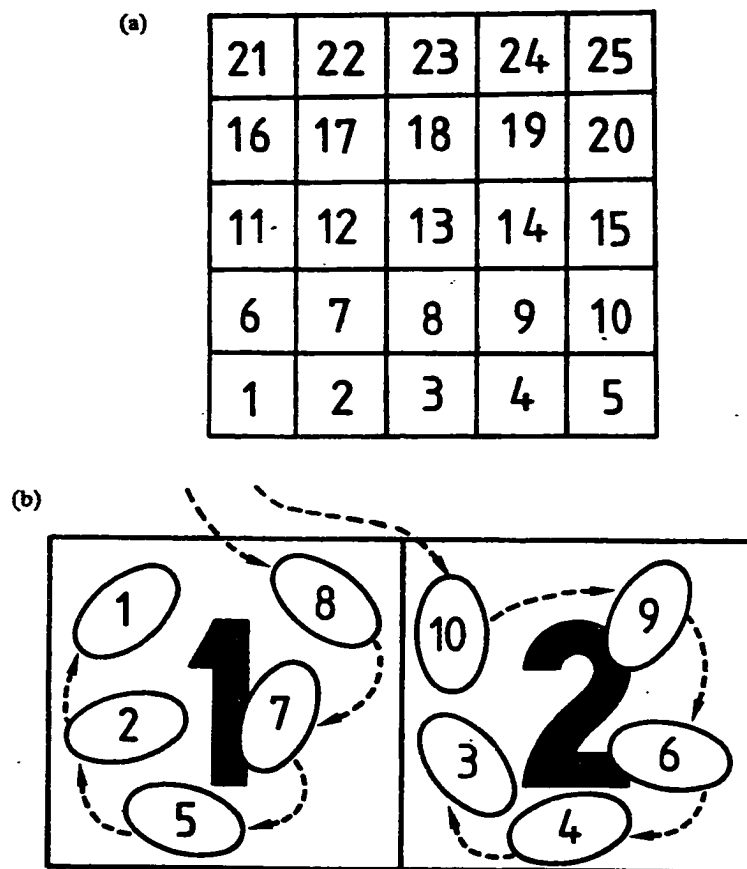
Fig. 3.1 The cell method in two dimensions. (a) The division of the central box into MxM cells where M=5. (b) Close-up view of cells 1 and 2, indicating the molecules and the link-list structure

CHAPTER 4
DIFFUSIVITY OF POINT DEFECTS IN SILICON: A COMPARATIVE STUDY USING THREE DIFFERENT INTERATOMIC POTENTIALS

4.1 Overview of Empirical Interatomic Potentials

Normally, empirical potentials are constructed by first guessing a functional form, based on physical intuition, and then by choosing the parameters to fit *ab initio* energy data . This process is particularly difficult in covalent materials due to the various complex quantum-mechanical effects such as chemical bond formation and rupture, hybridization, metallization, charge transfer and bond bending. There is a large number of potentials for silicon in the literature. Although the successes and failures of the various potentials cannot be attributed to the functional form, it can be concluded that a good functional form is more important than intricate fitting strategies.

As described in the previous chapter, the Stillinger-Weber (SW) potential has only eight parameters fitted to a few experimental properties [Stillinger 85]. This potential has a pair interaction term which has a deep well at the first neighbor distance to account for the fact that there is a strong restoring force opposed to the stretching of the hybrid sp^3 covalent bonds. The three-body term is represented as a product of a radial and an angular function. The angular function has a minimum of zero at the tetrahedral angle suggesting that there is an angular preference of sp^3 bonds. On the other hand, the radial function decreases with distance in order to mitigate the effect of the angular term upon bond stretching. It is also seen that although the various terms lose their relevance for distortions of the diamond lattice leading to the elimination of sp^3 hybridization, the

39

SW potential happens to be the most commonly used potential, mainly due to its simplicity and sound physical content.

The other popular empirical potential is the Tersoff potential, with three versions named T1 [Tersoff 86], T2 [Tersoff 88] and T3 [Tersoff 88]. The T1 version has only six adjustable parameters fitted to a small bulk polytype database. Elastic properties were further improved in subsequent versions by including seven more parameters. The fundamental difference between the Tersoff and SW potentials is that, in the Tersoff potential, the strengths of individual bonds is influenced by the presence of surrounding atoms. The energy is the sum of a repulsive pair term, $\Phi_R(r)$ and an attractive interaction term $p(\zeta)\,\Phi_A(r)$ which depends on the local bonding environment, denoted by a scalar quantity ζ.

$$E = \sum_{ij} [\ \Phi_R(R_{ij}) + p(\zeta_{ij})\Phi_A(R_{ij})\ ] \tag{4.1}$$

$$\zeta_{ij} = \sum_{k} V_3(\vec{R}_{ij}, \vec{R}_{ik}) \tag{4.2}$$

Here, the function $p(\zeta)$ represents the Pauling bond order. The three-body term has a form similar to the one found in the SW potential, excepting for the fact that the angular function may not have a minimum at the tetrahedral angle. It is due to the nature of the angular forces that the Tersoff potential does not have an overall advantage over the SW potential. Most of the potentials in the literature have formats similar to the SW or tersoff formats. However, a number of these potentials have functional forms have restricted validity . As an example, the potential developed by Pearson *et al* [Pearson 84], has no physical motivation and is simply an example in fitting. The authors of this potential use Lennard-Jones two-body terms and Axilrod-Teller three body terms which

has no relevance to covalent materials. As another example, four-body terms are included in some other potentials [Mistriotis 89] with no significant advantage.

The newly developed environment-dependent interatomic potential [EDIP] [Bazant 97] was developed keeping these factors in mind. The premise of the authors was that an improvement over the SW and Tersoff potentials could be achieved by replacing simple functional form with more flexible forms and also by carrying out more involved fitting schemes. Another consideration was that it may be impractical to attempt a simultaneous fit of all important atomic structures (bulk crystalline, amorphous and liquid phases, surfaces and clusters) because different features of bonding are behind different types of structures. The authors also believed that the local bonding environment is important while considering surface and bulk bonding preferences. The goal of the authors was to obtain the best possible description of condensed phases and defects with a theoretically justified functional form

The EDIP potential uses a theoretically motivated functional form which stresses on chemical and physical trends. This functional form is fitted to a small *ab initio* database with only thirteen parameters. The authors of this potential claim that this is a significant improvement over existing models and local structures and extended defects. The authors also claim that this potential describes point defects in the bulk, the concerted exchange path for self-diffusion and elastic properties of bulk silicon. The other claims are that the potential predicts core structures of partial dislocations in the glide set {111} which agrees very well with *ab initio* results.

The functional form of the EDIP potential is as follows:

The configuration energy is expressed as a sum over single-atom energies,

$E = \sum_i E_i$, each containing two and three-body terms,

$$E_i = \sum_{j \neq i} V_2(R_{ij}, Z_i) + \sum_{j \neq i} \sum_{k \neq i, k > j} V_3(\bar{R}_{ij}, \bar{R}_{ik}, Z_i) \qquad (4.3)$$

where $V_2(R_{ij}, Z_i)$ is representative of pairwise bonds between atoms i and j and

$V_3(\bar{R}_{ij}, \bar{R}_{ik}, Z_i)$ represents angular forces between i,j and k centered at atom i. These two

interactions depend on the local environment of atom i through its effective coordination

number given as

$$Z_i = \sum_{m \neq i} f(R_{im}) \qquad (4.4)$$

In this equation $f(R_{im})$ is a cutoff function indicating the contribution of neighbor m to the

coordination of atom i in terms of the separation R_{im}. This function is unity for r<c,

dropping gradually from 1 to 0 between c and a and is 0 for r>a. This is represented as:

$$f(r) = \begin{cases} 1 & \text{if } r<c, \\ \exp(\alpha/(1-x^{-3})) & \text{if } c<r<a \\ 0 & \text{if } r>a \end{cases} \qquad (4.5)$$

where x = (r-c)/(a-c). For r<c a neighbor of atom i is considered a full neighbor, whereas

neighbors between c and a only partially contribute to Z_i. The cutoffs are chosen to

reproduce the important crystal structure coordinations such as

Z_i = 4 for the diamond lattice.

The two-body term includes interactions which are attractive and repulsive:

$V_2(r,Z) = A[(B/r)^p - p(Z)] \exp(\sigma/(r-a)) \qquad (4.6)$

This function has continuous derivatives and goes to 0 at r = a It should be noted that

although this choice is very similar to the SW two-body term, the unique property of this

function is that the bond strength changes according to the local atomic environment. Theoretical calculations show a weakening of the attractive interaction and therefore an increase in bond length for increasing coordination [Bazant 97]. A Gaussian function demonstrates this theoretical dependence such as

$$p(Z) = e^{-\beta z^2} \tag{4.7}$$

The three-body term consists of radial and angular terms and is as follows:

$$V_3(\vec{R}_{ij}, \vec{R}_{ik}, Z_i) = g(R_{ij})g(R_{ik})h(l_{ijk}, Z_i) \tag{4.8}$$

where $l_{ijk} = \cos\theta_{ijk}$ and the radial function is selected to have the SW form,

$$g(r) = \exp(\gamma/(r-a)) \tag{4.9}$$

The angular function which depends strongly on the local coordination by means or two functions $\tau(Z)$ and $w(Z)$ that determine the equilibrium angle and the strength of interaction respectively. By theoretical considerations the following form is proposed:

$$h(l, Z) = \lambda[1 - e^{Q(Z)(1+\tau(Z))^2}) + \eta Q(Z)(1 + \tau(Z))^2]$$

with $w(Z)^{-2} = Q(Z) = Q_0 e^{-\mu Z}$ \hfill (4.11)

The three body angular function becomes flatter as the coordination increases. This is consistent with the desire to have a weakening of the angular forces with increasing coordination. Therefore, to summarize, this version of EDIP has 13 adjustable parameters for silicon which are: A, B, ρ, β, σ, a, c, λ, η, γ, μ, α and Q_0. One of the other features addressed by the authors is that of computational efficiency. The environment terms in the two- and three- body terms necessitate extra iteration loops in the force calculation. Although the three-body interaction requires a four-body loop leading to a more expensive force evaluation compared to the SW potential, this four-body loop needs to be performed only when the atoms are in the range c<r<a. Therefore, the authors

claim, that increased sophistication and realism can be realized with minor computational expense in the EDIP potential compared to the SW potential.

4.2 Diffusivities of Point Defects and Self-Diffusion in Silicon

It has been observed experimentally that the silicon self-diffusion coefficient shows Arrhenius behavior over a wide range of temperatures,

$$D(T) = D_0 \exp(-E_a / k_B T) \tag{4.12}$$

where the activation energy E_a is in the range 4-5 eV. The preexponential factor D_0 is much greater than the corresponding values in typical metals. However, the relative contribution from different mechanisms, such as, from vacancies and interstitials has not been resolved yet. Gosele [Gosele 96] has recently reported that the experimental data for interstitial (I) and vacancy (V) diffusion are as follows:

$$C_I^* d_I = 914 \exp(-4.84 / k_B T) \quad \text{cm}^2/\text{sec} \tag{4.13}$$

and

$$C_v^* d_v = 0.6 \exp(-4.03 / k_B T) \quad \text{cm}^2/\text{sec} \tag{4.14}$$

where d_I and d_v are single defect diffusivities and C^* is the equilibrium defect concentration normalized to 5×10^{22} cm^{-3}. It has also been found [Gosele 96] that $C_I^* d_I$ is a more reliable and accurate quantity- compared to the vacancy quantity -since consistent values are found using two different experimental measurements. Moreover, although

$C_I^* d_I$ is well established, the individual values of the terms d and C* are unknown both for interstitials and vacancies.

In this work the diffusivities $d_{I,V}$ are calculated theoretically using Molecular Dynamics simulations using three different interatomic potentials, namely, the SW, Tersoff and EDIP potentials. The values of the migration energy barriers of the interstitial and the vacancy obtained using the three different potentials determine the validity of the potentials for molecular dynamics simulations.

MD calculates the atomic trajectories of a group of interacting atoms. Since the time step for simulation is rather low (10^{-15} sec), the time duration of simulation is rather low. In this study the diffusion is simulated for 1×10^{-9} sec. The diffusion coefficients are calculated by following the displacements of all the atoms in the system. The accuracy of the results is increased by using high temperature simulations. The computation for single defects and small clusters was done using a computational cell consisting of 216 atoms. A larger computational cell of 1000 atoms used by M. J. Caturla at Lawrence Livermore National Laboratory yielded results almost identical to the results from the 216 atom cell used in this work.

As mentioned earlier, the diffusion coefficients of single point defects and small clusters were obtained not by following the migration of the defect itself but from the displacements of all the atoms in the system. As an example, the diffusion of a single vacancy is made possible by the nearest-neighbor displacements of lattice atoms as they are transported to neighboring vacant sites. In the absence of defects, none of the atoms is moved to a neighboring site. The diffusion coefficients of the point defects can hence be calculated from mean squared displacements over all atoms,

$$D = \sum_i [r_i(t) - r_i(0)]^2 / 6t \tag{4.15}$$

This equation is valid for larger elapsed time t. However, due to the large number of atoms in the computational cell and the short simulation times, the vibrational displacements of atoms around their lattice sites introduces errors in the computation. Specifically, there could be an initial steep rise in the plot of mean squared displacement as a function of time due to the vibrational displacements of atoms around their lattice sites. This possible error can be eliminated by plotting the mean squared displacement,

$\sum_i [r_i(t) - r_i(0)]^2$ as a function of time, and determining the slope of the curve after the

initial steep slope of the curve, due to the vibrational motion, has saturated [Gilmer 95].

A precaution should be taken about the orbital motion of large defect clusters around the cluster's center of mass while calculating the diffusivity of the clusters. Although for long simulation times this should not create any problem since the displacements due to orbital motion saturates, for the short time scales of MD simulations the orbital motion does contribute to the diffusivity values as they take a longer time to saturate than the vibrational motion of atoms. Fig. 4 1 illustrates the technique of determining the diffusivity from the mean squared displacement versus time curve. As is evident from this plot there is a linear relationship between the mean squared displacement and the time variable. This plot is for a fixed temperature. These calculations are repeated for various temperatures. From a semi-log plot of the diffusivity versus 1/kT, where k is the Boltzman's constant and T is the temperature, the migration energy barrier is extracted. This method is adopted for calculating the migration energy barriers using the SW, Tersoff and EDIP potentials. Fig. 4.2 is a plot of temperature dependent diffusivity of the vacancy, the interstitial and the di-interstitial calculated using

the SW potential. Fig. 4.3 and fig. 4.4 are similar plots for calculations done using the Tersoff and EDIP potentials respectively. Fig. 4.5 contains Arrhenius plots of diffusivities of vacancy for the three different potentials in order to show a comparison between the potentials. Figs. 4.6 and 4.7 are similar comparative plots of interstitial and di-interstitial diffusivities respectively for the three different potentials.

Table 4.1 contains the migration energy barriers for the vacancy, interstitial and the di-interstitial for calculation done using the SW, Tersoff and the EDIP potentials. From this data it is evident that the EDIP potential gives an interstitial migration energy value which is vastly lower (0.33 eV)) than that obtained from the SW (0.9 eV) and tersoff (1.1 eV) potentials.

First-principles methods also yield a value for the interstitial migration energy close to that obtained from the SW and tersoff potentials [Blochl 93]. Blochl *et al.* obtained the self diffusion coefficient by combining concentrations and diffusivities . The concentrations were obtained by determining the formation energies using ab initio techniques and formation entropies from the local harmonic approximation [Najafabadi 89]. In this approximation, for a given perfect crystal structure at volume V and temperature T, one can determine the three vibrational frequencies of an atom by diagonalizing the local dynamical matrix for each independent atom in the unit cell. These local frequencies yield the Helmoltz free energy from which all other thermodynamical quantities are determined. They also found that for a migration energy around 1.1 eV for the self interstitial the self diffusion values are in the range of experimental results. This therefore suggests that the migration energy values obtained using SW and tersoff potentials conform to first principles estimates.

The authors of the EDIP potential agreed that there is a flaw in this potential. They calculated the fully relaxed activation pathway between the tetrahedral and hexagonal sites with EDIP. From these calculations they noticed that the interstitial path is unrealistic in many ways. Mainly, the interstitial path has an artificial global minimum

Table 4.1 Migration energy barriers, of vacancy and interstitial calculated for the SW, Tersoff and EDIP potentials, from this work.

Potential	E_M (Vacancy) (eV)	E_M(Interstitial) (eV)
SW	0.436	0.926
Tersoff	0.383	1.1
EDIP	0.203	0.334

between the tetrahedral and hexagonal sites and perhaps also a low activation barrier. The authors attributed this flaw to a careless error that had been introduced into the fitting database. A certain intermediate configuration between the tetrahedral and hexagonal was fitted to the LDA energy of the hexagonal minimum. This in turn decreased the true minimum of energy and also apparently created an invalid global minimum. This lack of validity of the EDIP potential means that this potential cannot be successfully used in studying clustering phenomena.

In order to further investigate the validity of the EDIP potential it would be necessary to calculate the self-diffusion of the interstitial and the vacancy. A comparison of the temperature, at which there is a crossover between the interstitial-dominated to the

vacancy-dominated self-diffusion regime, for theoretical calculations using the EDIP potential and experimental observations would further indicate the validity of the EDIP potential.

A theoretical estimate of the self-diffusion coefficients requires three different calculations: (a) diffusivity prefactor d_0 and migration energy E^M (b) formation energy E_f and (c) formation entropy S_f. d_0 and E^M were obtained using MD with the EDIP potential. The self-diffusion calculations will be complete only when equilibrium concentrations are computed. The formation entropy (S_f) and energy (E_f) of the individual defects are related to the normalized equilibrium concentration of the interstitial and vacancy through the equation

$$C^*_{I,V} = \exp[-(E_f - TS_f)/k_B T] \qquad (4.16)$$

The calculation of formation energy is described in the following section.

4.3 Formation Energy Calculations of Point Defects and the Di-Interstitial

The formation energy of the point defects and the di-interstitial was obtained using the SW and the EDIP potentials. For self-diffusion calculations the EDIP potential was used. For formation energy calculations a computational cell of 1000 atoms was used. The stable structures of the point defects were obtained first by annealing the system containing the defects at arbitrary positions at 1000K for 50 picoseconds. This tempeature would be sufficient to produce several diffusion hops of the defects. Subsequently, the system is cooled to 0 K over a period of 50 picoseconds gradually. This technique is found to give a unique low-energy defect structure independent of the initial structure. The validity of this approach is further corroborated from the formation

energies obtained which were found to be having the same values as those reported in the

literature for the SW potential [Gilmer 95].

4.4 Self-Diffusion Data for the EDIP Potential

Table 4.2 shows the formation energy values obtained in this work using the SW

and EDIP potentials as well as the values obtained from the literature for the Tight

Table 4.2 Formation energies of point defects and the di-interstitial obtained by
simulations

Defect type	SW	TBMD	ab initio	EDIP
Vac.	2.64 eV	3.97 eV	3.65 eV	3.23 eV
Int.	3.65 eV	3.8 eV	3.7 eV	3.43 eV
di-int.	5.7 eV	4.91 eV	-	4.97 eV

The data labeled SW and EDIP are obtained in this work. TBMD values were obtained
from Tang et al. [Tang 97]. ab initio data are from Zhu et al. [Zhu 96].

Binding scheme and ab initio schemes. The self-diffusion data is then computed using the

migration energy barrier values and the formation energy values for the case of the EDIP

potential. In the present work, the formation entropy is not calculated using MD

simulations. For vacancies, Blochl et al. have calculated the formation entropy by means

of the local harmonic approximation and have obtained a value of $S_{fv} = 9$ k_B [Blochl 93].

For interstitials, Tang et al. have fitted $C^*_I d_I$ to the experimental data point at 1250 ^0C and

have extracted the formation entropy to be 11.2 k_B [Tang 97]. $C^*_I d_I$ is given as

$$C^*_I d_I = d_0 \exp(S_{fI}/k_B) \exp[-(E_f + E_m)/k_B T] \qquad (4.17)$$

Similarly the self-diffusion of vacancies is given by

$$C^*_v d_v = d_0 \exp(S_{fv}/k_B) \exp[-(E_f + E_m)/k_B T] \qquad (4.18)$$

Fig 4.8 depicts the Arrhenius plot of the self-diffusion data. From this plot it is estimated that the crossover temperature from the interstitial-dominated to vacancy-dominated self-diffusion regime falls at about $717^0 C$. This temperature value is vastly different from the experimental finding of $1050^0 C$. Therefore this is an additional proof that the EDIP potential is lacking in validity. The SW potential and the Tersoff potential give crossover temperatures of $1152\ ^0C$ and $1082\ ^0C$ respectively which are closer to the experimental value than the value obtained using the EDIP potential.

4.5 Summary

In this chapter an overview of SW, Tersoff and EDIP interatomic potentials was presented. The results of MD calculations of the migration energy of point defects and the di-interstitial were presented. These results show that the EDIP potential yields a migration energy barrier for the interstitial which is much lower than that obtained from SW, and Tersoff. The SW and Tersoff values are very close to that obtained from LDA calculations, thereby implying that there is a flaw in the EDIP potential. The formation energies of the point defects were also obtained by MD simulations using the EDIP potential. From the formation energies and migration energies the self-diffusion coefficient was calculated for the interstitial and the vacancy over a range of temperatures. It was found that the crossover temperature for the interstitials and vacancy self-diffusion coefficients was $717\ ^0C$ whereas the experimental value is $1050\ ^0C$ proving again that the EDIP potential is flawed.
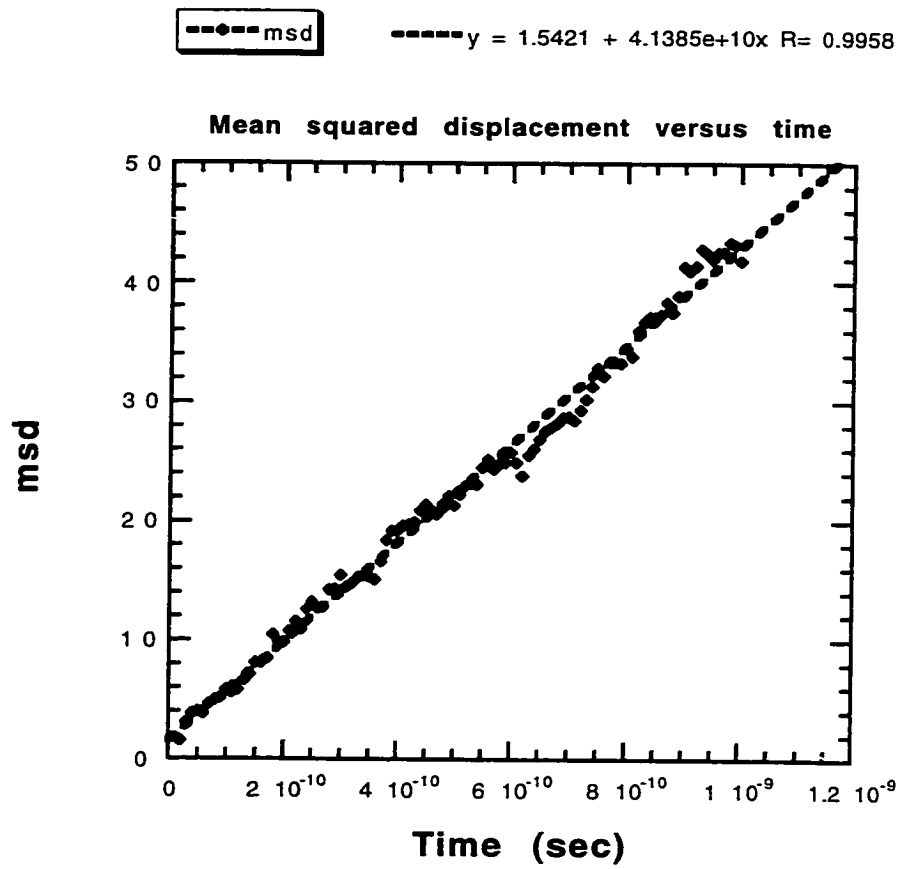
Fig 4.1 Mean squared displacement (msd) as a function of time for interstitial migration using the SW potential. This is for the case of the interstitial at 1450 K
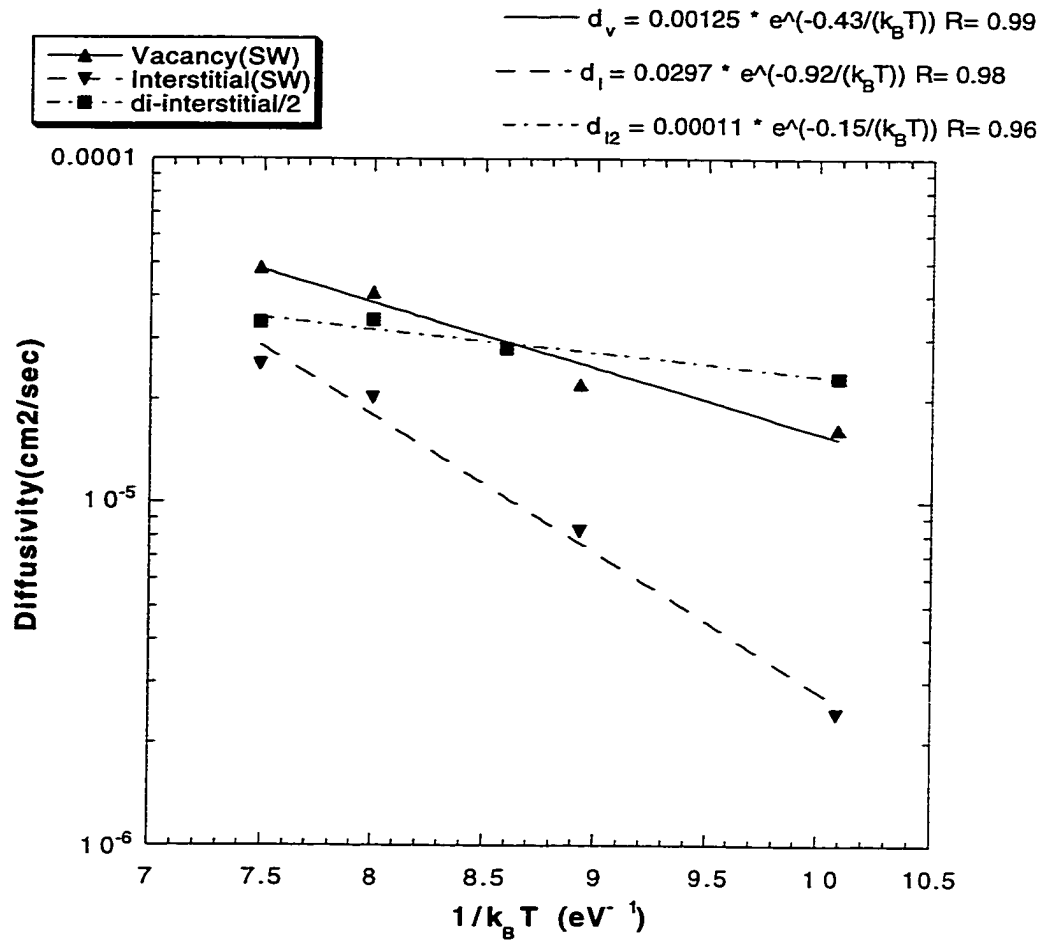
Fig. 4.2 Arrhenius plot of diffusivity as a function of $1/k_BT$ using the SW potential
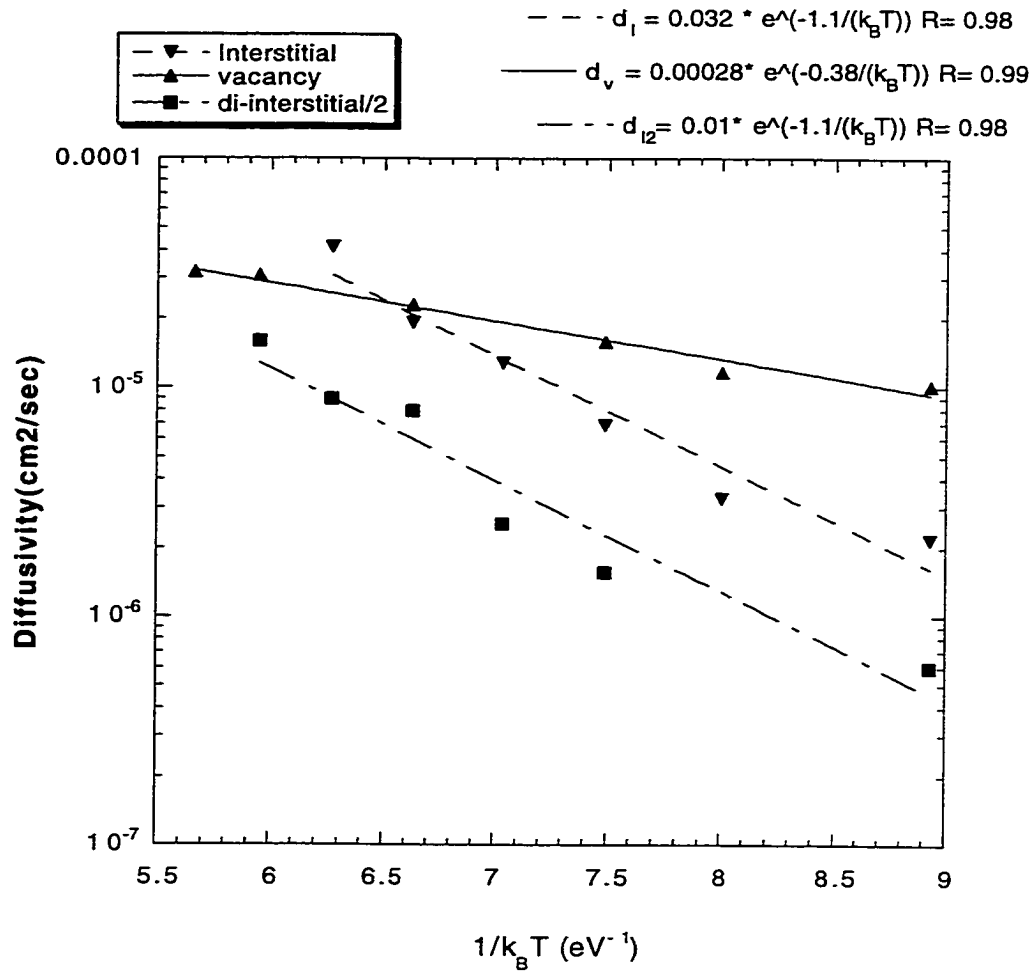
Fig. 4.3 Arrhenius plot of diffusivity as a function of $1/k_B T$ using the Tersoff potential
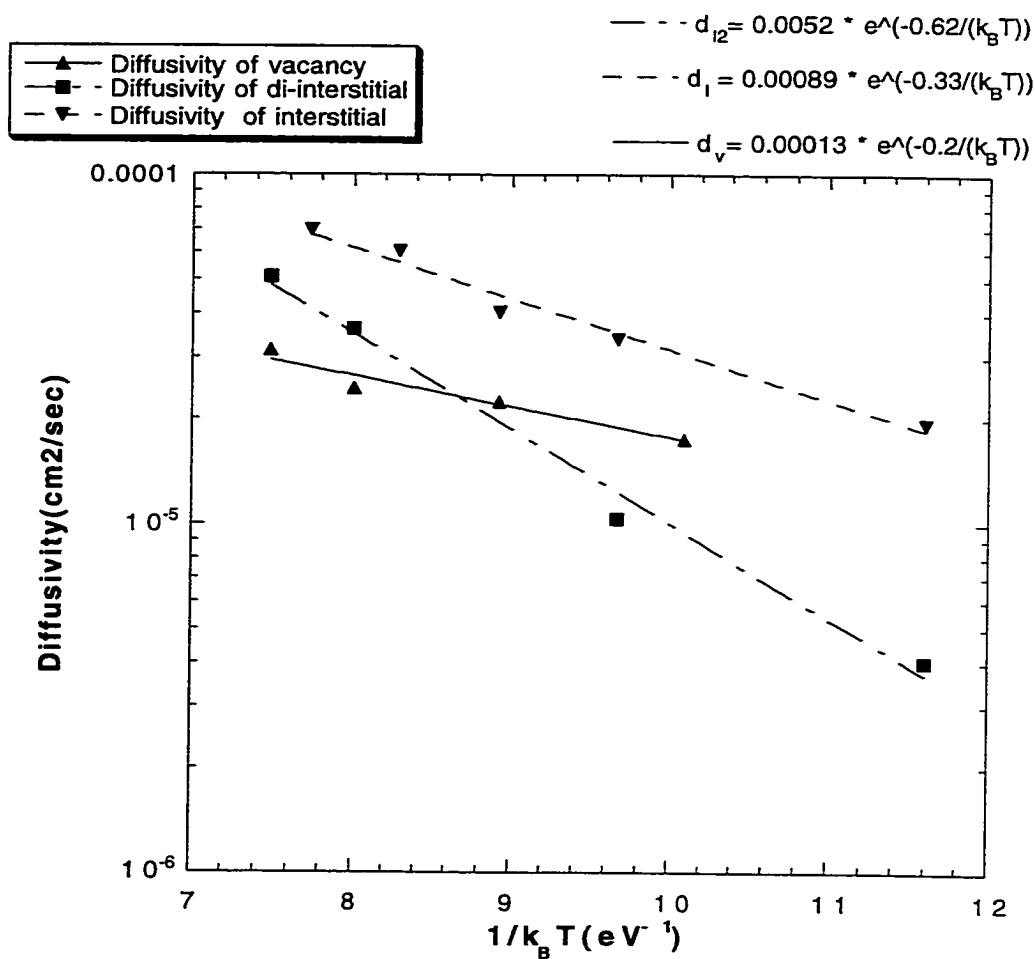
Fig. 4.4 Arrhenius plot of diffusivity as a function of $1/k_BT$ using the EDIP potential
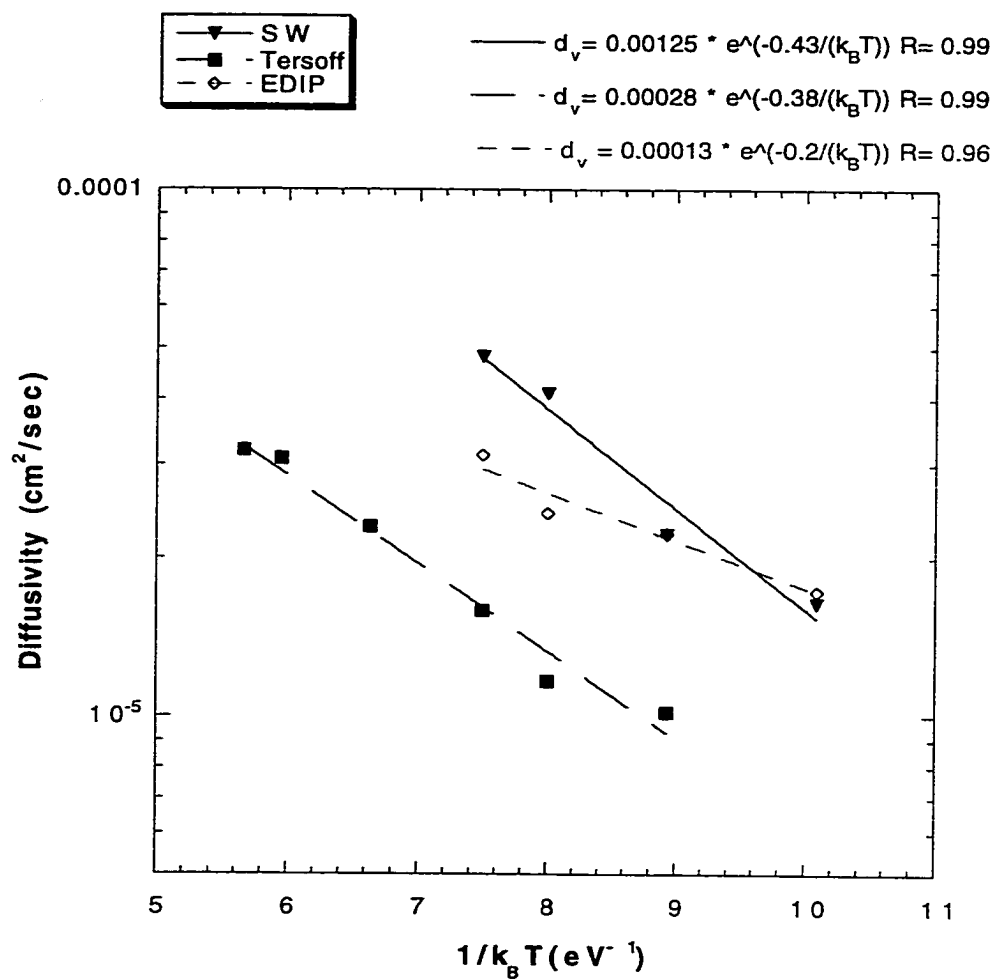
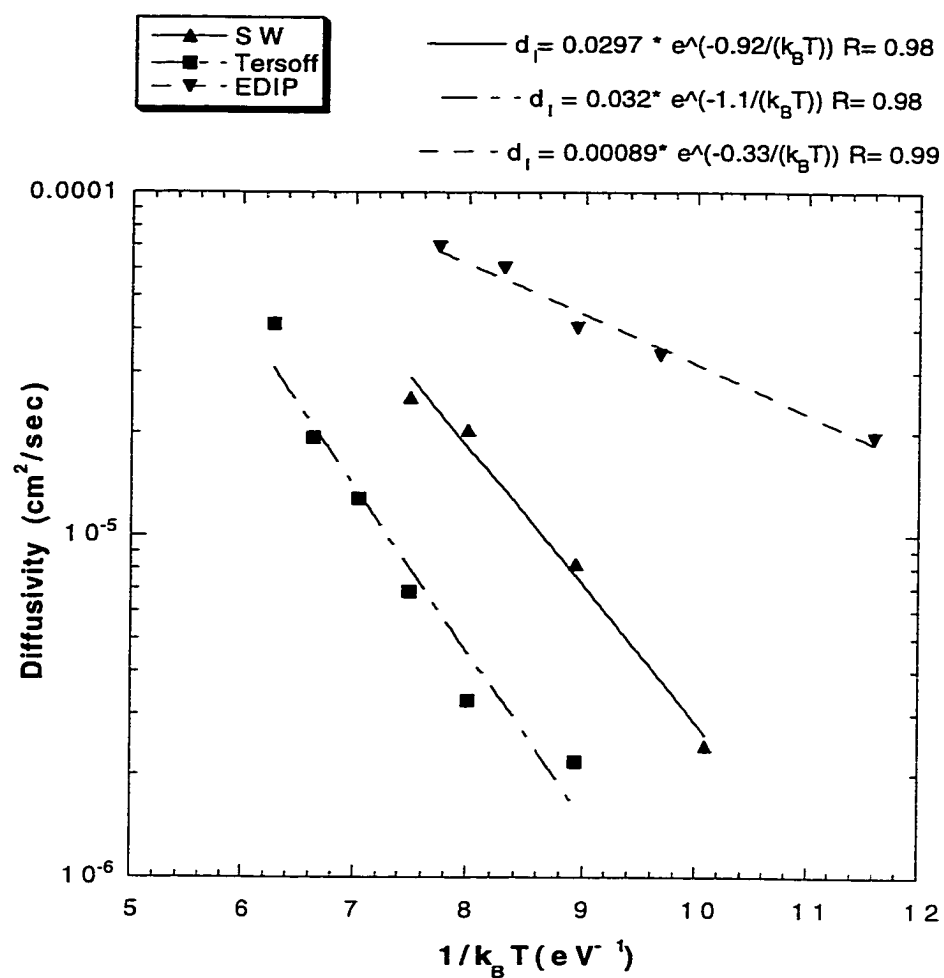Fig. 4.5 Arrhenius plots showing vacancy diffusivity for SW, Tersoff and EDIP potentials

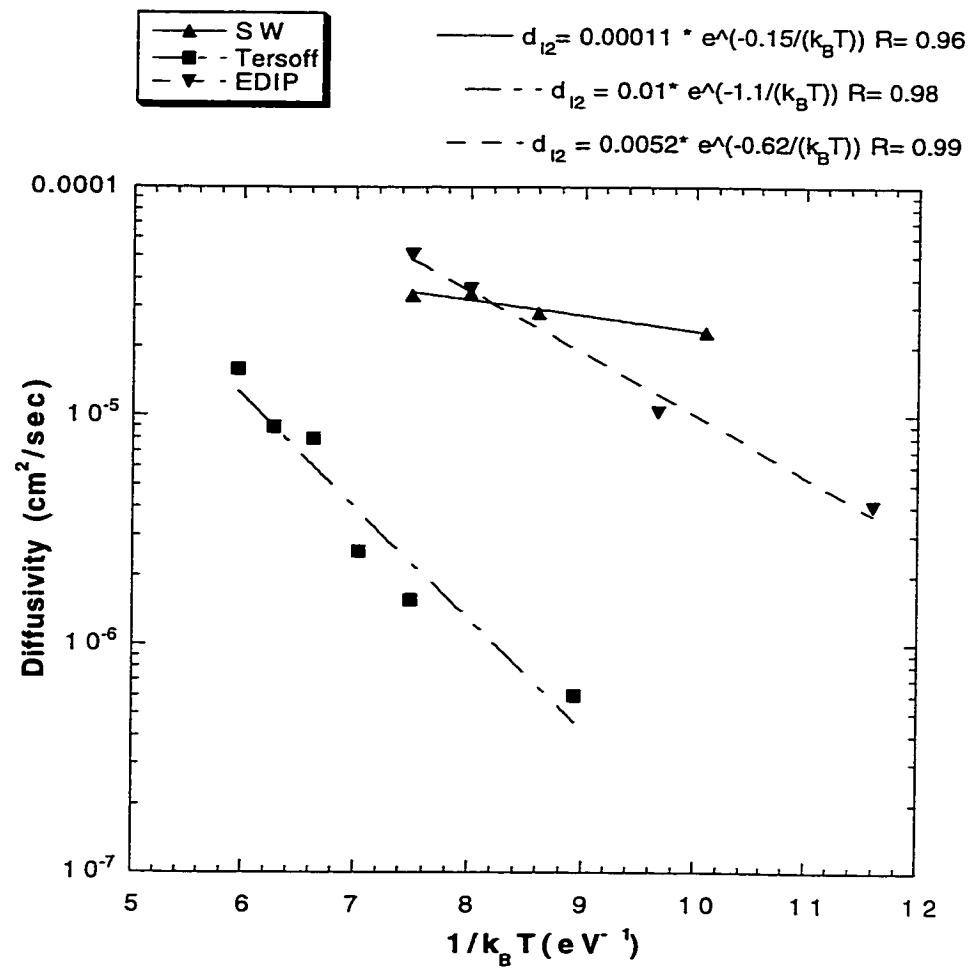Fig. 4.6 Arrhenius plots showing interstitial diffusivity for SW, Tersoff and EDIP potentials

Fig. 4.7 Arrhenius plots showing di-interstitial diffusivity for SW, Tersoff and EDIP potentials
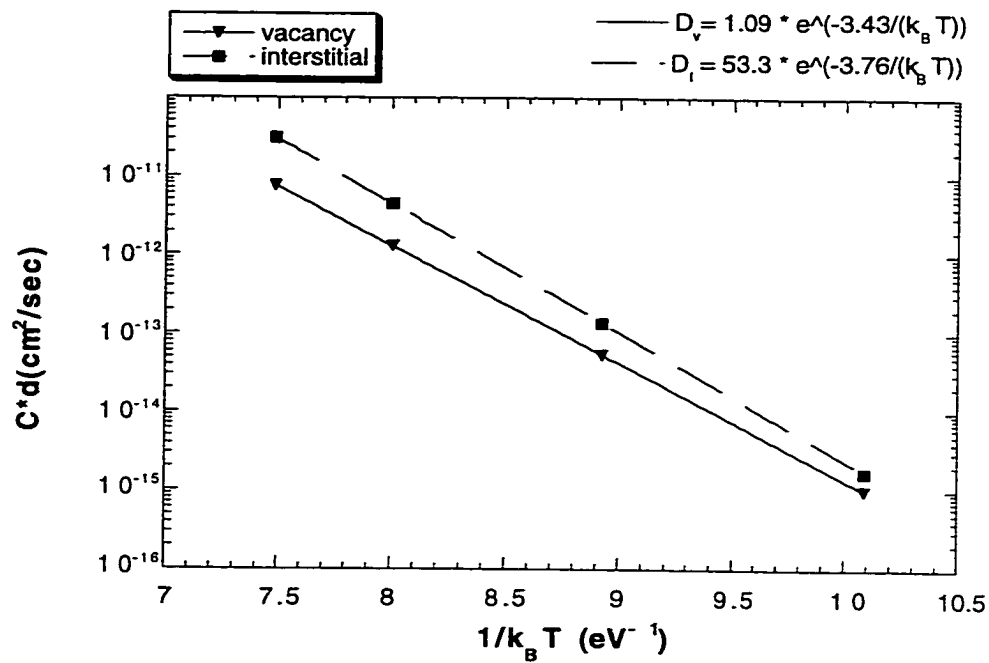
Fig. 4.8 Arrhenius plot of self-diffusion for vacancy and interstitial using the EDIP potential

CHAPTER 5
ENERGETICS OF SMALL SELF-INTERSTITIAL CLUSTERS

5.1 Introduction

It is now well known that self-interstitial atoms in silicon, generated by ion-implantation play a significant role in self-diffusion and impurity diffusion. Due to their high formation energies (3-5 eV) [Fahey 89], self-interstitials. also aggregate to form clusters and extended defects such as the {311} defects. Self-interstitial agglomerates, such as {311} defects have been seen to be involved in the phenomenon of dopant Transient Enhanced Diffusion (TED). This occurs by the injection of interstitials through the dissolution of {311} defects, which were initially generated, upon annealing [Stolk 97]. Moreover, it has been observed that the absolute enhancement and duration of boron TED, which is instigated by interstitial supersaturation, are dependent also on the thermal stability of small interstitial clusters [Zhang 95].

Although there have been numerous studies on obtaining structural information of {311} defects using Transmission Electron Microscopy (TEM) analyses [Eaglesham 94], as well as theoretical studies [Kohyama 92], there is very little information about the structure and energetics of nanometer –size interstitial clusters. In this chapter, the formation energy results of small clusters (size < 10 interstitials), calculated using MD simulations with the SW interatomic potential, will be presented. In addition to this, the binding energy, obtained from the formation energy calculations as well as the atomic models of some small clusters will be presented.

60

5.2 Computational Methodology

Classical MD simulations, using the MDCASK code with the SW potential, are used in this work. Because of the very small time steps involved in these simulations, the total simulation time is limited. In this work, a supercell of 1000 atoms is used. First, the case of a perfect lattice is run by heating the perfect lattice to 1000K for 5 nanoseconds and then cooling the system gradually to 0 K. Next the required number of interstitials is introduced at arbitrary locations. As before, the system is annealed for 5 nanoseconds at 1000 K, and subsequently, it is cooled slowly over a time span of 5 nanoseconds to 0 K. This procedure, of simulated annealing, has the advantage that the atoms will undergo several diffusion hops before attaining the most stable configuration after relaxation.

This ensures that if there is a metastable configuration for the clusters, we can get out of it by quenching the temperature slowly. The method used to do this quench is called Langevin dynamics [Allen 87]. This scheme involves coupling the atoms to a thermal reservoir, so that the temperature remains constant. The program does this in the following way: after the calculation of the force on each atom, there is a term added to that force, which is like a friction force and sets the temperature essentially to 0 K. Then, another term is added, which contains a random number, so that the desired temperature is added to the system. This procedure is done for every time step. The advantage with this method is that we can choose how fast the quench is occurring. In the code, this is done in a subroutine called tfix.f

The input file for the MDCASK code is called mold.in. In mold.in, there are several variables that are related to the procedure described above.

Langevin dynamics:

TEMPCONT NLANGEVIN TEMPFACT

ZTC   XYTC NTCLAYERS

BETAL

TEMPCONT: If this variable is assigned a logical value True, then this temperature control is going to be used.

NLANGEVIN: Determines the number of steps after which the temperature should be rescaled.

TEMPFACT: This variable decides by how much the temperature is going to be rescaled. For example, 0.8 is 80%.

This temperature rescaling can be carried out for either all the atoms in the simulation or for only some of them. The following parameters determine this choice:

ZTC: If true, then the atoms in the Z direction will be scaled.

YXTC: If true, then atoms in the x and y direction will be scaled.

NTCLAYERS: This sets the number of layers of atoms to be scaled. If the box is 10x10x10 and 20 layers are selected, it means that all the atoms in the simulation will be coupled to the reservoir.

Supposing that an interstitial is introduced into the system and the temperature of anneal is set at 1000 K, the code starts with TEMPRQ = 1000 K. If NLANGEVIN = 1000, every 1000 steps the temperature is lowered by 0.8 * TEMP, if TEMPFACT = 0.8 and if the total number of steps is stipulated to be 50000, then the code runs for 50000 steps.

From these simulation results the formation energy of the interstitial is obtained. The formation energy of a cluster is defined as

E(Formation) = Potential energy of the system with the clusters – (N+n)/N * Potential energy of the perfect system.

where N is the total number of atoms in the perfect box, and n is the total number of interstitials. These potential energies are obtained from two output files, namely, mold.out and mdyn.ene

In mdyn.ene we get the difference between the total energy of the system after relaxation and the energy at the beginning. The potential energy of the system with the cluster is = The total energy from mold.out+the energy from mdyn.ene. There are two ways to obtain the formation energy of clusters. In the first method, an original form of the cluster is set up and the temperature is increased and the system is relaxed. However, in this technique, different configurations will have to be tried to find the lowest energy configuration from all of them.

In the second method, the interstitials are introduced at random positions and the system is taken to a high temperature and held for a sufficiently long time for the interstitials to come together and for the cluster. The disadvantage with this method is that the simulation time is very high. In this work this second technique is adopted.

5.3 Results and Discussion

Figure 5.1 shows the plot of formation energy per interstitial versus defect size. Figure 5.2 shows a plot of binding energy versus defects size. From the formation energy per interstitial plot it is evident that there is a significant drop in formation energy as the cluster size increases especially for the first few sizes. This implies that there is a driving force for the aggregation of individual interstitials to form clusters. Unfortunately,

because of computational cost, the formation energy data could not be obtained for a defect size greater than 9 interstitials.

The binding energy plot shows an oscillatory trend with increase in cluster size. These binding energies are used as inputs in Monte Carlo calculations. The binding energies calculated in this work agree well with binding energy values in the literature for cluster size up to 5 interstitials [Jaraiz 96]. Jaraiz *et al.* have tabulated binding energy values for cluster size up to 5 intersititials and the oscillations are seen in their work as well. Their comment was that although oscillations are seen at very small cluster sizes in the binding energy, there should be a convergence of the binding energy to a single value (2.1 eV) at very large cluster sizes.

Figure 5.3 shows the atomic models of a two-interstitial cluster. As is seen from this figure, there is a strain field around the cluster and lattice atoms, in the vicinity of the cluster are displaced from their original locations. Figure 5.4 and fig. 5.5 show the atomic models of a three-interstitial cluster and a seven-interstitial cluster respectively. In these models too the strain field around the clusters are visible from the displacement of lattice atoms near the cluster. In the next chapter, formation energies of small interstitial clusters and those of {311} defects of the same size are compared.

5.4 Summary

In this chapter, the formation energy calculations using MD of small interstitial clusters as a function of cluster size were discussed. It was observed that formation energy per interstitial decreases with increase in cluster size thereby suggesting that there is a driving force for aggregation of interstitials to form clusters. From the atomic models

of these clusters it was evident that clusters have a strain field and lattice atoms near the clusters are displaced from their equilibrium positions.
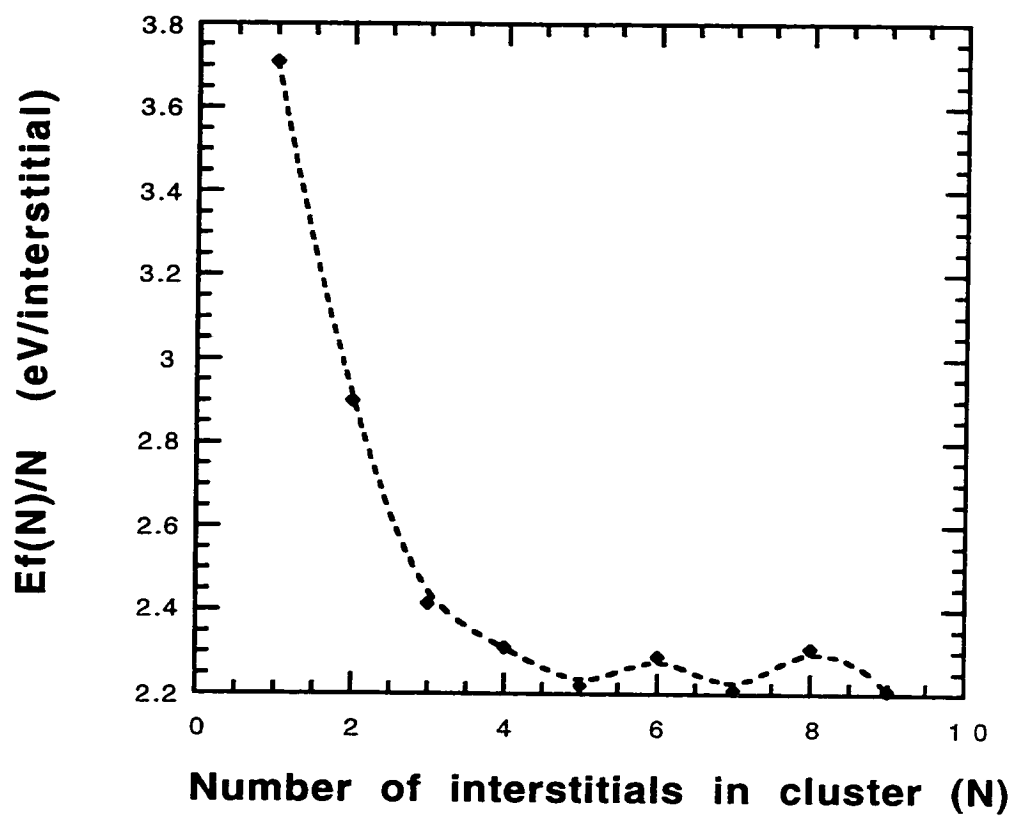
Fig. 5.1 Plot of formation energy per interstitial (Ef(N)/N) versus cluster size (N) for small interstitial clusters.
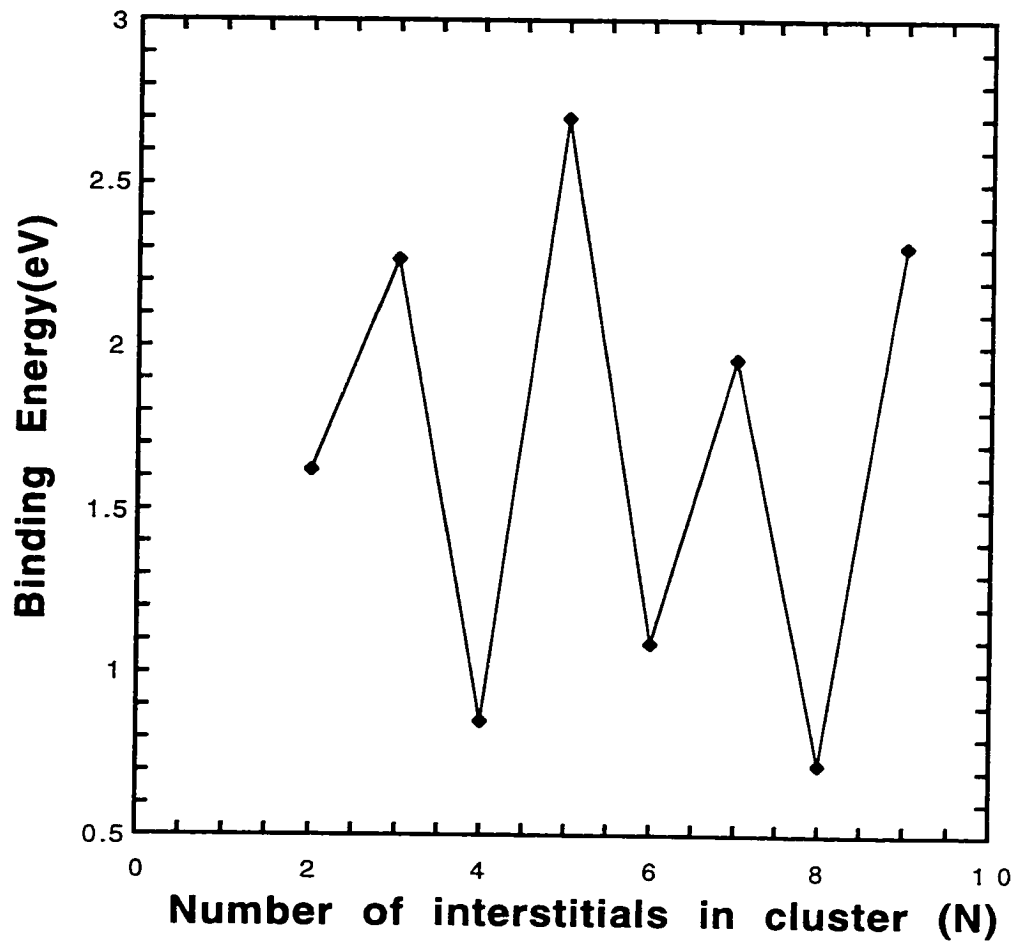
Fig. 5.2 Plot of binding energy versus cluster size for small interstitial clusters.
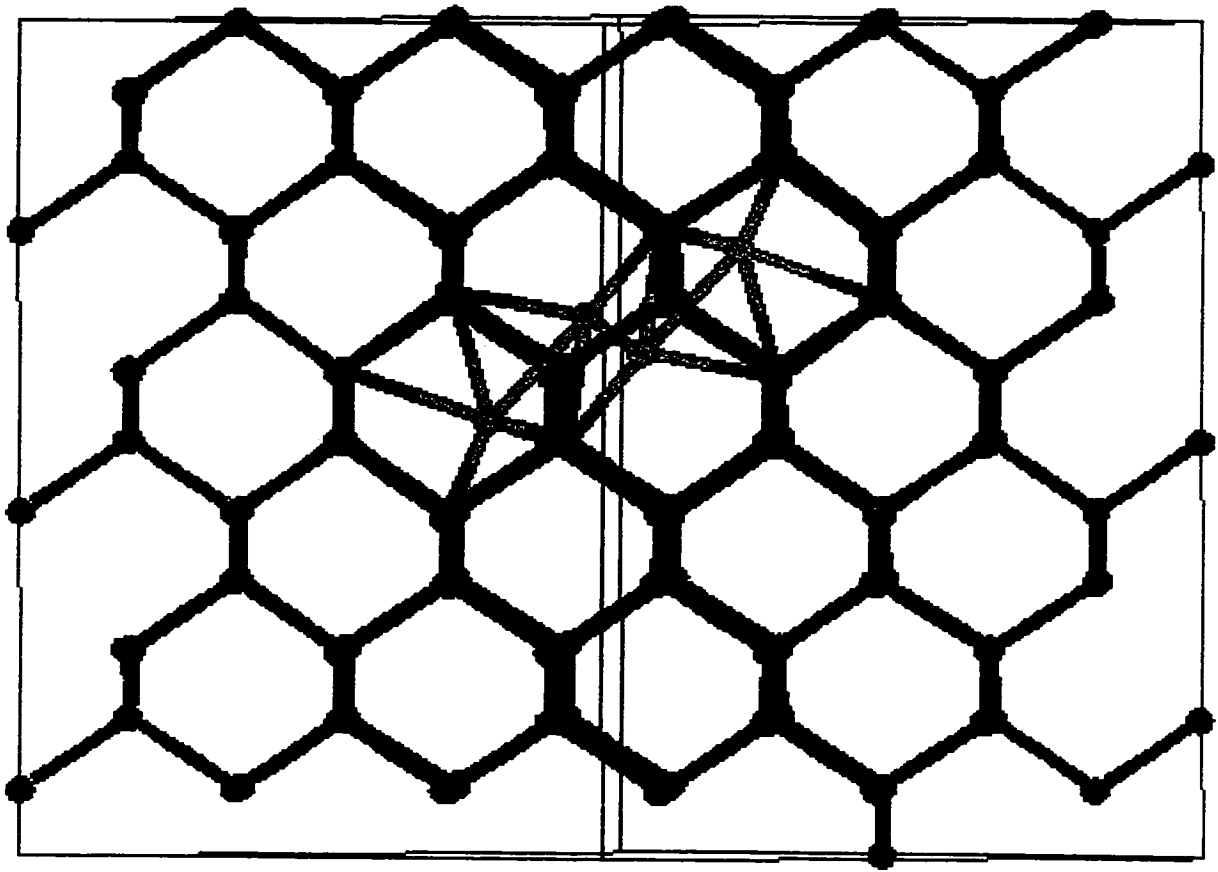
Fig. 5.3 Atomic model of two-interstitial cluster. Gray colors indicate strained atoms.
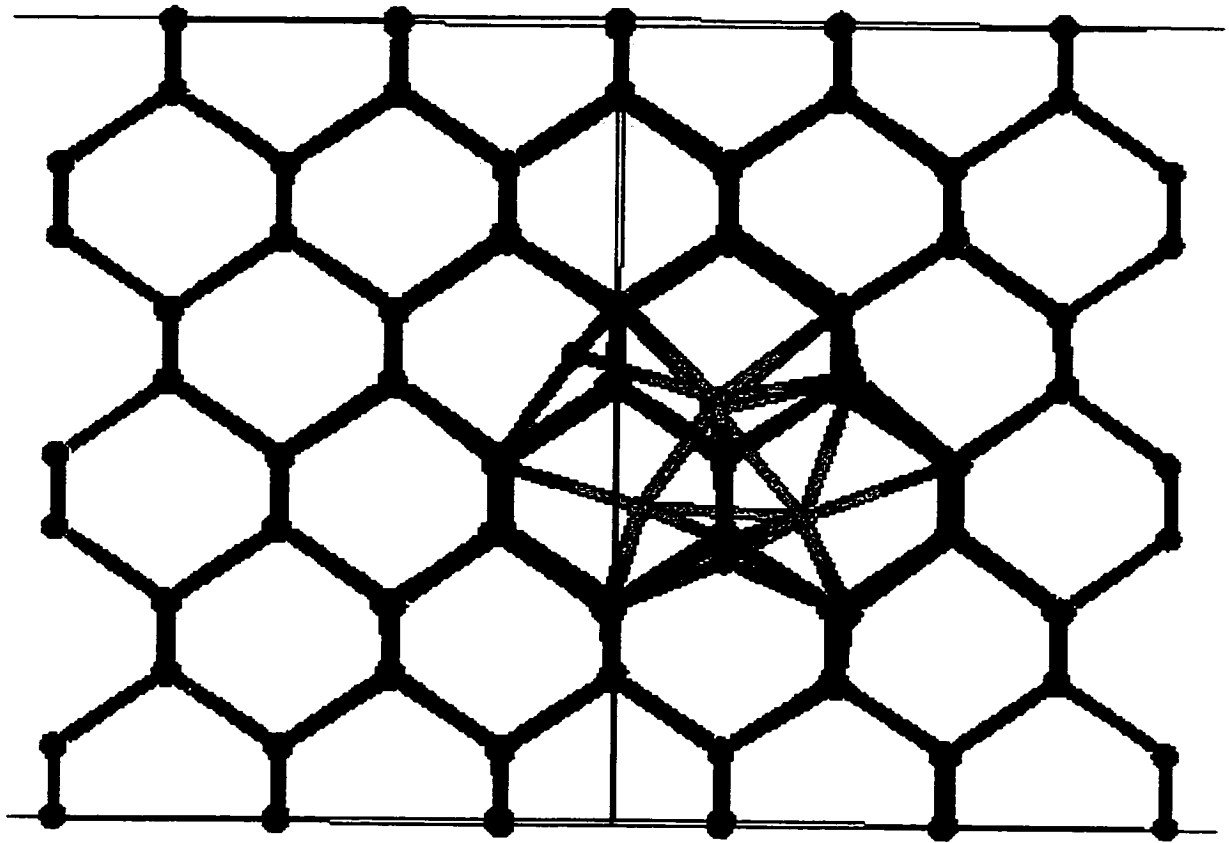
Fig. 5.4 Atomic model of three-interstitial cluster. Gray colors indicate strained atoms
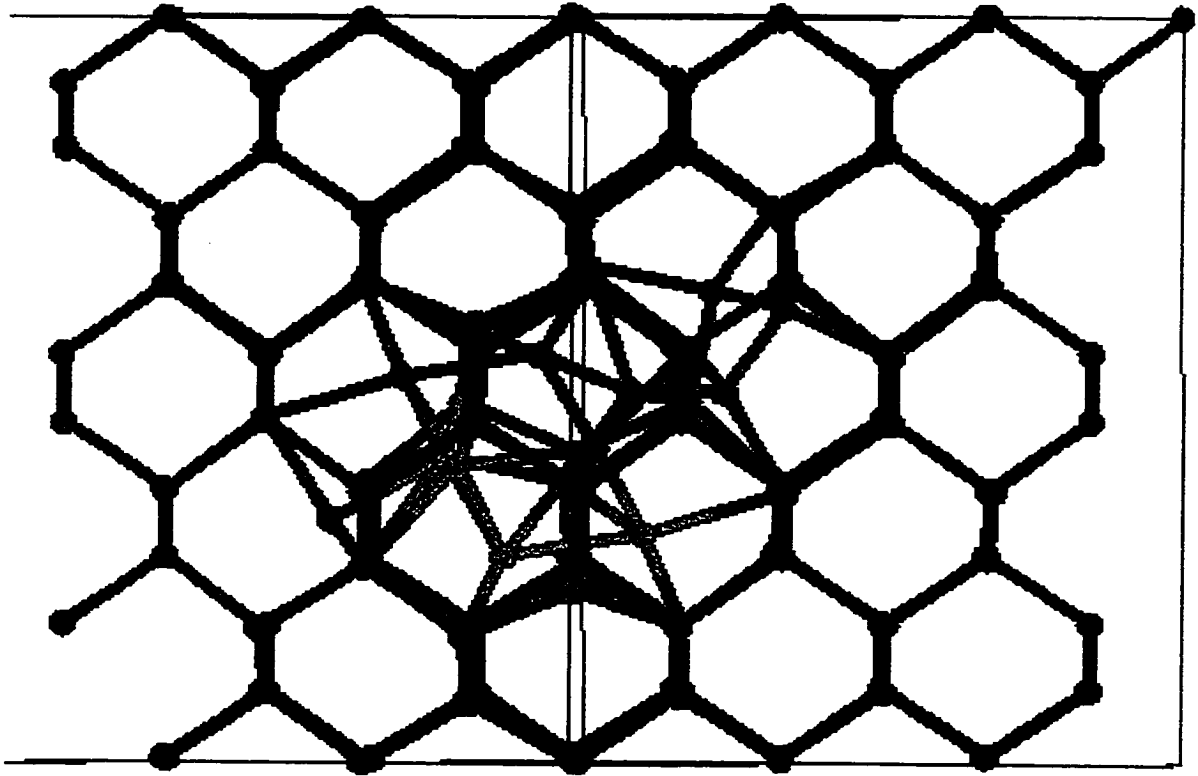
Fig. 5.5 Atomic model of seven-interstitial cluster. Gray colors indicate strained atoms.

CHAPTER 6
FORMATION ENERGIES AND RELATIVE STABILITY OF {311} DEFECTS AND DISLOCATION LOOPS

6.1 Introduction

It has been observed that the duration of boron transient enhanced diffusion

(TED) is exponentially activated with activation energies in the range 1.3-3.6 eV [Zhang

95, Stolk 95a]. The activation energy is related to the creation, diffusion and annihilation

of the Si interstitials and also the interactions between boron and boron and silicon

interstitials. Eaglesham *et al.* [Eaglesham 94] and Stolk *et al.*[Stolk 95a] suggested that

boron TED is a result of emission of Si interstitials from extended {311} defects. These

{311} defects are observed by Transmission Electron Microscopy (TEM) for boron

implantation energies in the range less than 1 KeV [Downey 99] to energies greater than

1 MeV [Washburn 80]. It has also been observed that TED can occur under implant

conditions which do not produce {311} defects [Zhang 95] which implies that there are

submicroscopic interstitial clusters such as boron interstitial clusters (BICs) which release

interstitials.

The {311} defects are elongated along the <011> direction and their width is

along the <233> direction and their habit plane is the {311} plane. A plan view weak

beam dark field TEM image of the {311} defects is shown in fig. 6.1 and a high

resolution cross sectional TEM image is shown in fig. 6.2 [Li 2000]. As is evident from

these images the {311} defects are rod-like and they are composed of chains of

interstitials extending longitudinally along the <011> direction, arranged laterally along

71

the <233> direction, and they lie on the {311} plane. There have been very few investigations in the literature on the energetics of {311} defects with due consideration being given to the growth in width of the {311} defects.

Another aspect of the {311} defects is that these rod-like defects unfault into dislocation loops upon annealing at a high temperature. It has been observed by TEM that concomitant with the dissolution of the {311} defects some small loops grow in size [Wu 77]. Similar connection between the dissolution of the {311} defects and the growth of loops has been observed by other groups [Tan 81]. Recently, Li and Jones have shown through TEM studies that sub-threshold dislocation loops nucleate from {311} defects by unfaulting of the latter [Li 98]. This work involved *in situ* annealing plan-view Transmission Electron Microscopy samples in a TEM. It was observed that after initial 5 minutes of annealing a dense combination of both {311} defects and small subthreshold dislocation loops was found. Subsequently, when the sample was annealed further the {311} defect density decreased rapidly and the loop density increased. The time evolution of 500 {311} defects was monitored. From this scrutiny it was observed that the unfaulting of a {311} defect was the source of every subthreshold loop.

Robertson *et al.* have observed the evolution of both {311} defects and dislocation loops for amorphizing implants, in the end-of-range damage region by *ex situ* TEM [Robertson 2000]. The post-implant anneals were carried out in a furnace at 750^0 C for times ranging from 10 to 370 minutes. It was seen that {311} defects were the preferential sites for dislocation loop nucleation. However, it was also observed that 45% of the loops had nucleated by 10 min at 750^0 C.

In this chapter a comparison is made between the formation energy per interstitial of small clusters and {311} defects. Tight-binding calculations performed recently indicate that infinitely extended (110) interstitial chains have a formation energy per interstitial of 1.7 eV [Kim 97]. However, the formation energy per interstitial of small chain sizes are found to be very large indicating that this structure is not suitable for describing the early stages of {311} nucleation.

Further, tight-binding calculations have shown [Bongiorno 99] that there exist alternative interstitial-cluster configurations, which, at sizes less than 10 interstitials, have formation energy per interstitial values lower than that of the (110) interstitial-chain. Therefore, it can be concluded from this data that small clusters are not direct precursors of the {311} defects and that a structural transformation should occur at some stage of the growth of these defects. In addition to this, deep level transient spectroscopy (DLTS) analysis has shown that changes occur in the electrical signatures during the transition from interstitial clusters to {311} defects [Benton 97].

More recently, Coffa *et al.* [Coffa 2000] have used photoluminescence and transmission electron microscopy (TEM) analyses to study the transition of small interstitial clusters into {311} defects. From their study they conclude that a structural transformation accompanies the transition from interstitial-cluster to {311} defects.

Eaglesham *et al.*, through cross sectional high resolution electron microscopy (HREM), reported agreement with the generally accepted structure of {311} defects consisting of chains of interstitials parallel to the <011> direction and lying on the {311} habit plane with the chains arranged laterally along the <233> direction [Eaglesham 94]. Eaglesham's work also found that, during Rapid Thermal Anneal (RTA), when the length

is measured from plan-view images and the width is measured from HREM, the width was found to be independent of anneal time and the size variations were increases in length only. This indicates that there is a saturation of width after a certain time of growth of the defect.

In the work of Cuendet *et al.*, which was Monte Carlo simulation work [Cuendet 95], the issue of elongation and broadening of the {311} defect has been examined assuming infinitely long stacking fault (SF) ribbons for elongation only and SF loops for both lengthening and broadening. The defect formation energies for defect size corresponding to 60 interstitials are in actuality values of infinitely long ribbons of a particular width. It was also noticed in the work of Cuendet *et al.* work that after the ribbon is 10 dimers long, the formation energy per interstitial is almost constant. It was observed that this formation energy decreases as the width widens. However, in this work, the simultaneous growth in length and width was not studied since an infinitely long ribbon was assumed for all the widths studied.

Gencer and Dunham [Gencer 97] have developed a model for calculation of the kinetic growth rate for {311} defects. In their model they have assumed that {311} defects have a rectangular shape and that the {311} defects grow primarily in their length. In their work it was assumed that the {311} defects have a maximum average width of about 5nm. It was also stated in this model that it would be unreasonable to assume that the width is always 5nm, thereby larger than their length(l) for l < 5nm. It was therefore concluded that the width (w) may be expressed as w = min(l,5 nm). This satisfies the condition that l is always greater than or equal to w and that w=5 nm for

large sizes which can be observed under high-resolution TEM. Here again, the evolution

of both length and width with increase in defect size was ignored.

Hobbler and Rafferty [Hobler 99] have developed a model for {311} defect

evolution based on the rate equations approach. In their work the strain energy of the

{311} defect is calculated within the framework of the theory of dislocations in isotropic

continua as a special case of piecewise straight dislocation configurations. The strain

energy consists of the self-energies of the four dislocation segments (two long edges

along the sides and two short edges along the ends) and also the interaction energies of all

pairs of these segments. From this expression, the variation of the strain energy per atom

is obtained as a function of defect size (the number of interstitials) for 2 to 6 chains wide.

The results thus obtained seem to agree with Cuendet's results excepting at the smallest

sizes where the continuum approach is not valid.

In the work of Kim *et al.* [Kim 97] tight-binding calculations were carried out to

study the structural properties and energetics of extended {311} defects based on their

dimensions and interstitial concentrations. Their finding was that interstitial chain

structures along the <110> direction are energetically more favorable than isolated

interstitials. They also found that interstitial chains are basic building blocks of the

extended {311} defects. They suggested that the extended {311} defects are formed by

condensation of the interstitial chains side by side in the <233> direction. However their

conclusion was that the growth of {311} defects would occur first by elongation of

interstitial chains along the <011> direction followed by an increase in width by the

capture of interstitial chains alongside the <233> direction. They did not determine the

progress of defect growth both longitudinally and laterally at the same time. Therefore, in

their work, they did not observe the ultimate saturation in width which is observed experimentally. Nevertheless the interstitial configuration developed by them for simulation purposes is found to be valuable for carrying out conjugate gradient calculations as part of this thesis.

From the preceding discussion it is evident that various groups have tried to examine the morphological changes in {311} defects with increase in defect size. Many assumptions have been made by these groups in studying the energetics of {311} defects. However, no attempt has been made, through atomistic simulations, to elucidate the simultaneous increase in width along with length as the defect grows. It has been observed experimentally that as the defect grows in length there is initially a growth in width also. However the width-wise growth is not indefinite and a saturation is observed in the width after a certain size. The width has been observed to grow to approximately 60 Å before any further growth stops [Li 2000].

In this work, for the first time, through simulations, the stability of the {311} defects has been determined, depending on the length and width of the interstitial chains that constitute the defect. An attempt has been made to relate the simulation results to experimental evidence. An analysis has also been done, through simulations, of the relative stability of {311} defects and perfect dislocation loops. The methodology of simulations has been the Conjugate Gradient method using the Stillinger-Weber interatomic potential.

6.2 Computational Details

As mentioned in previous chapters, the Stillinger -Weber (SW) interatomic potential is, by far, the most widely used interatomic potential for silicon and therefore is

the potential of choice in this work. The Conjugate Gradient technique is used in this investigation. This technique is also called Molecular Statics and unlike in Molecular Dynamics(MD) the trajectories of atoms are not monitored. The energy minimization is carried out at 0 K. Essentially the system is relaxed at 0K by minimizing the potential energy function. The computational time is vastly less than the MD technique and therefore large systems can be used in this technique.

6.2.1 The Mathematics Behind the Conjugate Gradient Method

The case of calculating, at a given N-dimensional point, not just the value of a function f(P) but also the gradient $\nabla f(P)$ has to be considered first. If the gradient is not used N^2 separate line minimizations have to be made in calculating the function minimum, each requiring a few function evaluations. Now each evaluation of the gradient will bring N new components of information. If used judiciously, we need to make only of order N line minimizations.

A factor of N improvement in computational speed in not necessarily implied. As a rough estimate, the calculation of each component of the gradient takes about as long as evaluating the function itself. In that case there will be of order N^2 equivalent function evaluations both with and without gradient information. Even if the advantage is not of order N, it is quite substantial. This is due to the following reasons: (a) Each computed component of the gradient information will not just save one function evaluation but a number of them, equivalent typically to, a whole line minimization. (b) There is usually a high degree of redundancy in the formulas for various components of a function's gradient: if this is the case, especially, when there is also redundancy with the calculation

of the function, then the calculation of the gradient may cost significantly less than N function evaluations.

However, it is erroneous to assume that any reasonable way of incorporating gradient information should be about as good as any other. The steepest descent method is an example of this not very good algorithm. The steepest descent method starts at a point, say P_0, and as many times as necessary moves from point P_i to the point P_{i+1} by minimizing along the line from P_i in the direction of the local downhill gradient $-\nabla f(P_i)$. The method will perform many small steps in going down a long, narrow valley, even if the valley is a perfect quadratic form. It may be expected that the first step would take us to the local minimum and the subsequent step would be down the long axis of the valley. Since the new gradient at the local minimum point of any line minimization is perpendicular to the direction just traversed, with the steepest descent method, a right angle turn must be made which does not, in general, take us to the minimum of the function.

What is really required is to travel not down the new gradient, but rather in a direction that is somehow conjugate to the old gradient, and as far as possible, to all the previously traveled directions. Methods that achieve this construction are called conjugate gradient methods. If a function $f(x)$ can be approximated as

$$f(x) = c - b.x + (1/2)\, x.A.x \tag{6.1}$$

where the matrix A whose components are the second partial derivative matrix of the function is called the Hessian matrix of the function at some particular point P. Using this approximation of equation (6.1), the gradient of the f is calculated as

$$\nabla f = A.x - b \text{ and } \delta(\nabla f) = A.(\delta x) \tag{6.2}$$

This implies that the function will be at an extremum at a value of x obtained by solving A.x = b. Suppose that we have moved along some direction u to a minimum and now decide to move along some new direction v. Then, the condition that motion along v not spoil our minimization along u is just that the change in the gradient be perpendicular to u. This is the basis for the conjugate gradient technique. From equation (6.2) this is given as follows:

$$u.\delta(\nabla f) = u.A.v = 0 \tag{6.3}$$

When equation (6.3) holds for two vectors u and v they are said to be conjugate. When this equation holds pair-wise for all members of a set of vectors, they are said to be a conjugate set. If we carry out successive line minimization of a function along a conjugate set of directions, then we need not redo any of those directions. If a direction set of N linearly independent mutually conjugate directions is created, then, one pass of N line minimizations will put it exactly at the minimum of a quadratic form such as that given by equation (6.1).

6.2.2 Interstitial Configuration for Calculations

In this work a 27000 atom computational cell was used. This large cell size ensures that the lattice displacement field created by the relaxed extended defects is contained within the cell. For {311} defects, the interstitial configuration used here is similar to that used by Kim *et al* [Kim 97]. This model is illustrated in fig. 6.3. The interstitial chains constituting the {311} defect are extended along the <011> direction, laterally along the <233> direction and the chains lie on the {311} plane. The adjacent interstitial chains are separated from each other by a distance of $a \dfrac{\sqrt{11}}{2\sqrt{2}}$ where a is the lattice parameter. This configuration is then relaxed using the conjugate gradient method

with the SW potential. As a consequence of this relaxation, the formation energy of the {311} defects is obtained as a function of the number of interstitials in the defect. Calculations are done for different number of chains up to a configuration five chains wide. Similarly, the interstitial configuration of the perfect dislocation loop with Burgers vector a/2<110> is created and, subsequently, the loop configuration is relaxed using the conjugate gradient technique to yield formation energies for varying loop size.

6.3 Results and Discussion

First, fig. 6.4 is a plot of the formation energies of small clusters and {311}s of the same size and it shows the difference between the formation energies of both types of defects. The cluster formation energies were obtained in the previous chapter from molecular dynamics calculations and the {311} formation energies are obtained in this chapter from conjugate gradient calculations. Thus, these results are similar to those obtained from tight-binding results mentioned in a previous section of this chapter [Bongiorno 99]. It may be concluded that the small interstitial clusters are not direct precursors of {311}s and that clusters undergo a structural transformation during their growth before they form {311} defects.

The total formation energies for the {311} defects obtained by the Conjugate Gradient method is plotted as a function of defect size in fig. 6.5. It is evident from this plot that as the defect size increases, the least energy configuration has progressively increasing widths. This trend is shown for the first four chains only. The five-chain wide defect has a higher formation energy compared to the four-chain defect for the defect sizes accessible from this simulation. However, a closer inspection of the data seems to suggest that the five-chain defect will become more stable than the four-chain wide

defect at a larger defect size. Moreover, it is also indicated from this plot that the total formation energy varies almost linearly with defect size.

Figure 6.6 shows the formation energy per interstitial of the {311} defect as a function of the defect size for different number of chains that constitute the defect. This plot indicates that, for the defect sizes studied, the formation energy per interstitial decreases as the defect size increases. This suggests that there is a driving force for defect growth. Moreover, as in fig. 6.5, the trend shown is that the most stable defect width (number of chains) increases as the defect size increases. However, it is also seen that this increase in defect width does not continue indefinitely since the five-chain wide defect is less stable than the four-chain wide defect. Therefore, there seems to be a saturation in the defect width with increasing defect size.

Figure 6.7 illustrates this point further. It is a plot of the formation energy per interstitial as a function of width (number of chains) for a defect size of 30 interstitials. It is seen in this plot that for this defect size of 30 interstitials the most stable defect has a width of 3 chains. Also, the slopes of this curve on either side of this minimum point are different. On the right of this minimum the slope is much smaller than that on the left. This implies that the width is beginning to saturate as the defect size increases. This agrees well with our earlier conclusion that the width does not increase indefinitely with increase in defect size.

It has been observed experimentally [Li 2000] that the average width of the {311} defect initially increases with average length and then saturates at a value of around 60 Å. This observation was made using cross-sectional HREM. This trend is in accordance with the energetics calculation done in this work. Fig. 6.8 is a plot of {311} width versus

{311} length observed experimentally [Li 2000] as well as a length to width correlation obtained from these simulations. In order to obtain the average length for each width from the simulation data, a certain width size is chosen and the average defect size during which this width is most stable is measured from the energetics plot (fig.6.6). Upon dividing the average size by the number of atoms in width the average number of atoms in length is obtained. From this the average length of the defect is estimated using the model of Kim *et al.* [Kim 97] which is discussed in section 6.2.2. This data is computed for three chain-wide and four chain-wide defects and shows a direct correlation of length versus width. In the plot of experimental data the saturation of the width is evident. In order to confirm the validity of the trends seen from the atomistic simulations presented in this thesis, a calculation was done based on dislocation theory of the width of the stacking fault defect. This calculation was done as follows:

The maximum separation between two partial dislocations is dictated by the stacking fault energy of the stacking fault separating the two dislocations. The maximum width of the stacking fault is given as w in the following equation:

$$\mu b^2/(2\pi w) = \gamma \qquad\qquad (6.4)$$

where μ is the shear modulus of silicon ($\mu = 6.5 \times 10^{10}$ Pa), b is the length of the Burgers vector (b = 0.1071 nm), and γ is the stacking fault energy in silicon ($\gamma = 60$ mJ/m^2) . From this calculation the width of the stacking fault, w = 19.8 Å. This is in agreement with the width obtained using atomistic simulations which has a value of 20 Å.

83

The driving force for the formation of defects such as the {311} defects and dislocation loops is the minimization of the free energy of the system. The free energy of a defect of size n is given by

$$\Delta G_n = -nkT \ \ln(C_I/C^*) + \Delta G_n^f \tag{6.5}$$

Here, C_I/C^* is the initial supersaturation of interstitials in the lattice and ΔG_n^f is the formation energy of defect of size n. C^*, the equilibrium concentration of interstitials, is calculated as described in chapter 4 using the interstitial formation energy (for the Stillinger-Weber interatomic potential) and formation entropy. These calculations are done at 750 ^{0}C. Defect formation energy is obtained from conjugate gradient calculations as described in previous sections of this chapter. Formation energy data is available for both {311} defects and perfect dislocation loops through conjugate gradient calculations. Plots of the free energy, ΔG_n, as a function of defect size n yield nucleation energy barrier values and critical nucleus size values for the nucleation process.

Figs. 6.10-6.15 show plots of free energy versus defect size for {311}s and perfect loops at various doses. The interstitial concentration (C_I) is obtained from supersaturation values (C_I/C^*). The value of C^* is estimated by the technique used in chapter 4. The formula for estimating C^* is as follows:

$$C^* = 5 \times 10^{22} \ \exp[-(E_f - TS_f)/k_BT] \ /cm^3 \tag{6.6}$$

where E_f is the formation energy of the interstitial which is obtained from molecular dynamics simulations as described in chapter 4 and T is the absolute temperature. The formation entropy (S_f) is estimated by the approach adopted by Tang et al. [Tang 97] as described in chapter 4. The value of C_I is obtained by multiplying the supersaturation

Reproduced with permission of the copyright owner. Further reproduction prohibited without permission.

(C$_I$/C*) by C*. The value of the implant dose ϕ is estimated by using the following expression which relates dose to peak concentration, in this case for a self implant

$$C_I = (0.4 \times \phi)/ \Delta R_p \qquad (6.7)$$

where ΔR_p is the ion projected straggle for silicon ions which is almost equal to that of phosphorus ions which in turn is available in textbooks on silicon processing. From these plots it is evident that, around a dose of 1.2×10^{12}/cm^2, free energy curves for the {311} defects begin to roll over indicating that the {311} defects are beginning to nucleate. Also from these plots, considering the nucleation barrier, at a dose of around 8×10^{13}/cm^2, there is a cross-over from {311} defects to loops as far as stability is concerned. This is illustrated in fig. 6.16 where the barrier height is plotted as a function of implant dose. However, it should be noted that the critical nucleus size of {311} defects becomes lower than that of the loops as the dose increases beyond 1×10^{14}/cm^2 and the barrier heights are not vastly different when the dose increases beyond 1×10^{14}/cm^2. It may therefore be inferred that the nucleation of {311} defects is possible with smaller agglomeration of interstitials at doses larger than 1×10^{14}/cm^2 since the critical nucleus size of these defects is smaller than that of the loops.

For example, fig.6.14 shows a typical case of free energy of nucleation calculations for a dose greater than 1×10^{14}/cm^2. It is evident in this plot that the nucleation barriers are not significantly different although the critical nucleus size for the {311} defect is 6 atoms large whereas for the loop it is 10 atoms large. As the interstitial agglomerates form, early in the agglomeration, it becomes easier for the interstitials to nucleate the {311} defect since the {311} defect has a smaller critical nucleus size as compared to the loop. This would explain the experimental evidence that at higher doses

{311}s nucleate first and then these defects unfault to form loops. Also, experimentally, the critical dose for {311} nucleation is $7 \times 10^{12}/cm^2$ and loops become more stable than {311}s at a dose around $2 \times 10^{14}/cm^2$ [Jones 96]. Therefore, we find that the theoretical calculations carried out in this work yield trends which conform to experimental evidence. Figs. 6.10-6.16 support this conclusion.

According to Li *et al.* [Li 98], the {311}s are the source of the loops and this experiment was done at sub-amorphizing implant doses. Fig. 6.9 is a plot of the formation energy per interstitial as a function of defect size for {311} defects and perfect loops. From this plot it is evident that for both {311}s and loops the formation energy per interstitial decreases continuously with defect size. This implies that there is a driving force for increase in defect size. The implications of the trends in defect nucleation can be validated with an inspection of the experimental data obtained by Robertson *et al.* [Robertson 2000] for amorphizing implants.

Fig. 6.17 is a plot of percentage loop nucleated as a function of anneal time for the experiment [Robertson 2000] described in the first part of this chapter. In that work, it was noticed that 45% of the loops were nucleated in the first 10 minutes of anneal. Out of these, the nucleation of 25% of the loops could not be explained as having occurred due to unfaulting of {311} defects. This number of unexplained loops was determined by the fact that they did not nucleate at the original location of {311}s. By overlapping of sequential TEM micrographs before and after unfaulting, it was found that 75% of the nucleated loops were located at the same spots as that of the original {311}s and the remaining 25% could not be found to originate at {311} sites.

The free energy calculations carried out in this chapter show that the {311} defects nucleate first during an anneal. The unfaulting reaction to convert {311} defects into perfect dislocation loops is given as follows [Li 98]:

$$\frac{a}{21}[116] + \frac{a}{42}[19\ \bar{2}\ 9] = \frac{a}{2}[101]$$ (6.8)

As an example, consider a {311} defect of length 1100Å and width 45Å as observed experimentally by Jinghong *et al.* [Li 2000]. The total number of atoms contained in this defect is estimated to be 1710 using the {311} interstitial configuration model developed by Kim *et al.* [Kim 97] which is described in section 6.2.2. The total energy of this {311} defect is calculated by estimating Gb^2 x total length of the {311} + (length)x(width)x(γ) where G is the shear modulus of silicon (6.45×10^{10} Pa), b is the Burgers vector of the {311} defect (a/21[116]) and γ is the stacking fault energy of silicon (60 mJ/m^2). This total energy is estimated from the calculation to be 2532 eV. Correspondingly, the radius (R) of the final loop is estimated to be 60Å using the silicon atom density on the {111} plane (1.5×10^{15}/cm^2) with the total number of atoms in the loop being 1710 using the expression πR^2x(atom density) = Total number of atoms . The total energy of the loop is calculated to be $2\pi R G b_l^2$ where b_l is the Burgers vector of the loop (a/2[101]). This total energy value for the loop is calculated to be 2241 eV. The energy barrier for the unfaulting reaction is estimated by computing the energetics of the transform partial which sweeps through the stacking fault during the unfaulting reaction. This has a value of Gb_p^2 x(length) = 3300eV, where b_p is the Burgers vector of the transform a/42[19 $\bar{2}$ 9] . The {311} defect unfaults into a loop upon annealing the silicon sample at high temperatures such as 750 ^{0}C which enables the {311} defect to surmount the energy barrier of unfaulting. The 25% of unexplained loops in the work of Robertson *et al.*

[Robertson 2000] could originate in submicroscopic interstitial defects which are primitive {311} defects and this is supported by nucleation theory results explained above.

6.4 Summary

It was observed that, for cluster size less than 10 interstitials, formation energy per interstitial values were lower than that of {311} defects in the same size regime implying that small interstitial clusters are not direct precursors of {311} defects. It is inferred that the small clusters have to undergo a structural transformation before nucleating {311} defects. Atomistic simulations have been done using the conjugate gradient method with the Stillinger-Weber potential to obtain the formation energy of {311} defects for defect widths up to 5 chains.

It is observed that the width of the most stable defect increases initially at first with defect size and then saturates. This trend is in agreement with experiment. The formation energy of perfect loops was also obtained by conjugate gradient simulations. From free energy calculations it is found that {311} defects nucleate earlier in the annealing phase and unfault into loops as the anneal proceeds. This explains the nucleation of loops in the end of range region for amorphized and annealed samples.

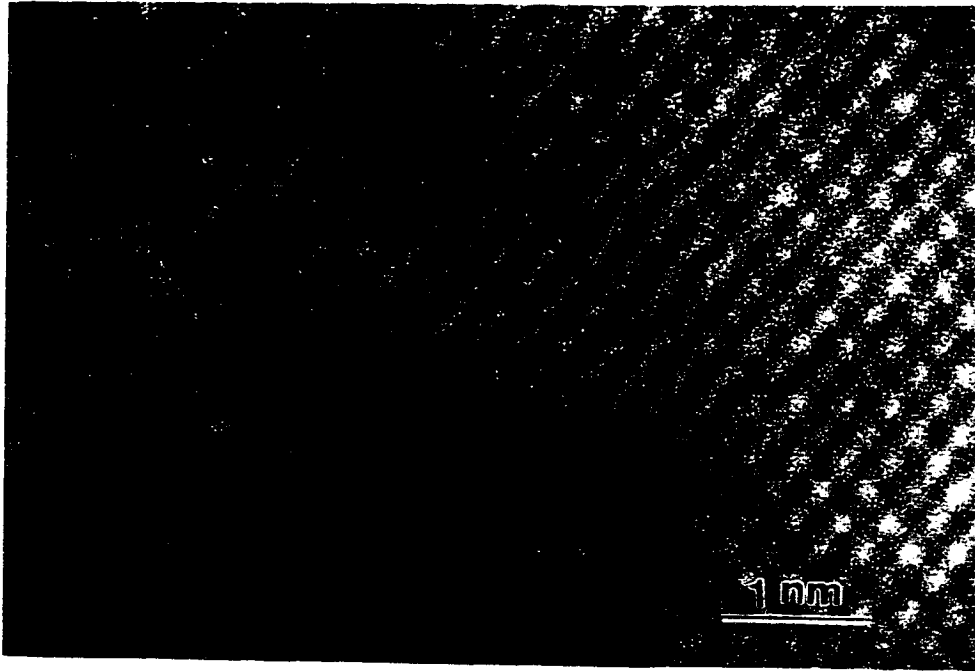Fig. 6.1 Plan view weak beam dark field image of {311} defects.
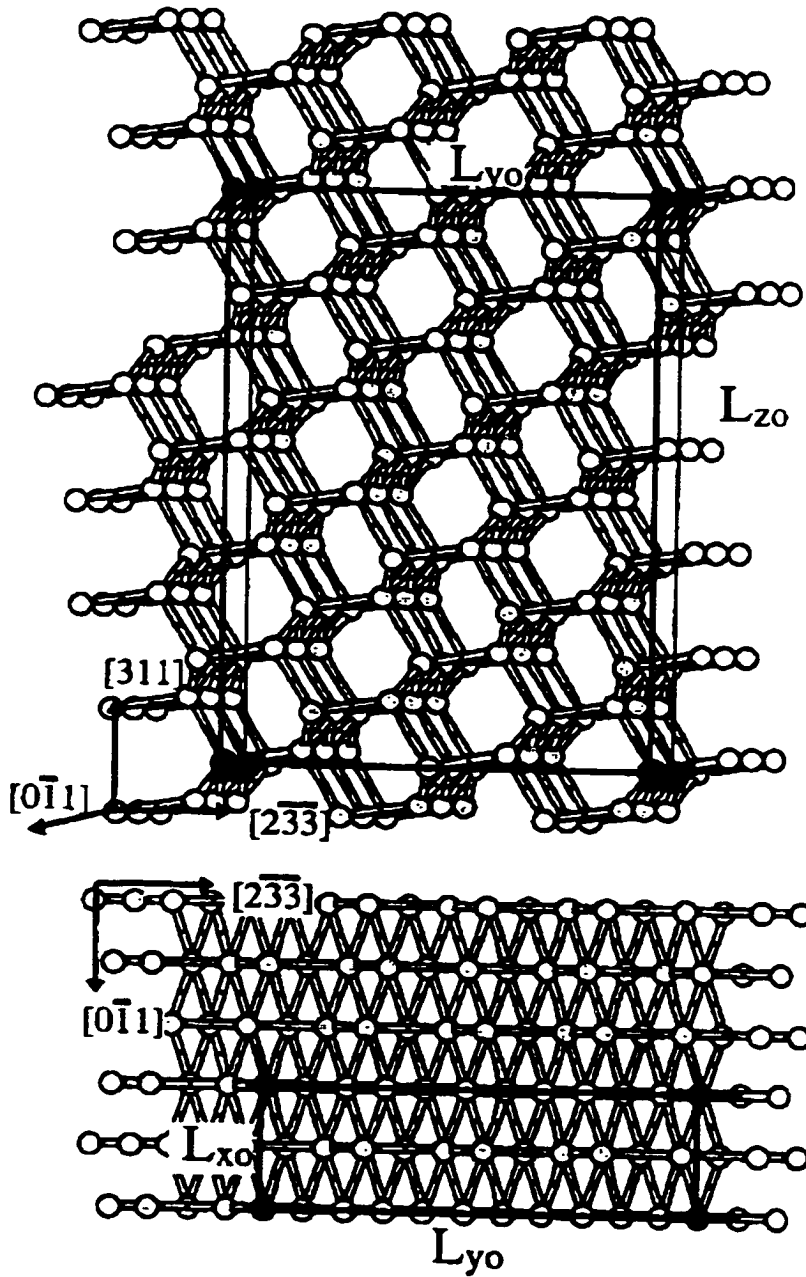
Fig. 6.2 Cross-section HRTEM image of {311} defect.

Fig. 6.3 Configuration of {311} defects. The dimensions of the unit cell are $L_{x0} = a/\sqrt{2}$, $L_{y0} = a\sqrt{11}/(2\sqrt{2})$ and $L_{z0} = a\sqrt{11}$, where a is the Si lattice constant. The size of the computational cell is $L_x = n_x \times L_{x0}$, $L_y = n_y \times L_{y0}$ and $L_z = 2 \times L_{z0}$.
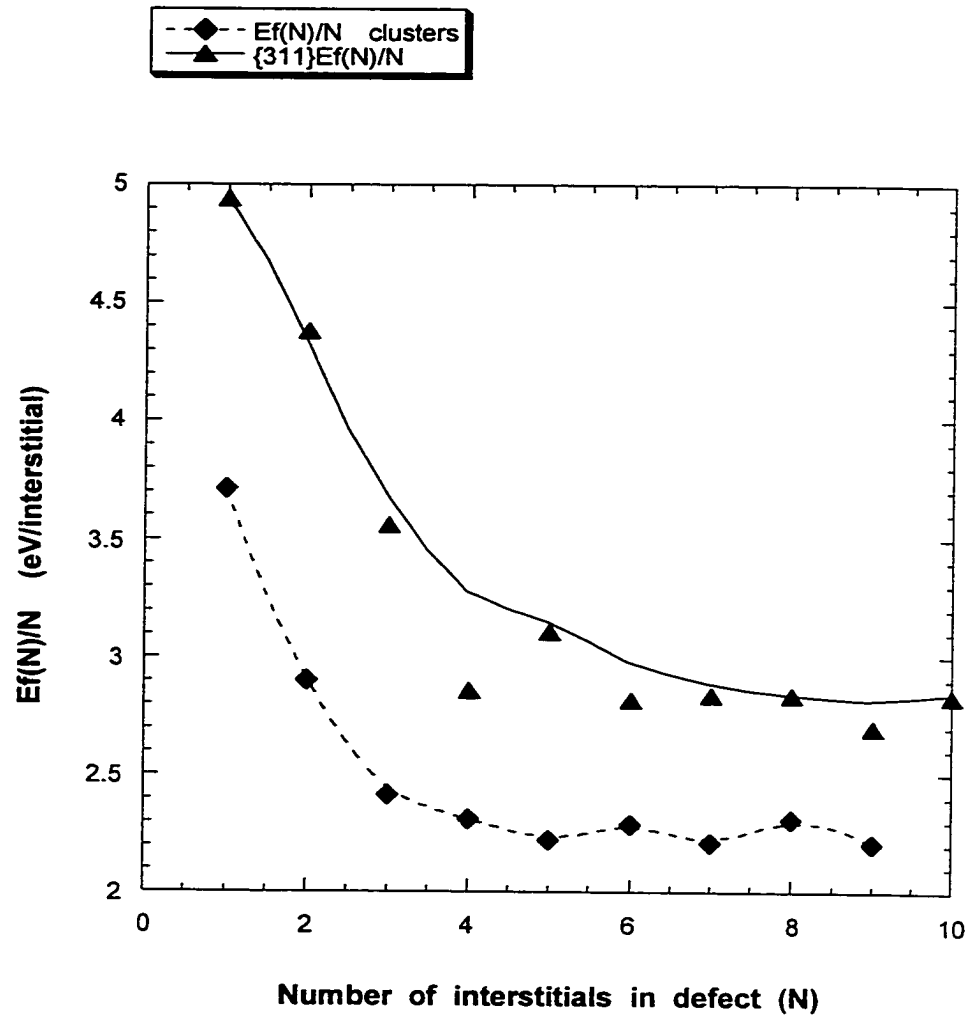
Fig. 6.4 Plots of formation energy per interstitial (Ef(N)/N) as a function of defect size(N) for small clusters and {311} defects of corresponding size.
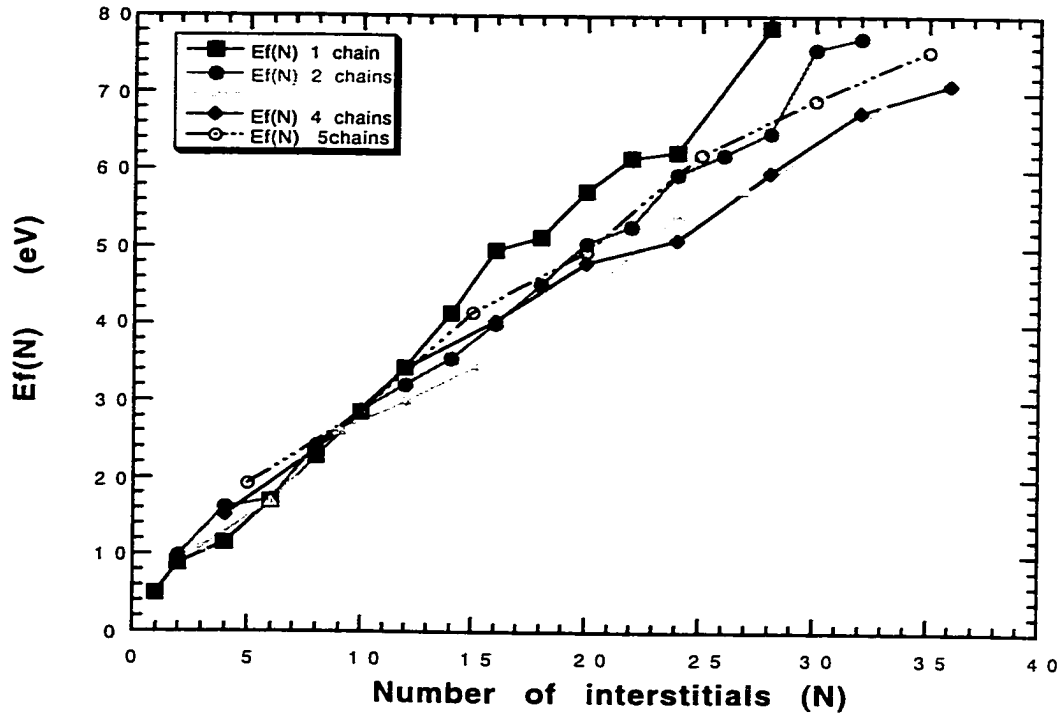
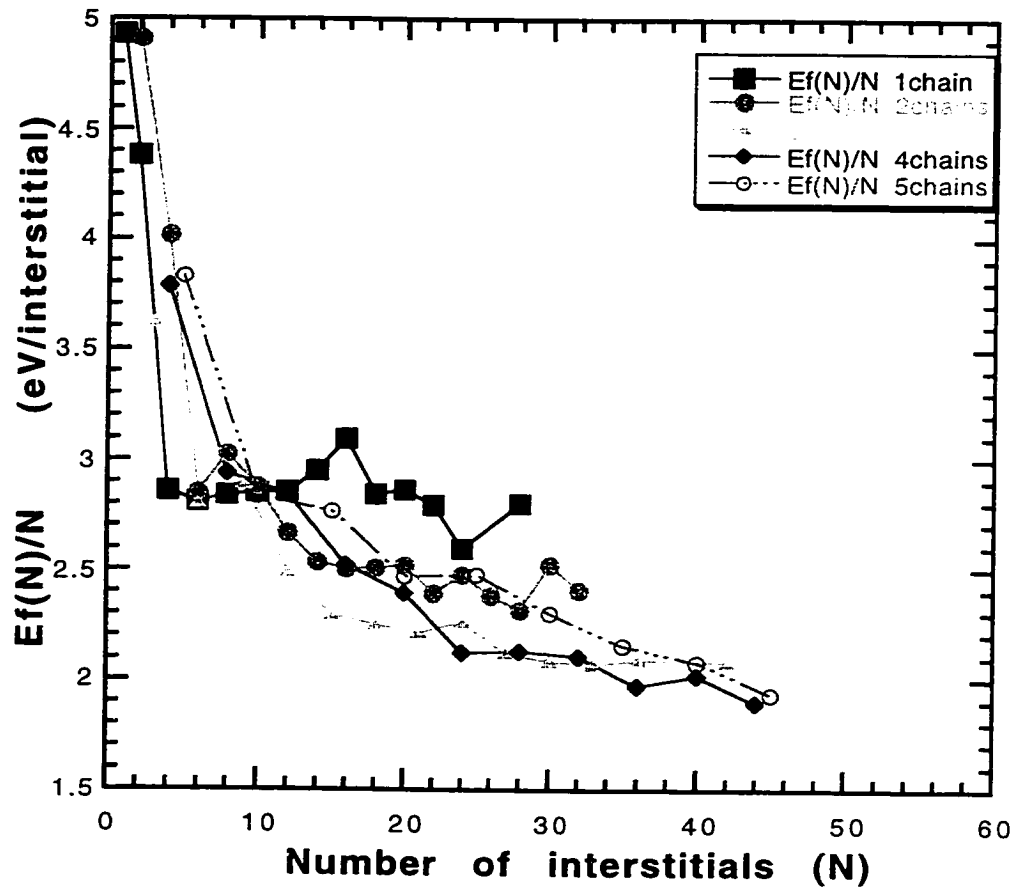Fig. 6.5 Total formation energy (Ef(N)) of {311} defect as a function of defect size for different widths

Fig. 6.6 Formation energy per interstitial (Ef(N)/N) for {311} defect as a function of defect size for different widths.

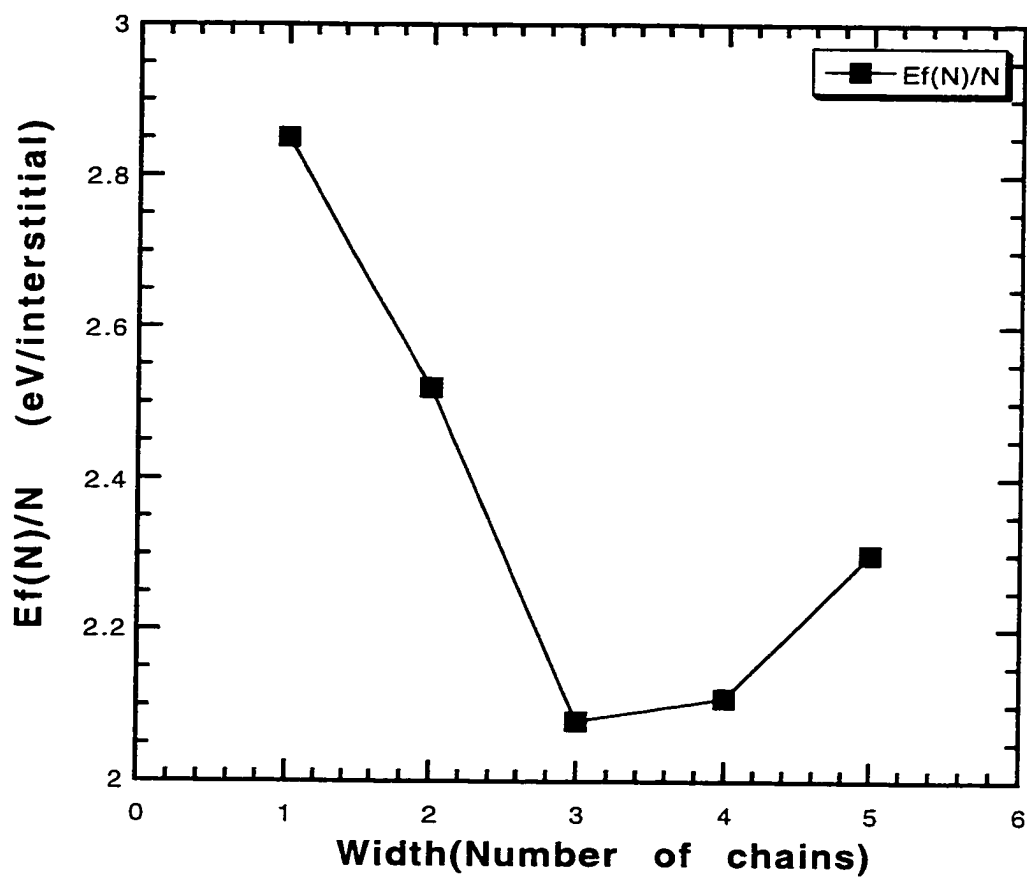Fig. 6.7 Formation energy per interstitial (Ef(N)/N) as a function of width (number of chains) for a defect size of 30 interstitials.
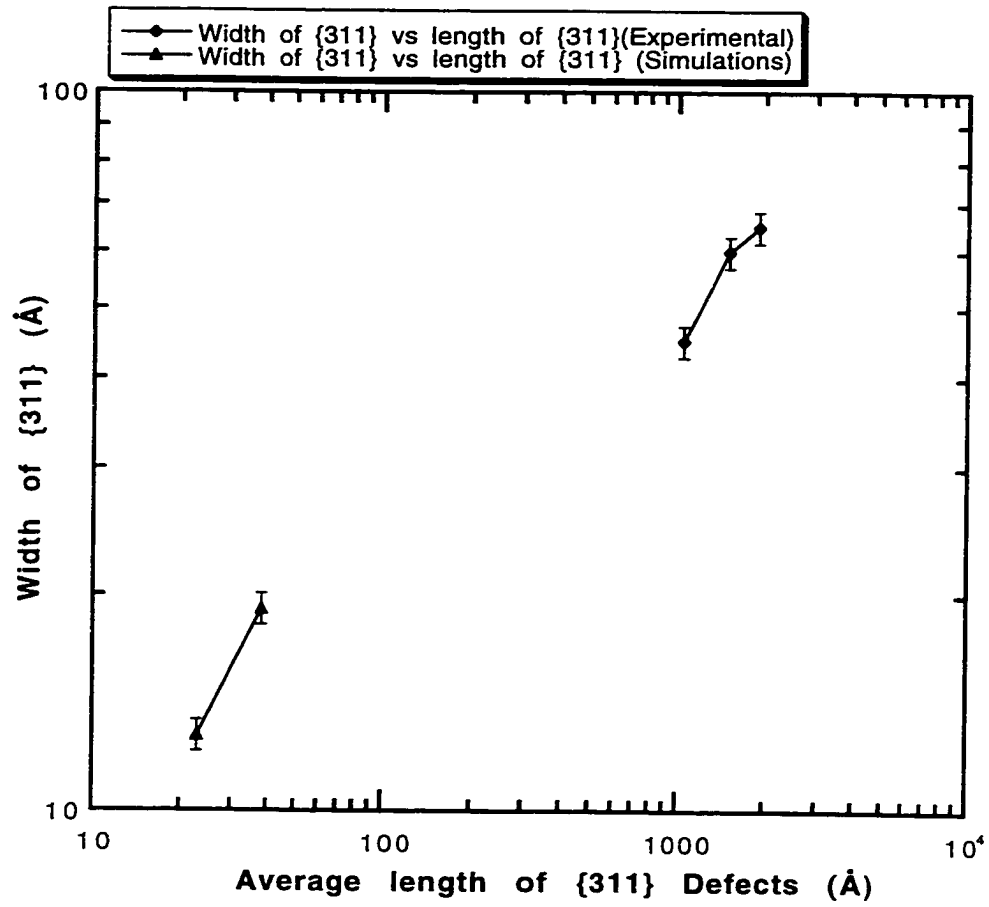
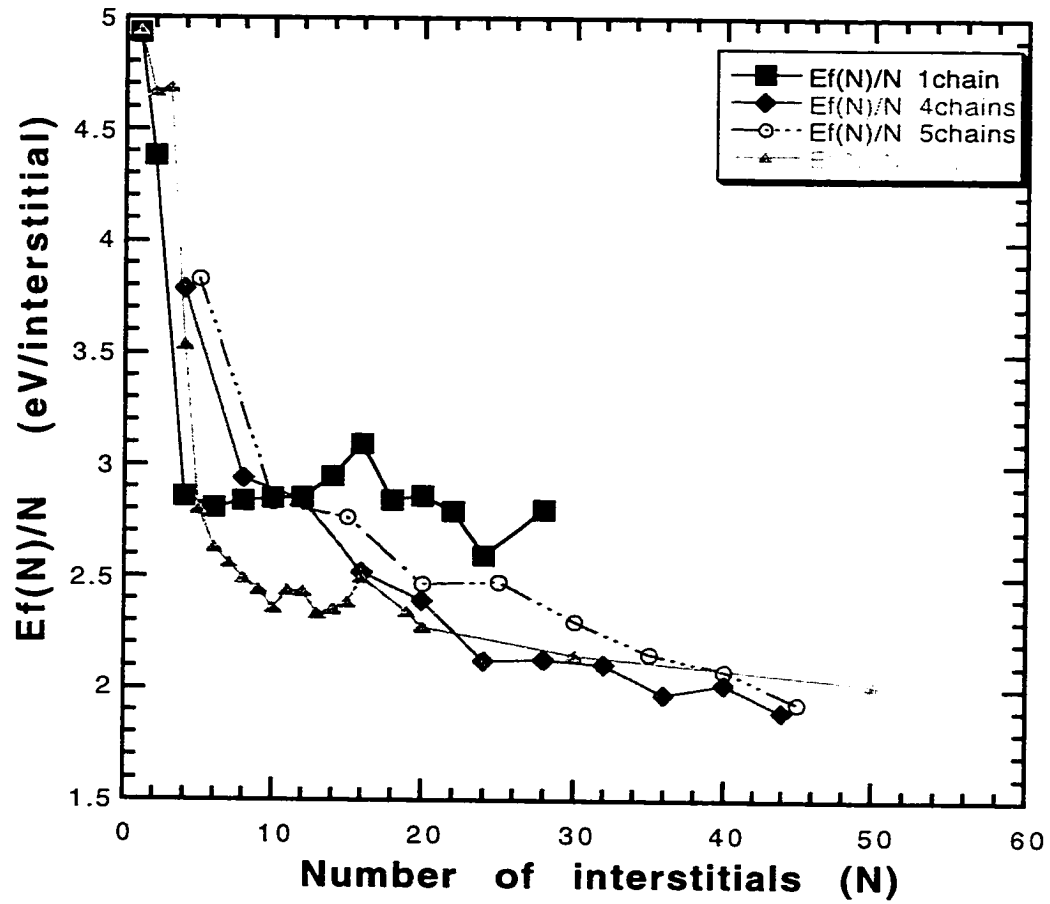Fig. 6.8 Width as a function of average length of {311} defects

Fig. 6.9 Formation energy per interstitial (Ef(N)/N) for {311}s (for different widths) and perfect dislocation loop
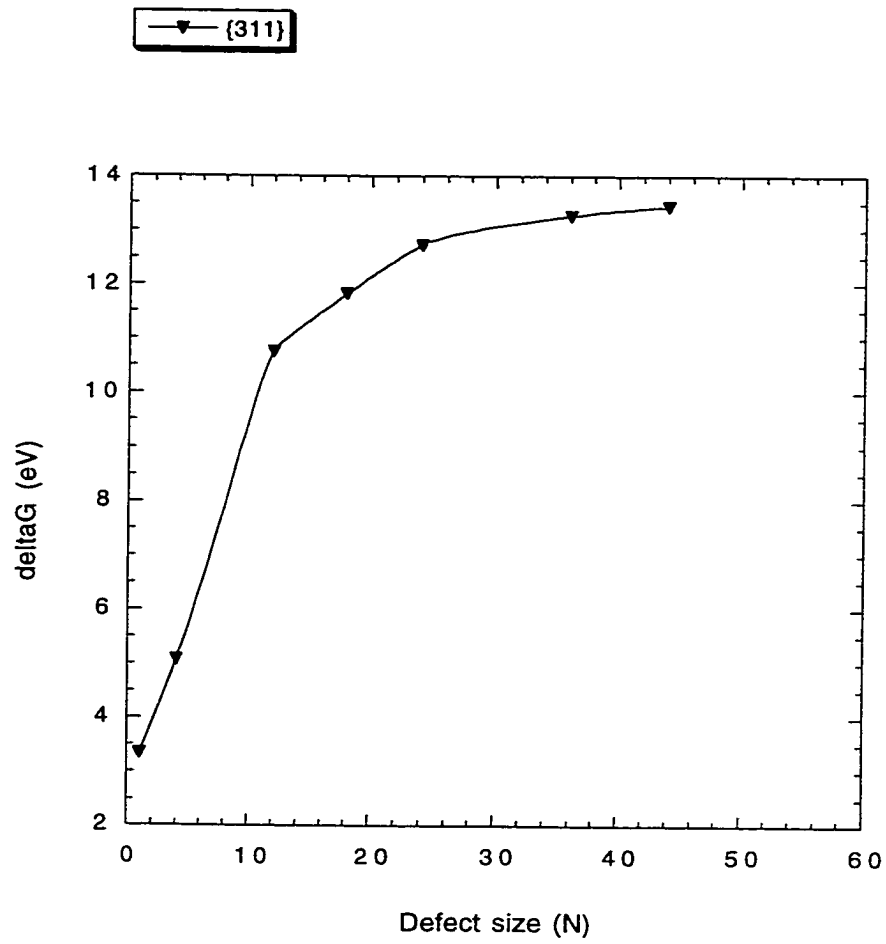
Fig. 6.10 Free energy of nucleation as a function of defect size for the {311} defect at a dose of $8 \times 10^{11}/\text{cm}^2$
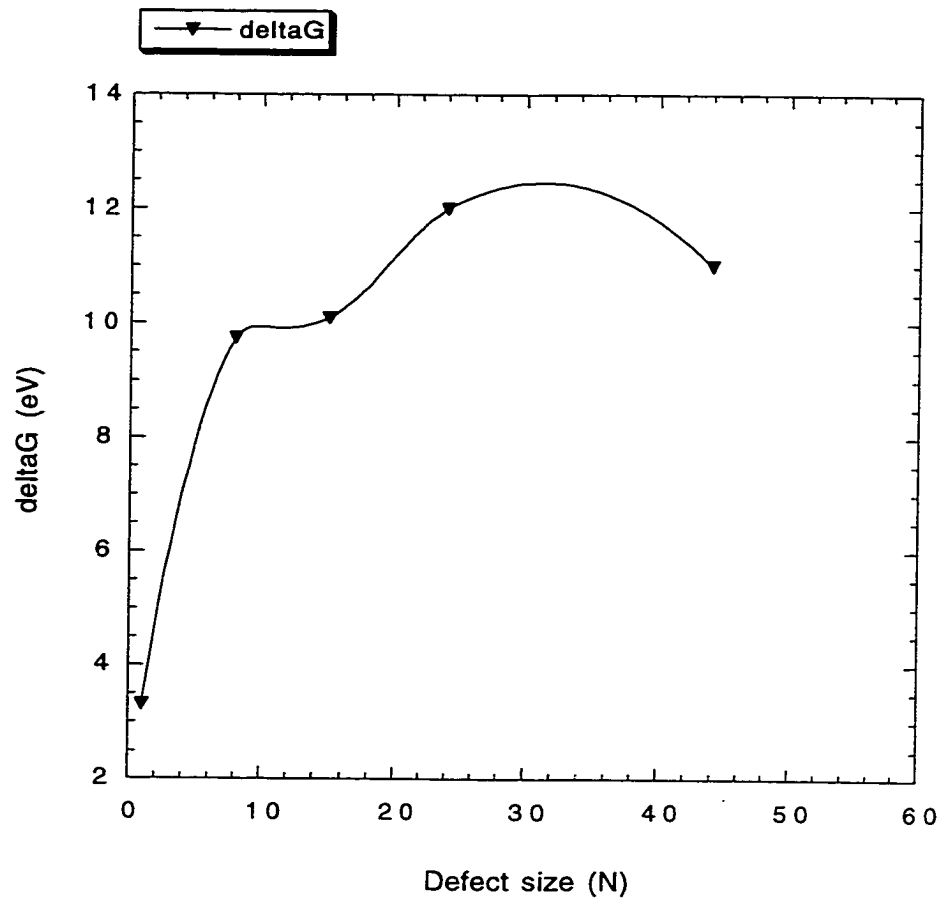
Fig. 6.11 Free energy of nucleation as a function of defect size for the {311} defect at a dose of $1.2 \times 10^{12}/\text{cm}^2$

Fig. 6.12 Free energy of nucleation as a function of defect size for the {311} defect and loop at a dose of $4.7\times10^{12}/cm^2$

Fig. 6.13 Free energy of nucleation as a function of defect size for the {311} defect and loop at a dose of $1.2 \times 10^{13}/cm^2$
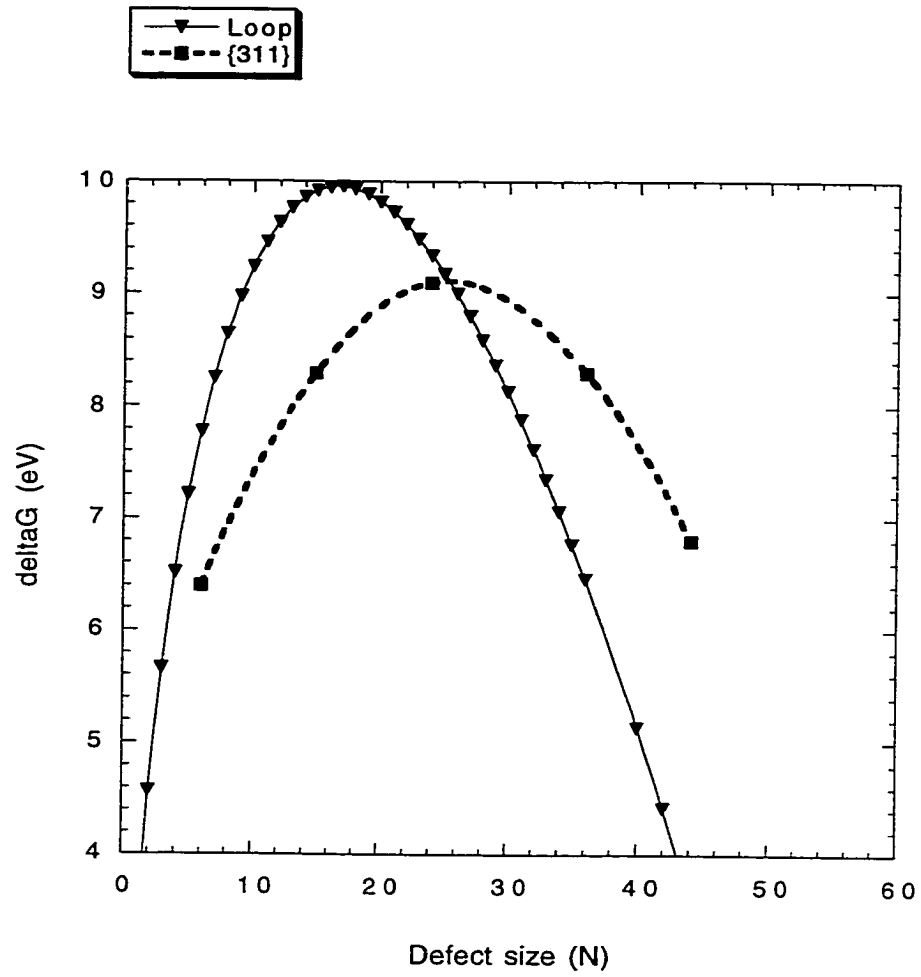
Fig. 6.14 Free energy of nucleation as a function of defect size for the {311} defect and loop at a dose of $1.2 \times 10^{14}/cm^2$
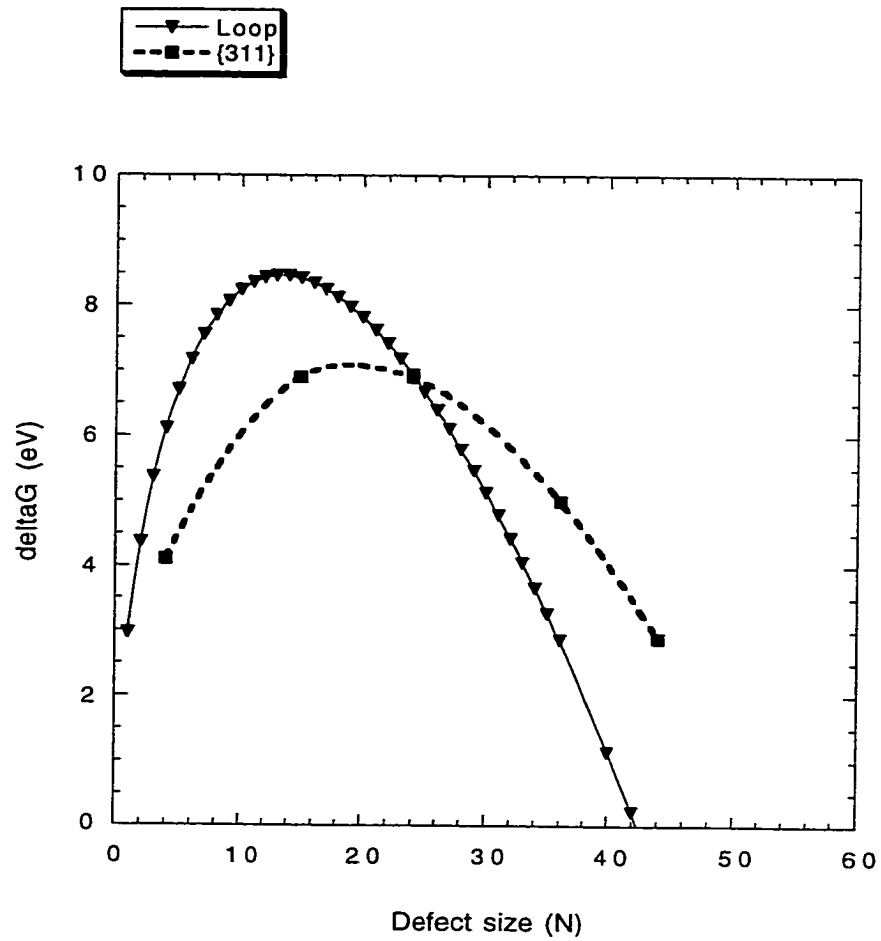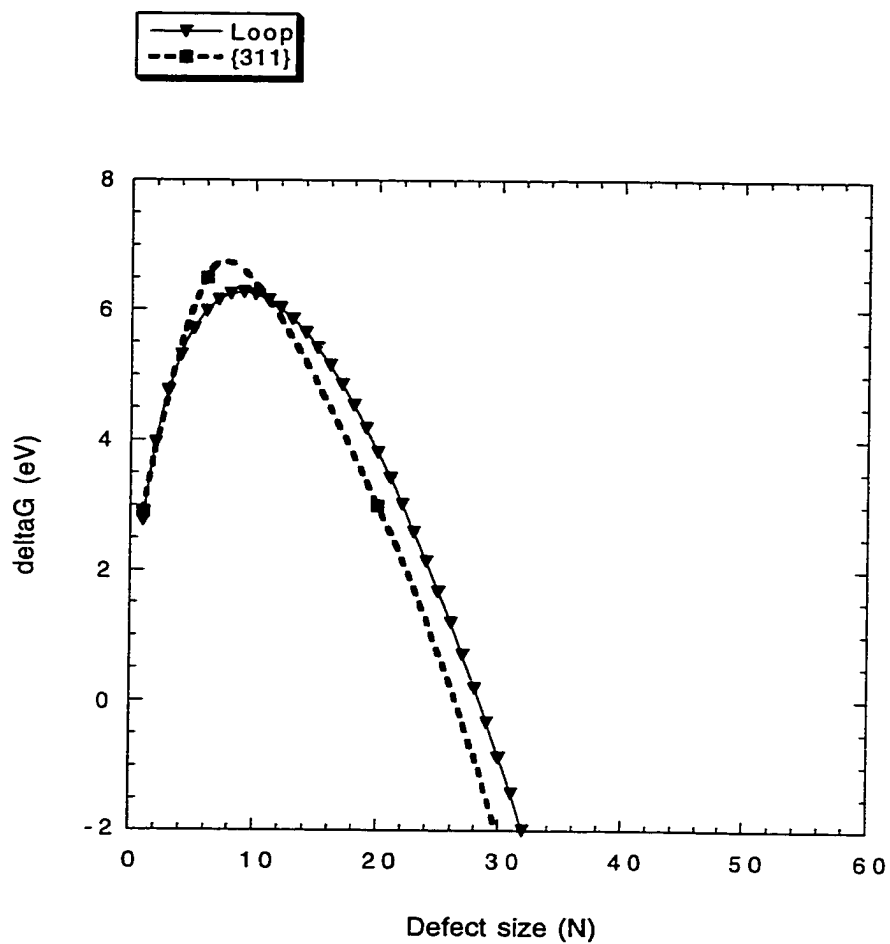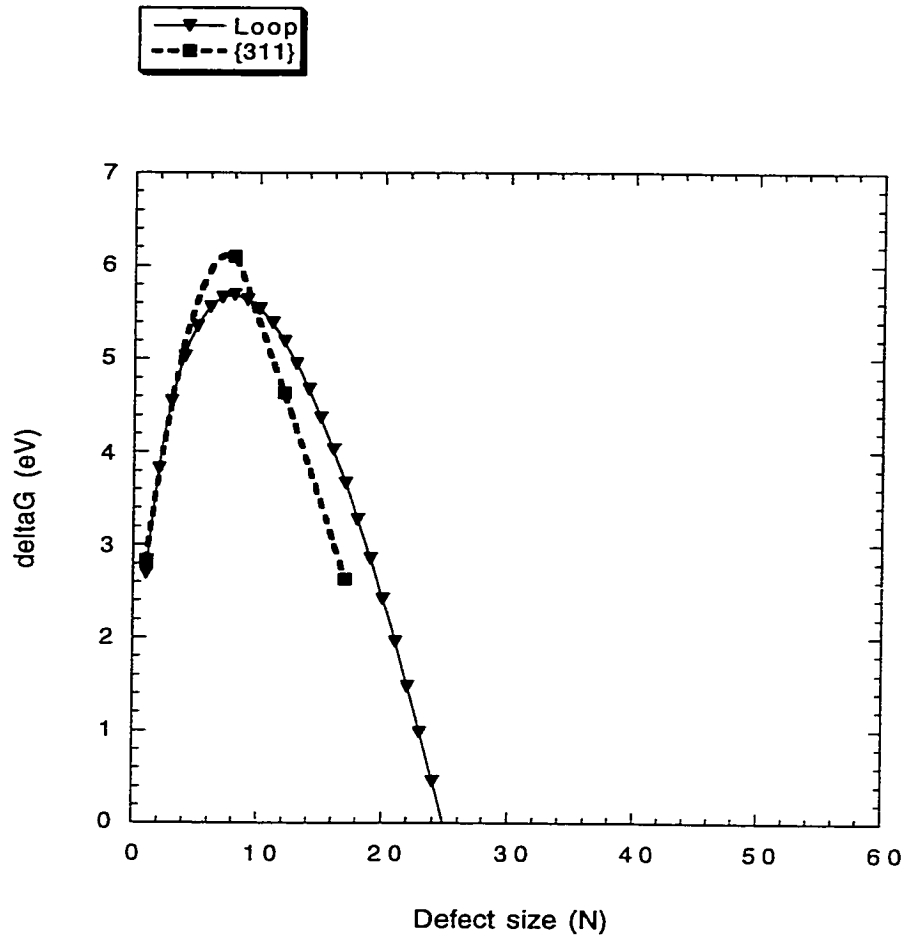
Fig. 6.15 Free energy of nucleation as a function of defect size for the {311} defect and loop at a dose of $2.4 \times 10^{14}/cm^2$
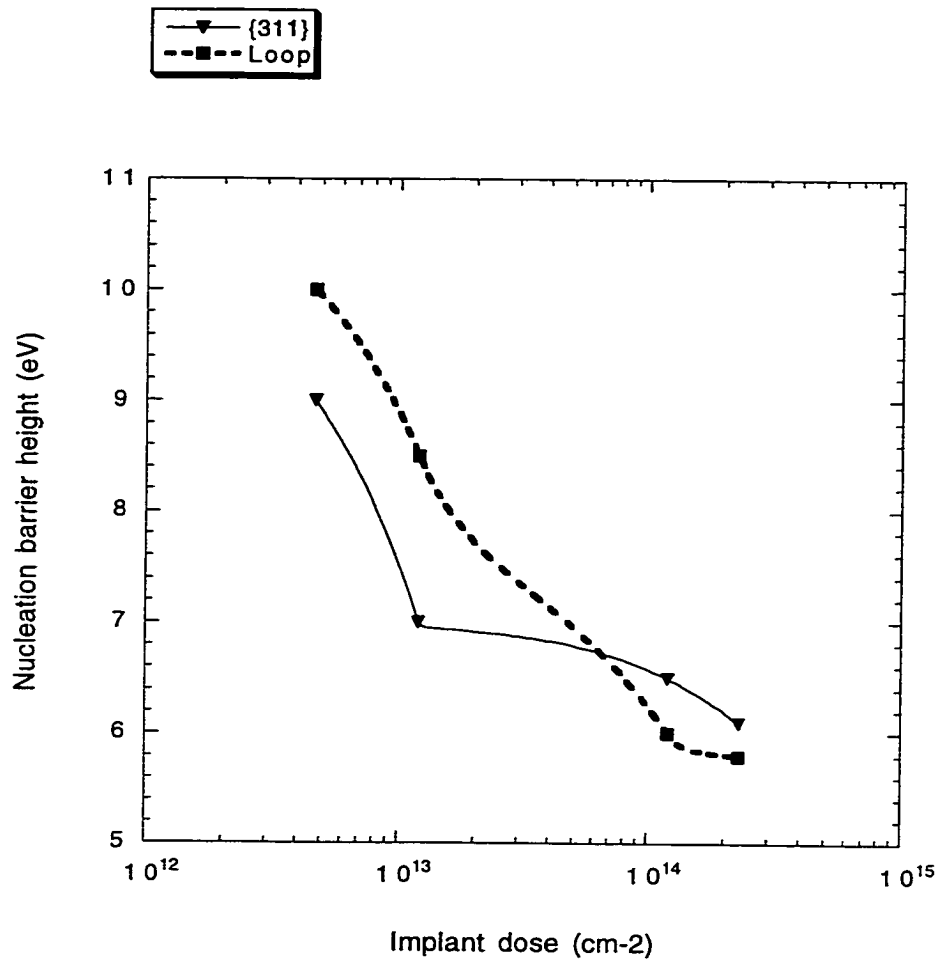
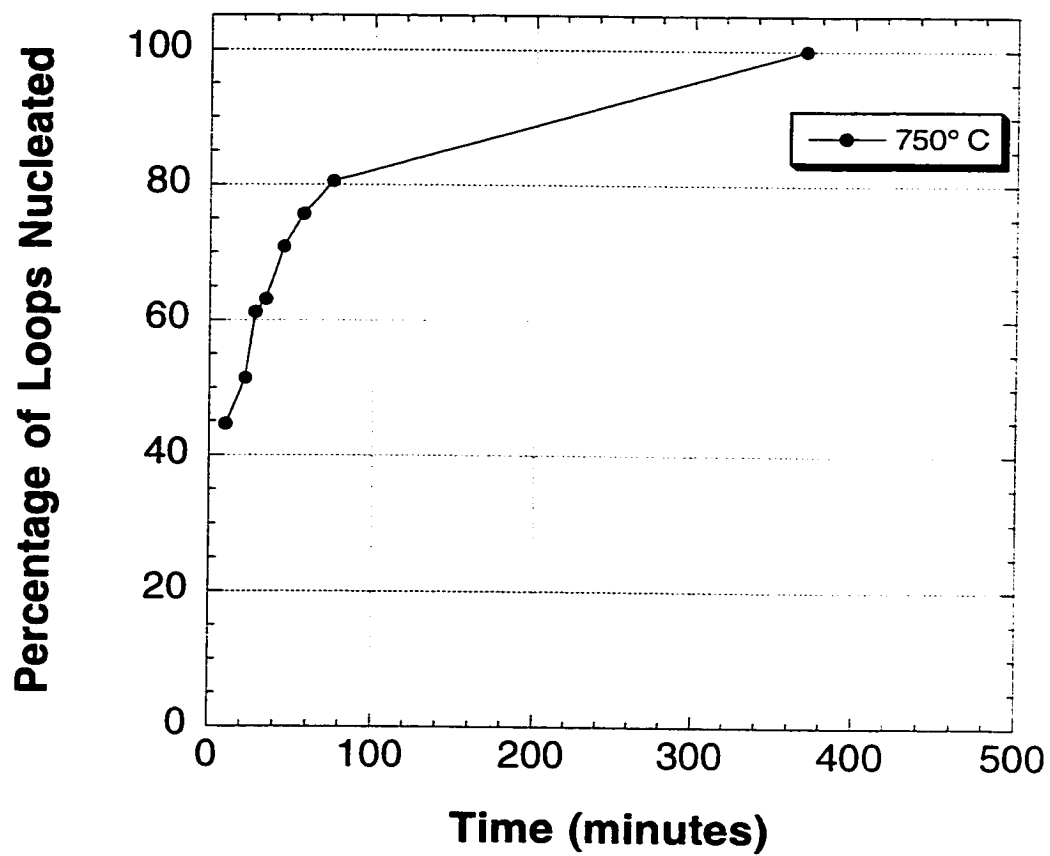Fig. 6.16 Nucleation barrier height as a function of implant dose for the {311} defect and loop

Fig. 6.17 Percentage loops nucleated as a function of annealing time

CHAPTER 7
CONCLUSIONS

Ion implantation will continue to be the most widely used technique of introducing dopants into silicon substrates in integrated circuit manufacturing. Ion implantation produces damage and upon post-implantation annealing the excess interstitials agglomerate to form submicroscopic clusters and extended defects. It is now well established that point defects, submicroscopic clusters and extended defects play an important role in dopant diffusion. This is particularly important while studying the phenomenon of transient enhanced diffusion which is a limiting factor in the formation of shallow junctions.

Since point defects have to diffuse in the lattice before agglomerating to form clusters, it is important to analyze the point defect diffusivities and self diffusion. While experimental methods cannot yield information about diffusivities of individual point defects such as interstitials, vacancies and also the di-vacancy, theoretical calculations have been found to be very useful in this task. Particularly, molecular dynamics simulations can be used to calculate the point defect diffusivities since it is possible using this technique to compute mean squared displacements over all atoms in the presence of defects. The interatomic potential used in molecular dynamics is crucial as far as the validity of the results are concerned. Among the over 30 interatomic potentials for silicon available in the literature, the Stillinger-Weber potential is by far the most widely used interatomic potential.

105

Recently, a new interatomic potential called the environment-dependent interatomic potential (EDIP) was developed, whose authors claimed that it was superior to the conventional potentials. In chapter four of this dissertation a comparative study of diffusivities of point defects and the di-interstitial was done using the Stillinger-Weber, Tersoff and EDIP potentials. From the migration energies thus obtained it was found that the EDIP potential lacks validity as it yields a very low value for migration energy of the interstitial (0.334 eV) as compared to the value given by the other two potentials as well as results from LDA available in the literature (0.9-1.0 eV). Moreover, using formation and migration energies the self-diffusion coefficient was calculated for the interstitial and vacancy. It was found that the crossover temperature for interstitials and vacancy self-diffusion coefficients was 717 ^{0}C whereas the experimental value is 1050 ^{0}C which further proves that the EDIP potential is flawed.

In chapter 5 of this dissertation, the results were presented of molecular dynamics simulations with the Stillinger-Weber potential used to estimate the formation energy of small interstitial (<10 interstitials) clusters. It was found that the formation energy per interstitial decreases with increasing cluster size initially thereby indicating a driving force for the aggregation of interstitials into clusters. It was also found from atomic models that the clusters have a strain field in their vicinity. Moreover, in chapter 6, a comparison between the formation energy per interstitial of the submicroscopic clusters and {311} defects in the same size range indicates that the clusters are more stable than the {311} defects. This implies that small interstitial clusters are not direct precursors of {311} defects and that the small clusters have to undergo a structural transformation before nucleating {311} defects.

In chapter 6, a study is presented of Conjugate Gradient calculations with the Stillinger-Weber potential to obtain formation energies of {311} defects for defect widths up to five chains. It was observed that the {311} width increases as the defect size increases initially and then saturates. This is in agreement with experimental observations. This contradicts some of the studies in the literature where linear growth takes precedence over increase in width. The formation energy of perfect dislocation loops was also calculated as a function of defect size. From the formation energies the free energy of nucleation was calculated for {311} defects and loops for various implant doses. This provides an explanation for loop nucleation through unfaulting of {311} defects which form earlier in an anneal.

LIST OF REFERENCES

[Allen 87]   Allen M. P. and D. J. Tildesley, *Computer simulation of liquids*, Oxford Science Publications, Oxford (1987).

[Batra 87]   Batra I. P, F .F .Abraham and S .Ciraci, Phys. Rev. B **35**, 9552 (1987).

[Bazant 97]   Bazant Martin Z., E. Kaxiras and J. F. Justo, Phys. Rev. B **56**, 8542 (1997).

[Beeler 76]   Beeler J. R and M. F. Beeler, In *Fundamental aspects of radiation damage in metals* M.T. Robinson, R.W. Young (eds) CONF-751006-P1, National Technical Information Service, Springfield, Virginia, pp. 28-34 (1976).

[Benton 97]   Benton J. L., S. Libertino, P. Kringoi, D. J. Eaglesham, J. M. Poate, and S. Coffa, J. Appl. Phys. **82**, 120 (1997).

[Berendsen 85]   Berendsen H. J. C. and W. F. Van Gunsteren, In *Molecular dynamics simulation of statistical mechanical systems*. Proceedings of the Enrico Fermi Summer School, Varenna, pp. 43-65, Soc. Italiana di Fisica, Bologna (1985).

[Biersack 80]   Biersack J. P, L. Haggmark, Nucl. Instrum. And Methods **174**, 257 (1980).

[Blochl 93]   Blochl P. E, E. Smargiassi, R. Car, D. B. Laks, W. Andreoni, and S. T. Pantelides, Phys. Rev. Lett. **70**, 2435 (1993).

[Bohr 13]   Bohr N., Phil. Mag. **25**, 10 (1913).

[Bohr 15]   Bohr N., Phil. Mag. **30**, 581 (1915).

[Bohr 48]   Bohr N., K. Dan, Vidensk. Selsk. Mat. Fys. Medd **18**(8) (1948).

[Bongiorno 99]   Bongiorno A., L. Colombo, F. Cargnoni, C. Gatti, and M. Rosati, In *Proceedings of the 24th International Conference*

on the Physics of Semiconductors, D. Gershoni (ed), World Scientific, Singapore, (1999).

[Born 12]   Born M. and Th. Vor Karman, Physik A, **13**, 297, (1912).

[Broughton 87]   Broughton J. Q. and X. P. Li, Phys. Rev. B **35**, 9120 (1987).

[Car 84]   Car R., P. J. Kelly, A. Oshiyama and S. T. Pantelides, Phys. Rev. Lett. **54**, 360 (1984).

[Chadderton 71]   Chadderton L. T. and F. H. Eisen, Radiat. Effects, **7**, 129 (1971).

[Coffa 2000]   Coffa Salvatore, Sebania Libertino, and Corrado Spinella, Appl. Phys. Lett. **76**, 321 (2000).

[Colombo 99]   Colombo L., A. Bongiorno and M. Rosati, Mat. Res. Soc. Symposium Proceedings **538**, 413 (1999).

[Cuendet 96]   Cuendet Nicolas, Timur Halicioglu and William A. Tiller, Appl. Phys. Lett. **68**, 19 (1996).

[Davidson 70]   Davidson S. M. and G. R. Booker Radiat. Effects, **6**, 33 (1970).

[Daw 84]   Daw M. S., M. I. Baskes, Phys. Rev. B **29** 6443 (1984).

[Diaz de la Rubia 92]   Diaz de la Rubia T. and M. W. Guinan, Solid State Phen. **27**, 1-50 (1992).

[Downey 99]   Downey Daniel F. and Kevin S. Jones, Proceedings of international conference on Ion Implantation Technology, IEEE , Piscataway, NJ, **2**, 897 (1999).

[Eaglesham 94]   Eaglesham J., P. A. Stolk, H. J. Gossmann, and J. M. Poate, Appl. Phys. Lett. **65**, 2305 (1994).

[Fahey 85]   Fahey P. M., Ph.D Dissertation, Stanford University, 1985.

[Fahey 89]   Fahey P. M., P. B. Griffin, and J. D. Plummer, Reviews of Modern Physics **61** (2) 1989.

[Fair 81]   Fair R. B., In *Impurity doping*, F. Wang (ed) (North-Holland, Amsterdam, 1981).

[Ferreira 76]	Ferreira C. A Lima, and A. Howie, Phil. Mag. **36**, 1057 (1976).
[Finnis 89]	Finnis M. W., MOLDY6. A Molecular Dynamics Program for simulation of Pure Metals, Harwell Report AERE-R-13182, Oxfs (1989).
[Gencer 97]	Gencer Alp H. and Scott T. Dunham, J. Appl. Phys. **81**, 631 (1997).
[Gibson 60]	Gibson J. B., A.N. Goland, M. Milgram and G.H. Vineyard, Phys. Rev. **120**, 1229 (1960).
[Gilmer 95]	Gilmer G. H., T. Diaz de la Rubia, D. M. Stock, and M. Jaraiz, Nucl. Instrum. Methods Phys. Res. B **102**, 247 (1995).
[Gosele 96]	Gosele U., A. Plossl and T. Y. Tan, In *Process Physics and Modeling in semiconductor Technology*, G. R. Srinivasan, C. S. Murthy and S. T. Dunham (eds), Electrochemical Society, Pennington, NJ, p.309 (1996).
[Gossmann 93]	Gossmann H. J., A. M. Vrendenberg, C. S. Rafferty, H. S. Luftman, F. C. Unterwald, D. C. Jacobson, T. Boone, and J. M. Poate, J. Appl. Phys. B **74**, 3150 (1993).
[Heermann 86]	Heermann D. W., *Computer simulation methods in theoretical physics*, Springer-Verlag, Berlin (1986).
[Hobler 99]	Hobler G. and C. S. Rafferty, Mat. Res. Soc. Symp. Proc. **568**, 123 (1999).
[Ishimaru 96]	Ishimaru M., K. Yoshida and T. Motooka, Phys. Rev B **53**, 7176 (1996).
[Jaraiz 96]	Jaraiz M., G. H. Gilmer, and J. M. Poate, Appl. Phys. Lett. **68**, 409 (1996).
[Jones 87]	Jones K. S., Ph.D. Dissertation, University of California, 1987.
[Jones 96]	Jones K. S. and J. Gyulai, In *Ion Implantation Science and Technology*, James Ziegler (ed), Ion Implantation Technology Co., Yorktown, NY, p. 261 (1996).

[Justo 98]   Justo J. F., M. Z. Bazant, E. Kaxiras, V. V. Bulatov and
                  S.Yip, Phys. Rev. B **58**, 2539, (1998).

[Kelires 88]   Kelires P. C. and J. Tersoff, Phys. Rev. Lett. **61**, 562
                  (1988).

[Kim 97]   Kim Jeongnim, John W. Wilkins, Furrukh S. Khan, and
                  Andrew Canning , Phys. Rev. B **55**, 16186 (1997).

[Kim 2000]   Kim Jeongnim, Florian Kirchhoff, John. W. Wilkins and
                  Furrukh S. Khan, Phys. Rev. Lett. **84**, 503 (2000)

[Kluge 87]   Kluge M. D., J. R. Ray and A. Rahman, Phys. Rev. B **36**,
                  4234 (1987).

[Kohyama 92]   Kohyama Masanori and Seiji Takeda, Phys. Rev. B **46**,
                  12305 (1992).

[Li 88]   Li X. P., G. Chen, P. B. Allen, and J. Q. Broughton, Phys.
                  Rev. B **38**, 3331 (1988).

[Li 98]   Li Jinghong and Kevin S. Jones, Appl. Phys. Lett. **73**, 3748
                  (1998).

[Li 2000]   Li Jinghong, Gopalakrishnan Subramanian, Craig Jasper,
                  Mark E. Law and Kevin S. Jones, Poster presentation,
                  Materials Research Society Spring 2000 Meeting, San
                  Francisco, CA, Unpublished.

[Lindhard 61]   Lindhard J. and M. Sharff, Phys. Rev. **124**, 128 (1961).

[Lindhard 63]   Lindhard S., M. Scharff and H. E. Schiott, Kgl. Danske
                  Vid. Selsk. Matt-Fys. Medd **33**, 14 (1963).

[Luedke 88]   Luedke W. D. and U. Landman, Phys. Rev. B **37**, 4656
                  (1988).

[Mathews 73]   Mathews M. D. and S. J. Ashby, Phil. Mag. A **27**, 1313
                  (1973).

[Michel 87]   Michel A. E., W. Rausch, P. A. Ronsheim, and R. H. Kastl,
                  Appl. Phys. Lett. **50** 460 (1987).

[Mistriotis 89]   Mistriotis A. D., N. Flytzanis and S. C. Farantos, Phys.
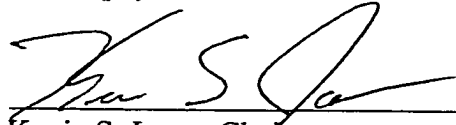   Rev. B **39**, 1212 (1989).

[Najafabadi 89]   Najafabadi R., R. LeSar, and D. J. Srolovitz, Phys. Rev. Lett. **63**, 624 (1989).

[Nichols 89]   Nichols C. S., C. G. Van de Walle, and S. T. Pantelides, Phys. Rev. B **40**, 5484 (1989).

[Pearson 84]   Pearson E. M., T. Takai, T. Halicioglu and W. A. Tiller, J. Cryst. Growth, **70**, 33 (1984).

[Poon 90]   Poon W., S. Yip, P. S. Ho and F. F. Abraham, Phys. Rev. Lett, **65**, 2161 (1990).

[Robertson 2000]   Robertson L. S, K. S. Jones, L M. Rubin and J. Jackson, J.Appl.Phys. **87**(6), 2910 (2000).

[Robinson 74]   Robinson M. T. and I. M. Torrens, Phys. Rev. B9, 5008 (1974).

[Robinson 94]   Robinson M. T., J.Nucl. Mate. **216**, 1 (1994).

[Salisbury 79]   Salisbury I. G. and M. H. Loretto, Phil. Mag. A, **39**, 317 (1979).

[Schultz 91]   Schultz P. J., C. Jagadish, M. C. Ridgway, R. G. Elliman, J. S. Williams, Phys.Rev. B **44** 9118 (1991).

[Stillinger 85]   Stillinger F. H. and T. A. Weber, Phys. Rev. B **31**, 5262 (1985).

[Stolk 95a]   Stolk P. A., H. J. Gossmann, D. J. Eaglesham, and J. M. Poate, Appl. Phys. Lett. **66**, 568 (1995).

[Stolk 95b]   Stolk P. A., H. J. Gossmann, D. J. Eaglesham, and J. M. Poate, Nucl. Instrum. Methods Phys. Sect. B **96**, 187 (1995).

[Stolk 97]   P. A. Stolk, H. J. Gossmann, D. J. Eaglesham, D. C. Jacobson, C. S. Rafferty, G. H. Gilmer, M. Jaraiz, J. M. Poate, H. S. Luftman and T. E. Hayner, J. Appl. Phys. **81**, 6031 (1997).

[Tan 81]   Tan T. Y., Phil. Mag. **44**, 101 (1981).

[Tan 85]   Tan T. Y. and U. M. Gosele, Appl. Phys. A. **31** (1) (1985).

[Tan 97]   Tan T. Y., P. Plekhnov, and U. M. Gosele, Appl. Phys.
                   Lett. **70**, 1715 (1997).

[Tang 97]   Tang Meijie, L. Colombo, Jing Zhu and T. Diaz de la
                   Rubia, Phys. Rev. B **55**, 14279 (1997).

[Tasch 95]   Tasch Al, S. H. Yang, S. J. Morris, Nucl. Instrum. And
                   Methods **102**, 173 (1995).

[Tersoff 88]   Tersoff J., Phys. Rev. B **37**, 6991(1988).

[Tersoff 88]   Tersoff J., Phys. Rev. B **38**, 9902 (1988).

[Tersoff 89]   Tersoff J., Phys. Rev. B **39**, 5566 (1989).

[Thomson 03]   Thomson J. J., *Conduction of electricity through gases*,
                   Cambridge University Press, Cambridge (1903).

[Townsend 76]   Townsend P. D., J. C. Kelly, N. E. W. Hartlwy *Ion
                   implantation, sputtering and their applications* Academic
                   Press, New York (1976).

[Vineyard 72]   Vineyard G. H. In *Interatomic Potentials and Simulation of
                   lattice defects*, P.C. Gehlen, J.R. Beeler Jr. and R.I. Jaffree,
                   (eds), Plenum Press, New York, pp. 3-25 (1972).

[Washburn 80]   Washburn J., Defects Semicond. **2**, 209 (1980).

[Wu 77]   Wu W. K. and J. Washburn, J. Appl. Phys. **48**, 3744
                   (1997).

[Yoshida 61]   Yoshida M., J. Phys. Soc., Japan **16**, 44 (1961).

[Zhang 95]   Zhang L. H., K. S. Jones, P. H. Chi, and D. S. Simons,
                   Appl. Phys. Lett. **67**, 2025 (1995).

[Zhu 96]   Zhu Jing, T. Diaz de la Rubia, L. H. Yang, C. Mailhiot, and
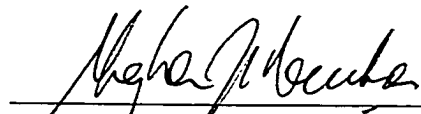   G. H. Gilmer, Phys. Rev. B **54**, 4741 (1996).

BIOGRAPHICAL SKETCH

Gopalakrishnan Subramanian received his Bachelor of Technology degree in metallurgical engineering from the Indian Institute of Technology, Madras, India, in May, 1988. He then proceeded to the University of Texas at Austin where he received a Master of Science degree in materials science and engineering. His M.S thesis was on the development of an $Al_xGa_{1-x}As/$ GaAs photovoltaic cell with epitaxial isolation layer for multijunction applications. He joined the University of Florida in August 1996 and earned his Doctor of Philosophy degree in December 2000.
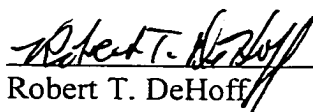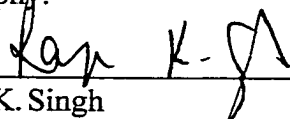
I certify that I have read this study and that in my opinion it conforms to acceptable standards of scholarly presentation and is fully adequate, in scope and quality, as a dissertation for the degree of Doctor of Philosophy.

Kevin S. Jones, Chair
Professor of Materials Science and
Engineering

I certify that I have read this study and that in my opinion it conforms to acceptable standards of scholarly presentation and is fully adequate, in scope and quality, as a dissertation for the degree of Doctor of Philosophy.

Stephen J. Pearton
Professor of Materials Science and
Engineering

I certify that I have read this study and that in my opinion it conforms to acceptable standards of scholarly presentation and is fully adequate, in scope and quality, as a dissertation for the degree of Doctor of Philosophy.

Robert T. DeHoff
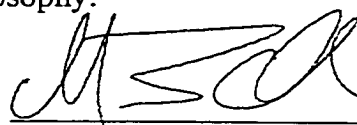Professor of Materials Science and
Engineering

I certify that I have read this study and that in my opinion it conforms to acceptable standards of scholarly presentation and is fully adequate, in scope and quality, as a dissertation for the degree of Doctor of Philosophy.

Rajiv K. Singh
Professor of Materials Science and
Engineering

I certify that I have read this study and that in my opinion it conforms to acceptable standards of scholarly presentation and is fully adequate, in scope and quality, as a dissertation for the degree of Doctor of Philosophy.

Mark E. Law
Professor of Electrical and Computer
Engineering

This dissertation was submitted to the Graduate Faculty of the College of Engineering and to the Graduate School and was accepted as partial fulfillment of the requirements for the degree of Doctor of Philosophy.

December, 2000

M. J. Ohanian
Dean, College of Engineering

Winfred M. Phillips
Dean, Graduate School